Title

CO2 Conversion to value-added Chemicals: Thermodynamic and Indium-based catalysts studies

Author

Alamer, Abdulaziz M

Publication Date

2022

Peer reviewed|Thesis/dissertation

UNIVERSITY OF CALIFORNIA

Los Angeles

CO_2 Conversion to value-added Chemicals: Thermodynamic and Indium-based catalysts studies

A dissertation submitted in partial satisfaction of the

requirements for the degree Doctor of Philosophy

in Chemical Engineering

by

Abdulaziz M. Alamer

2022

ABSTRACT OF THE DISSERTATION

CO_2 Conversion to value-added Chemicals:

Thermodynamic and Indium-based catalysts studies

by

Abdulaziz M. Alamer

Doctor of Philosophy in Chemical Engineering

University of California, Los Angeles, 2022

Professor Vasilios I. Manousiouthakis, Chair

The high dependency on fossil fuels to meet the world's increasing demand for energy has led to an increase in carbon dioxide (CO_2) emissions into the atmosphere, which could lead to irreversible environmental ramifications. Conversion of CO_2 to value added chemicals and/or fuels is a promising strategy not only to mitigate anthropogenic CO_2 emissions, but also to provide a renewable source of energy. Nonetheless, CO_2 is a thermodynamically stable molecule that requires vast energy and an active catalyst to activate it. To address the issue of CO_2 stability, thermodynamic analysis and material science are utilized in this work. In the first part of this thesis, Gibbs free energy minimization is employed to offer an insight into the thermodynamic behavior for the production of dimethyl ether and acetic acid from CO_2 in atomic space. A set of temperatures, pressures, and hydrogen and oxygen atom-mole fractions are identified that allow for maximum production of dimethyl ether and acetic acid and minimum production of by-products, particularly CO_2. In the second part of this thesis, for the first time,

galvanic replacement is employed to synthesize In-based alloy catalysts where the surface structures are highly tailored and the host sites are highly controlled. The synthesized alloys show high stability, activity, and selectivity toward methanol formation, in the conversion of CO_2 to methanol, and CO formation, in the reverse water gas shift reaction. This work offers a new approach for utilizing Gibbs free energy minimization in atomic space for CO_2 based reactions. Additionally, it demonstrates the capability of galvanic replacement in synthesizing In-based alloys with well-defined surface structures.

The dissertation of Abdulaziz M. Alamer is approved.

Yunfeng Lu

E. Charles H. Sykes

Junyoung O. Park

Vasilios I. Manousiouthakis, Committee Chair

University of California, Los Angeles
2022

03/2022

Abdulaziz M. Alamer

Table of Contents

LIST OF FIGURES

LIST OF TABLES

Acknowledgements

During my PhD journey, I received a lot of support and encouragement from multiple people that helped bring this thesis to completion. I would like to first thank my PhD advisor, professor Vasilios Manousiouthakis, for all of the support, guidance, and the opportunity to conduct the experimental components of this thesis at professor Maria Flytzani- Stephanopoulos' lab at Tufts University. Likewise, I would like to extend my deep appreciation to late Prof. Stephanopoulos for her support, guidance, and treating me as one of her PhD student, not just a visiting scholar. Also, I would like to thank Prof. Charles Sykes for his support and supervision especially after the passing of prof. Stephanopoulos. I extend my thanks to my PhD committee: Prof. Yunfeng Lu, Prof. Charles Sykes, and Prof. Junyoung Park, for their constructive comments and suggestions that helped me improve the quality of this thesis.

Professor Nathaniel Eagan who is a friend and, later, a project advisor, played an important role in completing my experimental work for which I am truly grateful. I also would like to thank my friend and collaborator, Faisal Alshafei, for his support during my time in Los Angeles and his helpful projects discussions. Similarly, I would like to thank my labmates at UCLA and Tufts with whom I shared wonderful times. I was lucky to work and collaborate with exceptional people during my PhD. I would like to thank Ibubeleye Somiari (UCLA), Dr. Mengyao Ouyang (Tufts), Dr. Georgios Giannakakis (Tufts), Dr. Muhammad Nadeem (SABIC), Yahya Alsalik (SABIC), Prof. Jeffrey Miller (Purdue), Alexandre Foucher (UPenn), Prof. Eric Stach (UPenn), Dr. Anna Plonka (Stony Brook), Prof. Anatoly Frenkel (Stony Brook), and Dr. Sanjaya Senanayake (BNL).

I would like to thank SABIC for believing in me, not once but twice, first when they

sponsored my undergraduate studies and now my PhD studies as well as for funding my projects at UCLA and Tufts.

Finally, my heartfelt appreciation goes to my parents and family for their support and to my wife for her patience and encouragement.

Vita

2010-2014	Department of Chemical Engineering Worcester Polytechnic Institute Bachelor of Science in Chemical Engineering
2014-2016	Research Engineer Saudi Basic Industries Corporation Saudi Arabia
2016-2018	Department of Chemical and Biomolecular Engineering University of California, Los Angeles Master of Science in Chemical Engineering

Selected Publications and Presentations

- **Abdulaziz M. Alamer,** Ibubeleye Somiari, Maria Flytzani-Stephanopoulos, Vasilios Manousiouthakis. *Chemical-phase equilibrium of CO-CO_2-H_2-CH_3OH-DME-H_2O mixtures in C-H-O atom-mol fraction space using Gibbs free energy minimization*. Submitted
- Ibubeleye Somiari, Demetrios Chaconas, **Abdulaziz M. Alamer,** Maria Flytzani-Stephanopoulos, Vasilios Manousiouthakis. *Coproduction of dimethyl-ether and hydrogen/power from natural gas with no carbon dioxide*. Submitted
- **Abdulaziz M. Alamer**, Mengyao Ouyang, Faisal H. Alshafei, Muhammad Amtiaz Nadeem, Yahya Alsalik, Jeffrey T. Miller, Maria Flytzani-Stephanopoulos, E. Charles H. Sykes, Vasilios Manousiouthakis, Nathaniel M. Eagan. *Design of dilute palladium-indium alloy catalysts for the selective hydrogenation of CO_2 to methanol*. Submitted
- **Abdulaziz M. Alamer**, Vasilios Manousiouthakis. Equilibrium analysis of acetic acid production from carbon dioxide in C-H-O atom-mol fraction space. In preparation.
- Ibubeleye Somiari, Demetrios Chaconas, **Abdulaziz M. Alamer,** Theodore T. Tsotsis , Vasilios Manousiouthakis. *Coproduction of dimethyl ether (DME) and hydrogen/power*

from natural gas with zero carbon dioxide emissions: an attainable region approach. 2020 American Institute of Chemical Engineers (AIChE) Annual Meeting. Virtual.

- **Abdulaziz Alamer**, Mengyao Ouyang, Faisal Alshafei, Jeffrey T. Miller, Maria Flytzani-Stephanopoulos, E Charles Sykes, Vasilios Manousiouthakis, Nathaniel Eagan. *Dilute Alloys of Palladium in Indium Supported onγ-Al2O3 for the Selective Hydrogenation of CO2 to Methanol*. 2021 American Institute of Chemical Engineers (AIChE) Annual Meeting. Boston, MA.

CHAPTER 1: Introduction

1.1 Background

Improved standards of living coupled with an exponential growth in the world's economy in the last few years have dramatically increased demand for fuels, chemicals, and materials [1]. The heightened demand for fossil fuels led to increased greenhouse gases emissions [2]. These anthropogenic emissions into the atmosphere have had several environmental implications, including climate change [3]. One of the most widely emitted greenhouse gasses is carbon dioxide (CO_2). Today, CO_2 accounts for over 70% of greenhouse gases emissions [4,5]. In fact, CO_2 concentration in the atmosphere has increased from 280 part per million (ppm) in the 18th century to 419 ppm in 2021, that is an increase of almost ca. 50% (**Figure 1.1a**) [6]. In 2018, the world CO_2 emission was around 37 Gtones and projections postulate that these levels will reach 45 Gtones by 2040 [7]. Alarmingly, CO_2 emissions have led to notable increases in the earth's temperature by 0.18 °C a year on average, which is more than twice the rate prior to 1981 **(Figure 1.1b)**.

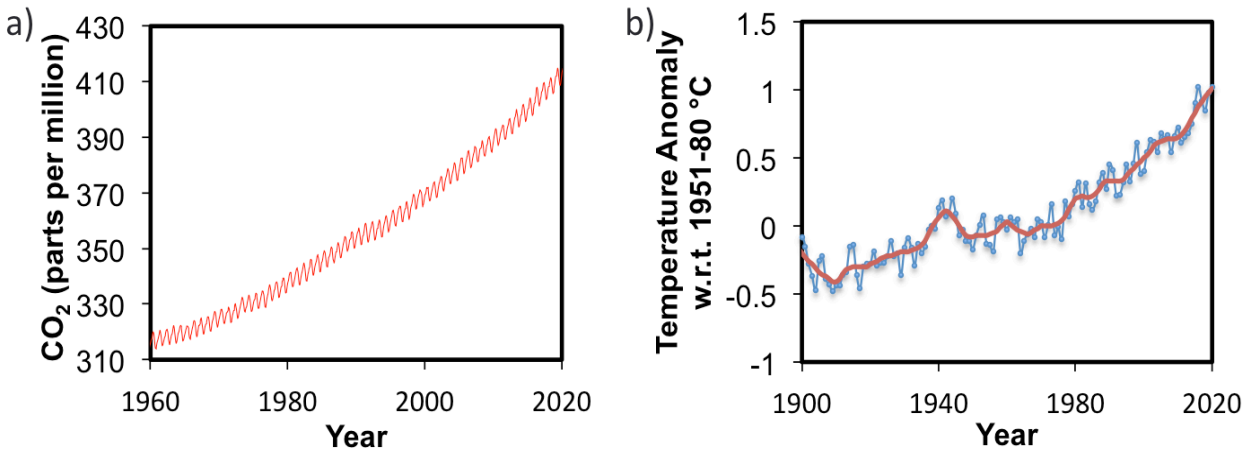

Figure 1.1: (a) Monthly mean atmospheric carbon dioxide in parts per million (ppm) at Mauna Loa Observatory, Hawaii. **(b)** Global average temperature anomaly (1900-2020) [8]

In order to mitigate the severe effects of CO_2 on our planet, in 2015, 195 countries signed an agreement in the United Nations Framework Convention of Climate Change (UNFCCC)

conference in Paris to limit global warming below 2°C above the pre-industrial level [9]. In 2019, the European Commission took a step further to reduce CO_2 emission by pledging to achieve carbon neutral economy by 2050 [10].

To reduce CO_2 emission and achieve carbon neutral economy, different approaches have been considered by scientists and regulators. These approaches include improvement of current industrial processes efficiency to reduce energy consumption; utilization of alternative and renewable energy sources such as, nuclear energy, solar energy, wind power, and biomass; and application of CO_2 capture and storage and/or utilization.

CO_2 Capture and Storage (CCS) technology involved capturing and separating CO_2 from other gases produced at the emission source such as in industrial and energy sites. In CCS, CO_2 is captured by one of the three methods: pre-combustion capture, post-combustion capture or oxyfuel combustion [11]. The captured CO_2 is transported for safe storage by pipelines, road tankers or ships. Finally, CO_2 is stored in depleted oil and gas fields or deep saline aquifer formations several kilometers below the earth's surface. It is projected that using CCS technology can store about 3 Gtones a year of CO_2 by 2031 [12]. While this technology is effective for storing CO_2, one of its key drawbacks is high cost, which makes CCS technology unsustainable [13].

In contrast to CCS, Carbon Capture and Utilization (CCU) technologies by thermocatalytic [14], electrocatalytic [15,16] and photocatalytic processes [17] are more affordable; hence, sustainable. The CCU method utilizes CO_2 emissions as a C_1 building block in synthesizing value added chemicals and fuels such as methanol [18], acetic acid [19], and formic acid [20]. However, for CCU technologies to be more effective than CCS, they ought to be carbon-neutral or have negative carbon emissions.

Although CCU technologies have many advantages and have shown auspicious potential, only a small fraction of CO_2 emitted has been utilized. This is due to the inherent thermodynamic stability of the CO_2 molecule as its carbon exists at its most oxidized state (+4), which requires high temperatures to convert it to value added chemicals [21]. In fact, CO_2 cannot be converted without the presence of a catalyst and/or thermal energy. Therefore, there is a need to develop an active catalyst for converting CO_2 to value-added chemicals by utilizing material science and engineering as well as thermodynamic analysis, to optimize catalyst reactivity and reaction conditions.

1.2 Thermodynamics

Thermodynamics analysis has been an essential and useful tool for understanding, simulating, and optimizing several chemical reaction processes including hydrogenation [22], dehydrogenation [23], and oxidation [24]. This analysis accurately predicts the number of phases at equilibrium and their composition at specific temperatures and pressures. Additionally, thermodynamic analyses provide insight into stability of different chemical species, yields, and selectivities of different products. According to Smith et al., there are two different methods to calculate chemical reaction equilibrium, the stoichiometric and non-stoichiometric methods [25].

In the stoichiometric method, a full understanding of the reaction system is crucial as each reaction should be well defined including its stoichiometric coefficient and equilibrium constant, which are typically obtained experimentally. One of the drawbacks of the stoichiometric method is its sensitivity to the initial values and values obtained experimentally, which affect the accuracy of the phase equilibrium. Conversely, the non-stoichiometric method, i.e., the Gibbs free energy minimization method, only requires knowledge of temperature, pressure, the chemical species involved in the equilibrium, the amounts of each element present

in the feed, and their Gibbs free energy of formation. Non-stoichiometric method does not require any knowledge of reactions in which the species participate.

Given the simplicity of the Gibbs free energy minimization method, it has been utilized to study the thermodynamics of multiple CO_2-based reactions. Several studies have been conducted to confirm the accuracy of Gibbs free energy minimization method. Gao et al., preformed thermodynamic calculation for the methanation reaction of carbon oxides (CO and/or CO_2) using the Gibbs free energy minimization method [26]. They also investigated the effect of different parameters such as temperature, pressure, and composition of reactants on the conversion of CO_x and CH_4 yield. The results matched closely the experimental data [26]. Jia et al. performed a similar study in which they performed thermodynamic analysis by employing Gibbs free energy minimization method on different CO_2 hydrogenation reactions towards CO, hydrocarbons, alcohols, aldehydes and carboxylic acids [27]. The obtained experimental data validated the calculated data for CO_2 methanantion and reverse water gas shift reaction.

These studies confirmed the accuracy of the Gibbs free energy minimization method, and its effectiveness as a tool for understanding the thermodynamics of complicated reaction system without knowledge of the reaction chemistry and input from experimental data. In our quest to further simplify the Gibbs free energy minimization method, our group proposed a general conceptual framework where numbers of elements are considered rather than species to reduce the extent of parametric studies that need to be carried out to capture a mixture's equilibrium behavior. Chaconas et al. employed Gibbs free energy minimization method in atomic space to investigate the thermodynamic equilibrium of a mixture consisting of CH_4, CO, CO_2, H_2, H_2O, and C for different industrial processes including steam methane reforming, dry methane dry

reforming, and syngas methanation [28]. This framework will be utilized in this thesis to study the thermodynamics of CO_2 hydrogenation to different value- added products.

1.3 Indium Oxide

Indium oxide, In_2O_3, is a yellow colored material that is derived from metal indium which was discovered in 1863 coincidentally by Reich and Richter in Germany [29]. Indium oxide and its related indium-based materials have been used in various applications including, solar cell, touch screens, optoelectronic devices, gas sensors, liquid crystal displays, and energy efficient windows, and that is due to the fact that indium oxide is a highly transparent material and exhibits high electrical conductivity [30–34]. Hexagonal indium oxide, In_2O_3, is the most common oxide phase and In^{3+} is the most common oxidation state of indium [35]. In_2O_3 have three different crystal structures: body-centered cubic bixbyite-type crystal (c-In_2O_3) (**Figure 1.2**), metastable rhombohedral corundum-type crystal (rh-In_2O_3) and orthorhombic Rh_2O_3(II)-type crystal structures [36]. However, the interesting catalytic properties of In_2O_3 have not attracted much attention until recently, especially its selective conversion of CO_2.

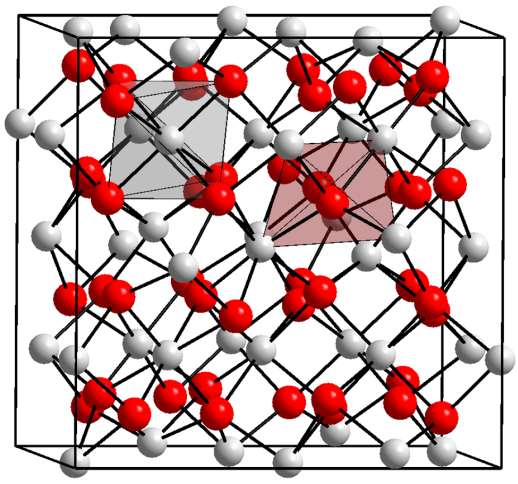

Figure 1.2: Cubic Bixbyite Structure of Indium Oxide [37]

In 2008, a study conducted by Umegaki et al. showed that In_2O_3 catalysts have a high hydrogen (H_2) selectivity and without any CO detected in ethanol steam reforming which suggested that In_2O_3 might be a selective catalyst toward CO_2 formation [38]. Subsequent work by Lorenz et al. showed In_2O_3 is indeed an active and a selective catalyst toward CO_2 in methanol steam reforming reaction and only a small amount of CO is formed (< 5%) [39]. To further understand the mechanism of CO_2 formation on In_2O_3, Bielz et al. investigated In_2O_3 catalyst for CO_2 production via water gas shift reaction (WGS) and formaldehyde reforming [40]. Their results reveal that CO can easily reduce the surface of In_2O_3 and CO_2 is produced by reacting CO with the reactive oxygen lattice forming oxygen vacancies in the process which cannot be replenished by CO_2. Also, CO_2 production from formaldehyde indicates that formaldehyde is a possible intermediate. These results suggested that In_2O_3 could be a potential novel catalyst for CO_2 hydrogenation to methanol.

To understand the elementary step of methanol formation on In_2O_3 from CO_2, Prof. Qingfeng Ge and his group preformed density functional theory (DFT) studies to investigate the adsorption and hydrogenation of CO_2 on In_2O_3 (110) surface [41]. Their DFT results revealed that CO_2 is activated upon adsorption forming carbonate species by reacting with surface oxygen. H_2 dissociates heterolytically to form hydroxyl (H-O) and hydride (H-In) on the surface, where the hydride reacts with carbonate to form surface formate species, which is believed to be the preferred pathway for methanol production from CO_2, although it is highly endothermic (+0.33 eV). Whereas, when hydroxyl reacts with carbonate, it forms surface bicarbonate, which is exothermic (-0.78 eV); however, the consequent step to form CO is highly endothermic (+1.07 eV), which results in reproduction of CO_2 and water. Further study by the same group showed that oxygen vacancy is critical in methanol synthesis from CO_2 over In_2O_3 (110) surface and that

the reaction follows a mechanism involving the cyclic creation and annihilation of oxygen vacancies [42]. Their DFT also suggests that H_2 help generate oxygen vacancies where CO_2 is adsorbed as HCOO species. This adsorption process is both thermodynamically and kinetically favorable resulting in further hydrogenation to form adsorbed HCOO, H_2CO, H_3CO species. The hydrogenation of H_2CO to H_3CO is the rate-limiting step during which oxygen vacancy is filled and methanol is produced.

Experimental work conducted by Sun et al. confirmed that In_2O_3 is, indeed, an active catalyst for methanol synthesis from CO_2 [43]. They showed that CO_2 conversion and methanol yield increases with increasing the temperature up to 300°C, and above 330°C, the competing reverse water gas shift (RWGS) starts to dominate. This indicates that the RWGS reaction can be inhibited at lower temperatures, which is fundamentally different than what occurs in Cu/ZnO, commercial catalyst for methanol synthesis from syngas, catalysts where methanol is synthesized through RWGS route rather than the formate route. Subsequently, Martin et al. synthesized bulk In_2O_3 and supported In_2O_3 which displayed 100% methanol selectivity from CO_2, either by co-feeding carbon monoxide (CO) or supporting In_2O_3 on ZrO_2, and stability for 1000 hours at industrially relevant conditions [44]. Their in-depth characterization revealed that methanol production proceeds through the same mechanism, the cyclic creation and annihilation of oxygen vacancies, as proposed earlier by Ye et al.

The promising results of indium-based catalysts were exploited in bifunctional catalysts system, too, where methanol is utilized as a reactive intermediate rather than a terminal product Indium oxide can be used as a bifunctional catalyst along with acid catalysts, e.g., aluminosilicates (zeolites) and silicoaluminophosphates (SAPOs), to convert CO_2 to hydrocarbons such as light olefins (C_2-C_4) [45] and gasoline range hydrocarbons (C_{5+}) [46].

To further enhance the activity of indium-based catalysts, a dopant, especially noble metals, have been utilized to improve the dissociative adsorption of H_2 and to provide interfacial sites for CO_2 adsorption and hydrogenation. Ye et al. demonstrated through DFT calculation that introducing Pd to In_2O_3 enhances the catalyst's activity as Pd provides metal site for H_2 dissociative adsorption and interfacial sites for CO_2 adsorption and hydrogenation, and formate route is the dominate pathway. A subsequent experimental study showed that using a peptide template to prepare Pd/In_2O_3 resulted in the formation of well-dispersed Pd particles, which improved the activity of the catalyst due to the improved dissociative adsorption of H_2 and adsorption of CO_2. Snider et al. observed a similar positive affect of Pd for $Pd\text{-}In/SiO_2$ catalyst where the active site arises from the synergy between the indium oxide phase and intermetallic InPd with an In-rich surface [47]. In another Pd-related work, Frei et al. utilized a co-precipitation method to synthesize low nuclearity Pd clusters by replacing indium atoms by palladium atoms in the active In_3O_3 ensemble which improved the methanol yield, reaching 0.96% $g_{MeOH}\ h^{-1}\ g_{cat}^{-1}$, which is the highest methanol yield from CO_2 over a heterogonous catalyst [48].

Inspired by the earlier work for Pd promoted In_2O_3, Wang et al. prepared highly dispersed rhodium (Rh) support In_2O_3 by a deposition-precipitation method which resulted in an improved methanol yield due to the promotional effect of Rh for dissociative adsorption and spillover of H_2 as well as CO_2 adsorption and activation [49]. Another work by Han et al., where they prepared atomically dispersed Pt^{n+} atoms support in In_2O_3, revealed that atomically dispersed Pt atoms acts as a Lewis acid site to promote the heterolytic dissociation of H_2 that enhances methanol yield whereas Pt nanoparticle boosts RWGS to form CO [50]. Another dopant, gold (Au), was investigated by Rui et al., which showed enhanced performance and selectivity for CO_2 hydrogenation to methanol. The enhanced performance was attributed to the reactive $Au^{\delta+}$–

In_2O_{3-x} interface that was due to the strong metal-support interaction [51]. This strong bonding increases the gold dispersion and prevents its sintering under reaction condition.

These finding reveals that metal dopants improve the activity and selectivity of indium-based catalysts toward methanol production as dopants provides site for hydrogen dissociation which then transfers to the In_2O_3 surface via spillover to react with adsorbed carbon-containing species to produce methanol.

1.4 Aim and structure of the thesis

The objective of this thesis is to limit the environmental impact of the increased carbon dioxide (CO_2) concentration in the atmosphere by converting CO_2 to value-added chemicals, namely, dimethyl ether (DME), acetic acid, methanol, and carbon monoxide (CO). The thesis is divided into two sections: theoretical and experimental. Theoretical: thermodynamic analysis of CO_2 to DME and acetic acid, **chapter 2** and **chapter 3**. Experimental: fundamental understating of indium-based catalysts for CO_2 hydrogenation, **chapter 4** and **chapter 5**.

Chapter 2 presents chemical and phase equilibrium analysis for a CO-CO_2-H_2-CH_3OH-DME-H_2O mixture by utilizing Gibbs free energy minimization. The mixture's feed composition is presented in C-H-O space and different operating conditions are investigated to identify conditions favoring DME production and minimizing by products formation.

Chapter 3 examines the thermodynamic equilibrium behavior of a mixture that consists of seven species: CO, CO_2, H_2, CH_3OH, H_2O, CH_3COOH, and $C_3H_6O_2$. A similar approach to the one utilized in Chapter 2 was employed in this study to identify the operating point that maximizes acetic acid production while minimizes other by products.

Chapter 4 demonstrates the ability of utilizing galvanic replacement to synthesize In-based catalyst, in particular Pd-In alloys, where the surface structure of these alloys can be

highly tuned. Various Pd-In alloy containing Pd in various states of aggregation (isolated atom, small clusters, extended clusters) are synthesized and tested for CO_2 hydrogenation to methanol.

Chapter 5 investigates the capability of galvanic replacement to modify the surface of Cu/In_2O_3 nanoparticle by selectively deposit Pd atoms on the surface of different host metal forming different Pd alloys. The synthesized alloys are tested in CO_2 hydrogenation to methanol and reverse water gas shift reaction.

CHAPTER 2: Chemical-Phase Equilibrium of CO-CO_2-H_2-CH_3OH-DME-H_2O Mixture in C-H-O Atom Fraction Space Using Gibbs Free Energy Minimization

2.1 Introduction

The concentration of carbon dioxide (CO_2) in the atmosphere has been increasing since the industrial revolution. As of 2019, it has surpassed 400 parts per million (ppm) and this pattern is expected to continue, and to reach 1000 ppm by 2100 [52]. The Intergovernmental Panel on Climate Change (IPCC) suggests that increased atmospheric carbon dioxide concentrations contribute to an increase in the earth's temperature [53]. Due to the increased CO_2 atmospheric concentrations, extensive research is being conducted to reduce CO_2 emissions to the atmosphere. One research direction focuses on utilizing CO_2 as a carbon source to produce carbon containing high value chemicals such as formic acid [54], methane [55,56], methanol [57] and dimethyl ether [58] (DME). Dimethyl Ether (DME) has attracted much attention as an alternative to liquefied petroleum gas (LPG) and a fuel in the diesel engines, given its high cetane number, low soot emissions and physical properties [59,60].

Commercially, DME is synthesized in a two-step process. In the first step, synthesis gas is converted to methanol, typically over $Cu/ZnO/Al_2O_3$ catalyst at 35-100 bar and 200-300 ^oC [61–64]. In the second step, methanol is dehydrated to DME over solid acid catalyst such as γ-Al_2O_3 at a pressure of 10-20 bar and temperature of 220-350^oC [63]. Recently, there has been renewed interest in a single step process for DME synthesis from synthesis gas. This typically takes place over a bifunctional catalyst and the methanol synthesis and methanol dehydration reactions occur in the same reactor [63,64]. This single step process is preferred given its low thermodynamic limitations. However, because the reaction is highly exothermic, effective temperature control is

critical to prevent runaway reactions [64]. Even though the single step process is thermodynamically favorable, it is not fully commercialized due to the lack of highly selective catalysts that can operate at high pressures, high temperatures and are robust to the presence of water. This has prompted further research in bifunctional catalyst development [65–67], and in related thermodynamic studies supportive of future reaction kinetics, and process design/optimization efforts.

Several thermodynamic studies involving the Gibbs free energy minimization approach have been carried out for the DME production process. These studies, coupled with sensitivity analysis, provide preliminary results on process objectives such as conversion, yield, and selectivity, and assess the impact of process parameters on process objectives. The Gibbs free energy minimization approach is favored because it requires no foreknowledge of the reaction scheme involved, but only knowledge of the species present and the reaction conditions. Chen et al. utilized Gibbs free energy minimization method to study the thermodynamics of both the single step and two step methods of DME synthesis from syngas and CO_2 [68]. The group reported that single step synthesis has lower thermodynamic limitations and high CO_2 conversion and DME selectivity. Shen et al studied the thermodynamic equilibrium of CO_2 hydrogenation to methanol and DME and the effect of temperature, pressure and feed composition on CO_2 equilibrium conversion, methanol yield and DME yield [69]. Their study showed that CO_2 hydrogenation to DME has a higher equilibrium product yield. Stangeland et al. showed that product condensation can enhance CO_2 conversion, without adversely affecting product selectivity [70]. These DME synthesis equilibrium studies often incorporate the impact of different feed compositions on the obtained equilibrium products. Although this is feasible for mixtures involving a small number of species, thermodynamic analysis may be problematic for

mixtures with a high number of species, as a thorough sensitivity analysis to feed composition is more difficult to carry out. To overcome this difficulty for mixtures with a significant number of species (such as the six species mixture involved in this study), there is a need for a thermodynamic equilibrium analysis approach that employs a more compact representation of the considered mixture's feed composition.

The use of compact representations to address reactor analysis and design problems has a long tradition in chemical engineering. Gavalas [71] and Horn [72] "introduced the invariant manifold [71] and the attainable region (AR) [72] concepts, as the sets of all points in concentration space that are attainable through reaction [71] and through reaction and mixing [72] from a given feed point.". This latter AR concept has been applied to reactors [73,74], reactive separators [75] reactor design [76], general process networks [77], reactor networks within the Infinite DimEnsionAl State-space (IDEAS) framework [78–81], and the direct synthesis of DME from syngas [82]. In the above spirit of developing compact representations to address reactor analysis and design problems, in this work, we address the need to carry out reaction and phase equilibrium analysis using a compact representation of the considered mixture's feed composition, by minimizing the total Gibbs free energy of the system subject to atomic conservation, which is expressed in terms of the feed's atom-mol fractions, which are then required to belong to an attainable region (AR). This AR concept refers to all possible atom-mol fractions that can be attained from predetermined list of species, and is distinct from the aforementioned AR efforts [72–82], which refer to the set of all reactor network outlet species concentrations attainable from a given feed, and will thus be referred to as the Atom Species Attainable Region (ASAR), as it only requires knowledge of all species that can possibly comprise the considered system (the reactor inlet). Previously, we introduced and quantified this

ASAR concept so as to effectively carry out Gibbs free energy minimization-based reaction/phase equilibrium analysis for a CH_4-CO-CO_2-H_2O-H_2-C mixture [28]. In this work, the ASAR concept is formally defined next, and subsequently employed to efficiently carry out equilibrium analysis for a CO-CO_2-H_2-CH_3OH-DME-H_2O mixture.

2.2 Definition of Atom Species Attainable Region (ASAR) in Atom-Mol Fraction Space for Mixtures of Known Species

In the International System of Units (SI), a mol refers to 6.02214076×10^{23} elementary entities, such as atoms, molecule, ions, or electrons [83]. Consider a system containing a list of species $\{i=1,NC\}$ with an associated list of elements, each of which is present in at least one of the species $\{j=1,NE\}$. For the considered system, let $a_i\left(\frac{i^{th}\ element's\ atom-mol}{total\ atom-mol}\right)$, $F_j\left(\frac{j^{th}\ species'\ mol}{total\ atom-mol}\right)$, and $\nu_{i,j}\left(\frac{i^{th}\ element's\ atom-mol}{j^{th}\ species'\ mol}\right)$ denote the *i*th element's atom-mol fraction, the *j*th species' mol per total atom-mol of the system, and the number of atoms (or atom-mol) of element *i* in a molecule (or mol) of species *j*, respectively. It clearly holds:

$$\left\{a_i=\sum_{j=1}^{NC}\nu_{i,j}F_j\ \ \forall i=1,NE;\ \sum_{i=1}^{NE}a_i=1;\ a_i\geq 0\ \ \forall i=1,NE;\ F_j\geq 0\ \ \forall j=1,NC\right\}.$$

Considering that $\{F_j\}_{j=1}^{NC}\in\mathbb{R}^{NC}$ may be required to satisfy further restrictions quantified by the feasible region $\Omega\subset\mathbb{R}^{NC}$, then the Atom Species Attainable Region (ASAR) is defined as:

$$ASAR \triangleq \left\{ \left\{ a_i \right\}_{i=1}^{NE} \in \mathbb{R}^{NE} : \left\{ \begin{array}{l} \sum_{i=1}^{NE} a_i = 1,\ a_i \geq 0 \quad \forall i = 1, NE \\ \exists \left\{ F_j \right\}_{j=1}^{NC} \in \Omega \subset \mathbb{R}^{NC} : \left\{ \begin{array}{l} a_i = \sum_{j=1}^{NC} \nu_{i,j} F_j \quad \forall i = 1, NE \\ F_j \geq 0 \quad \forall j = 1, NC \end{array} \right\} \end{array} \right\} \right\}$$

Therefore, the ASAR narrative definition is:

Definition

The ASAR for a system that is known to contain a predetermined list of species is the set of all possible system atom-mol fractions that can be attained by considering all possible system compositions, in mol per total atom-mol, over the predetermined list of species.

Though, the ASAR is typically defined as a subset of $\mathbb{R}^{NE}$, it can also be defined as a subset of $\mathbb{R}^{NE-1}$, by substituting one of the element atom-mol fractions.

Thus, the Atom Species Attainable Region (ASAR) can also be defined as:

$$ASAR \triangleq \left\{ \left\{ a_i \right\}_{i=1}^{NE-1} \in \mathbb{R}^{NE-1} : \left\{ \begin{array}{l} \sum_{i=1}^{NE} a_i - 1 \leq 0,\ a_i \geq 0 \quad \forall i = 1, NE \\ \exists \left\{ F_j \right\}_{j=1}^{NC} \in \Omega \subset \mathbb{R}^{NC} : \left\{ \begin{array}{l} a_i = \sum_{j=1}^{NC} \nu_{i,j} F_j \quad \forall i = 1, NE-1 \\ 1 = \sum_{i=1}^{NE} \sum_{j=1}^{NC} \nu_{i,j} F_j \\ F_j \geq 0 \quad \forall j = 1, NC \end{array} \right\} \end{array} \right\} \right\}$$

The above ASAR definitions enable the development of compact representations for efficient reactor analysis/design based on reaction/phase equilibrium. Once the ASAR is quantified in atom mol-fraction space, Gibbs free energy minimization is carried out for a broad collection of ASAR points and a wide range of temperatures and pressures. This is possible,

since the Gibbs free energy minimization problem features the same minimum for any of the infinite number of inlet compositions that correspond to the same ASAR point. Thus, the low-dimensional parameter space in which the ASAR belongs can be explored in a numerically efficient manner so as to identify desirable atom-mol fraction combinations and temperature/pressure conditions. Next, propositions are presented rigorously quantifying the set of all atom-mol fraction combinations that can be attained using the CO-CO_2-H_2-CH_3OH-DME-H_2O species list and a reduced list of species that do not include CH_3OH and DME. The results of this comprehensive equilibrium analysis are then presented, and conclusions are drawn.

2.3 Construction of Atom Species Attainable Region (ASAR) in Atom-Mol Fraction Space for CO-CO_2-H_2-CH_3OH-Dme-H_2O Mixtures

Chemical-phase equilibrium studies carried out using the Gibbs free energy minimization conceptual framework, make clear that knowledge of a list of participating species, of the total atom-mol normalized atom-mol amounts of each element entering the system, and of the temperature, and pressure, completely determines the total atom-mol normalized mol amount of each considered species that is present at equilibrium. Knowledge of the mol amount of each species entering the system is not needed, thus significantly reducing the extent of parametric studies that need to be carried out to capture a mixture's equilibrium behavior. Given however that only the considered species are allowed to contribute to the total atom-mol normalized atom-mol amounts of each element entering the system, it is then necessary to identify the region in atom-mol fraction space that can be attained using all possible feed mixture compositions.

In this work, a six-component mixture is considered, consisting of the following species and elements $\{(1)CO; (2)CO_2; (3)H_2; (4)CH_3OH; (5)CH_3OCH_3; (6)H_2O\}$, $\{(1)C; (2)H; (3)O\}$.

Then the following proposition holds:

Proposition 1

Consider the linear variety in the atom-mol fraction space $\left\{\left(a_C, a_H, a_O\right) \in \mathbb{R}^3, a_C + a_H + a_O = 1\right\}$ for the six-component mixture $\left\{(1)CO; (2)CO_2; (3)H_2; (4)CH_3OH; (5)CH_3OCH_3; (6)H_2O\right\}$.

Substituting $a_C = 1 - a_H - a_O$, enables quantification of the mixture's atom species attainable region in the reduced atom-mol fraction space $\left\{\left(a_H, a_O\right) \in \mathbb{R}^2\right\}$ as:

$$\left\{\begin{array}{l} -\frac{3}{2}a_H - 2a_O + 1 \le 0; \\ -a_H - 3a_O + 1 \le 0; \\ -\frac{7}{2}a_H - 6a_O + 3 \le 0; \\ \frac{3}{2}a_H + 3a_O - 2 \le 0; \\ a_H + a_O - 1 \le 0; \\ -a_H \le 0; -a_O \le 0 \end{array}\right\} \qquad (1)$$

Proof.

The point $\left(a_C, a_H, a_O\right) \in \mathbb{R}^3$ belongs to the ASAR in the atom-mol fraction space $\left\{\left(a_C, a_H, a_O\right) \in \mathbb{R}^3\right\}$ if and only if there exists $\left(F_1, F_2, F_3, F_4, F_5, F_6\right)$ such that:

$$\left\{\begin{array}{l} a_C = F_1 + F_2 + F_4 + 2F_5 \\ a_H = 2F_3 + 4F_4 + 6F_5 + 2F_6 \\ a_O = F_1 + 2F_2 + F_4 + F_5 + F_6 \\ F_1 \ge 0,\ F_2 \ge 0,\ F_3 \ge 0,\ F_4 \ge 0,\ F_5 \ge 0,\ F_6 \ge 0 \\ a_C \ge 0, a_H \ge 0, a_O \ge 0, a_C + a_H + a_O = 1 \end{array}\right\} \Leftrightarrow$$

$$\left\{\begin{array}{l} F_5 = \frac{1}{2}a_C - \frac{1}{2}F_1 - \frac{1}{2}F_2 - \frac{1}{2}F_4 \\ F_3 = \frac{1}{2}a_H - 2F_4 - 3F_5 - F_6 \\ F_6 = a_O - F_1 - 2F_2 - F_4 - F_5 \\ F_1 \geq 0,\ F_2 \geq 0,\ F_3 \geq 0, \\ F_4 \geq 0,\ F_5 \geq 0,\ F_6 \geq 0 \\ a_C \geq 0, a_H \geq 0, a_O \geq 0, a_C + a_H + a_O = 1 \end{array}\right\} \Leftrightarrow$$

$$\left\{\begin{array}{l} F_5 = \frac{1}{2}a_C - \frac{1}{2}F_1 - \frac{1}{2}F_2 - \frac{1}{2}F_4 \\ F_3 = -a_C + \frac{1}{2}a_H - a_O + 2F_1 + 3F_2 \\ F_6 = a_O - \frac{1}{2}a_C - \frac{1}{2}F_1 - \frac{3}{2}F_2 - \frac{1}{2}F_4 \\ F_1 \geq 0,\ F_2 \geq 0,\ F_4 \geq 0, \\ -a_C + \frac{1}{2}a_H - a_O + 2F_1 + 3F_2 \geq 0 \\ \frac{1}{2}a_C - \frac{1}{2}F_1 - \frac{1}{2}F_2 - \frac{1}{2}F_4 \geq 0 \\ a_O - \frac{1}{2}a_C - \frac{1}{2}F_1 - \frac{3}{2}F_2 - \frac{1}{2}F_4 \geq 0 \\ a_C \geq 0, a_H \geq 0, a_O \geq 0, a_C + a_H + a_O = 1 \end{array}\right\} \Leftrightarrow$$

$$\left\{\begin{array}{l} F_5 = \frac{1}{2}a_C - \frac{1}{2}F_1 - \frac{1}{2}F_2 - \frac{1}{2}F_4 \\ F_3 = -a_C + \frac{1}{2}a_H - a_O + 2F_1 + 3F_2 \\ F_6 = a_O - \frac{1}{2}a_C - \frac{1}{2}F_1 - \frac{3}{2}F_2 - \frac{1}{2}F_4 \\ 0 \le F_4 \le min\left[\begin{array}{l}\left(a_C - F_1 - F_2\right), \\ \left(2a_O - a_C - F_1 - 3F_2\right)\end{array}\right] \\ F_1 \ge 0,\ F_2 \ge 0,\ F_4 \ge 0, \\ -a_C + \frac{1}{2}a_H - a_O + 2F_1 + 3F_2 \ge 0 \\ 0 \le a_C - F_1 - F_2 \\ 0 \le 2a_O - a_C - F_1 - 3F_2 \\ a_C \ge 0, a_H \ge 0, a_O \ge 0, a_C + a_H + a_O = 1 \end{array}\right\} \Leftrightarrow$$

$$\left\{\begin{array}{l} F_5 = \frac{1}{2}a_C - \frac{1}{2}F_1 - \frac{1}{2}F_2 - \frac{1}{2}F_4 \\ F_3 = -a_C + \frac{1}{2}a_H - a_O + 2F_1 + 3F_2 \\ F_6 = a_O - \frac{1}{2}a_C - \frac{1}{2}F_1 - \frac{3}{2}F_2 - \frac{1}{2}F_4 \\ 0 \le F_4 \le min\left[\begin{array}{l}\left(a_C - F_1 - F_2\right), \\ \left(2a_O - a_C - F_1 - 3F_2\right)\end{array}\right] \\ max\left[0, \left(\frac{1}{3}a_C - \frac{1}{6}a_H + \frac{1}{3}a_O - \frac{2}{3}F_1\right)\right] \le F_2 \le \\ \le min\left[\left(a_C - F_1\right), \left(\frac{2}{3}a_O - \frac{1}{3}a_C - \frac{1}{3}F_1\right)\right] \\ 0 \le F_1 \\ 0 \le a_C - F_1 \\ 0 \le \frac{2}{3}a_O - \frac{1}{3}a_C - \frac{1}{3}F_1 \\ \frac{1}{3}a_C - \frac{1}{6}a_H + \frac{1}{3}a_O - \frac{2}{3}F_1 \le a_C - F_1 \\ \frac{1}{3}a_C - \frac{1}{6}a_H + \frac{1}{3}a_O - \frac{2}{3}F_1 \le \frac{2}{3}a_O - \frac{1}{3}a_C - \frac{1}{3}F_1 \\ a_C \ge 0, a_H \ge 0, a_O \ge 0, a_C + a_H + a_O = 1 \end{array}\right\} \Leftrightarrow$$

$$
\left\{\begin{array}{l}
F_5 = \frac{1}{2}a_C - \frac{1}{2}F_1 - \frac{1}{2}F_2 - \frac{1}{2}F_4 \\
F_3 = -a_C + \frac{1}{2}a_H - a_O + 2F_1 + 3F_2 \\
F_6 = a_O - \frac{1}{2}a_C - \frac{1}{2}F_1 - \frac{3}{2}F_2 - \frac{1}{2}F_4 \\
0 \le F_4 \le min\left[\begin{array}{l}(a_C - F_1 - F_2), \\ (2a_O - a_C - F_1 - 3F_2)\end{array}\right] \\
max\left[(0), \left(\frac{1}{3}a_C - \frac{1}{6}a_H + \frac{1}{3}a_O - \frac{2}{3}F_1\right)\right] \le F_2 \le min\left[(a_C - F_1), \left(\frac{2}{3}a_O - \frac{1}{3}a_C - \frac{1}{3}F_1\right)\right]
\end{array}\right\} \Leftrightarrow
$$

$$
\left\{\begin{array}{l}
max\left[\begin{array}{l}0, \\ \left(2a_C - \frac{1}{2}a_H - a_O\right)\end{array}\right] \le F_1 \le min\left[\begin{array}{l}a_C, (2a_O - a_C), \\ \left(2a_C + \frac{1}{2}a_H - a_O\right)\end{array}\right] \\
0 \le a_C,\ 2a_C - \frac{1}{2}a_H - a_O \le a_C \\
0 \le 2a_O - a_C,\ 2a_C - \frac{1}{2}a_H - a_O \le 2a_O - a_C \\
0 \le 2a_C + \frac{1}{2}a_H - a_O,\ 2a_C - \frac{1}{2}a_H - a_O \le 2a_C + \frac{1}{2}a_H - a_O \\
a_C \ge 0, a_H \ge 0, a_O \ge 0, a_C + a_H + a_O = 1
\end{array}\right\}
$$

$$
\left\{
\begin{array}{l}
F_5 = \frac{1}{2}a_C - \frac{1}{2}F_1 - \frac{1}{2}F_2 - \frac{1}{2}F_4 \\
F_3 = -a_C + \frac{1}{2}a_H - a_O + 2F_1 + 3F_2 \\
F_6 = a_O - \frac{1}{2}a_C - \frac{1}{2}F_1 - \frac{3}{2}F_2 - \frac{1}{2}F_4 \\
0 \le F_4 \le min\left[\begin{array}{l}(a_C - F_1 - F_2), \\ (2a_O - a_C - F_1 - 3F_2)\end{array}\right] \\
max\left[\begin{array}{l}0, \\ \left(\frac{1}{3}a_C - \frac{1}{6}a_H + \frac{1}{3}a_O - \frac{2}{3}F_1\right)\end{array}\right] \le F_2 \le min\left[\begin{array}{l}(a_C - F_1), \\ \left(\frac{2}{3}a_O - \frac{1}{3}a_C - \frac{1}{3}F_1\right)\end{array}\right] \\
max\left[\begin{array}{l}0, \\ \left(2a_C - \frac{1}{2}a_H - a_O\right)\end{array}\right] \le F_1 \le min\left[\begin{array}{l}a_C, \\ (2a_O - a_C), \\ \left(2a_C + \frac{1}{2}a_H - a_O\right)\end{array}\right] \\
a_C - \frac{1}{2}a_H - a_O \le 0,\ a_C - 2a_O \le 0,\ 3a_C - \frac{1}{2}a_H - 3a_O \le 0 \\
0 \le 2a_C + \frac{1}{2}a_H - a_O,\ a_C \ge 0, a_H \ge 0, a_O \ge 0, a_C + a_H + a_O = 1
\end{array}
\right\}
$$

$$
\left\{
\begin{array}{l}
F_5 = \frac{1}{2}\left(1 - a_H - a_O - F_1 - F_2 - F_4\right) \\
F_3 = -1 + \frac{3}{2}a_H + 2F_1 + 3F_2 \\
F_6 = \frac{1}{2}\left(-1 + a_H + 3a_O - F_1 - 3F_2 - F_4\right) \\
0 \le F_4 \le min\begin{bmatrix} 1 - a_H - a_O - F_1 - F_2, \\ -1 + a_H + 3a_O - F_1 - 3F_2 \end{bmatrix} \\
max\begin{bmatrix} 0, \\ \frac{1}{3} - \frac{1}{2}a_H - \frac{2}{3}F_1 \end{bmatrix} \le F_2 \le min\begin{bmatrix} 1 - a_H - a_O - F_1, \\ -\frac{1}{3} + \frac{1}{3}a_H + a_O - \frac{1}{3}F_1 \end{bmatrix} \\
max\begin{bmatrix} 0, \\ 2 - \frac{5}{2}a_H - 3a_O \end{bmatrix} \le F_1 \le min\begin{bmatrix} 1 - a_H - a_O, \\ -1 + a_H + 3a_O, \\ 2 - \frac{3}{2}a_H - 3a_O \end{bmatrix} \\
1 - \frac{3}{2}a_H - 2a_O \le 0;\ 1 - a_H - 3a_O \le 0;\ 3 - \frac{7}{2}a_H - 6a_O \le 0; \\
-2 + \frac{3}{2}a_H + 3a_O \le 0;\ -1 + a_H + a_O \le 0;\ -a_H \le 0;\ -a_O \le 0;\ a_C = 1 - a_H - a_O
\end{array}
\right\} \text{O.E.}\Delta.
$$

The ASAR, given by the above set of inequalities, is represented graphically in Figure 3 below. The ASAR (hatched region) is a polygon in (a_H, a_O)space with vertices (0, 0.5), (0, 0.667), (0.667, 0.333), (1, 0) and (0.667, 0.111). The ASAR shown in **Figure 2.1** will subsequently be explored to identify regions in (a_H, a_O) space that meet specific process objectives related to DME synthesis.

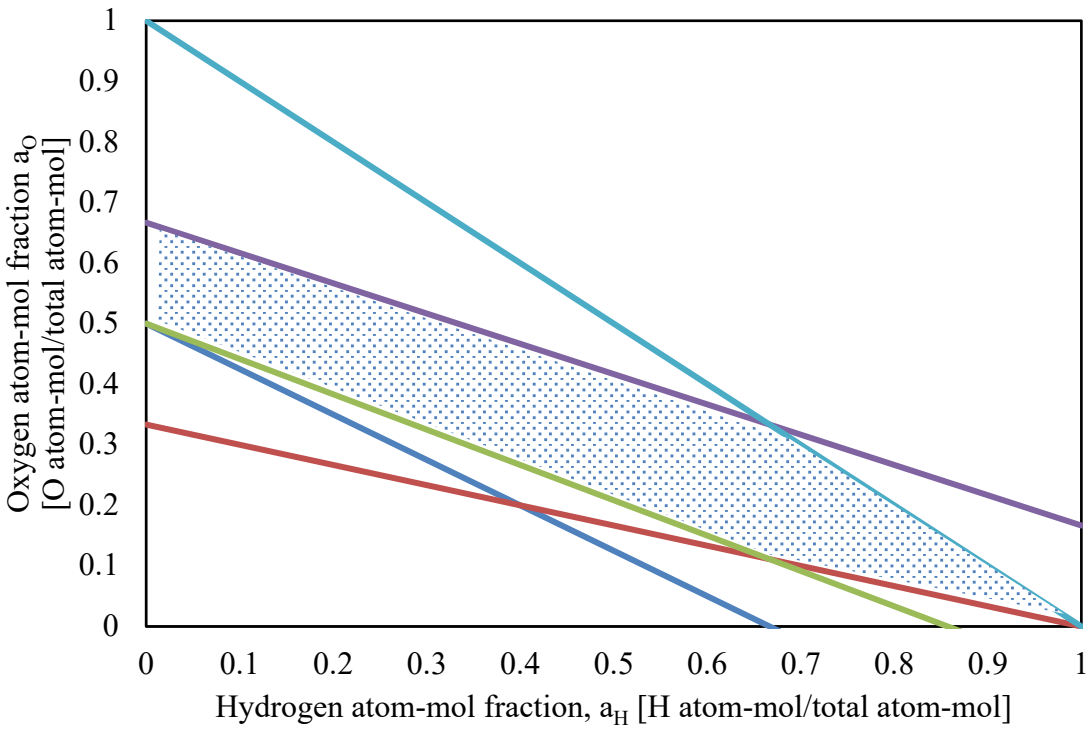

Figure 2.1: ASAR in atom-mol fraction space of {CO, CO_2, H_2, CH_3OH, CH_3OCH_3, H_2O} mixture

An important consideration in this work is DME production. Thus, it is of interest to quantify the ASAR for feeds not involving the presence of DME. Further, from an atom content viewpoint, methanol can be viewed as a combination of CO and H_2. Thus, it is desirable to quantify the ASAR for a {CO, CO_2, H_2, H_2O} mixture. To this end the following proposition holds.

Proposition 2

The ASAR sub-region in the reduced atom-mol fraction space, $\left(a_H, a_O\right) \in \mathbb{R}^2$, with $a_c = 1 - a_H - a_O$, for the four-component mixture $\left\{(1)CO; (2)CO_2; (3)H_2; (6)H_2O\right\}$ is:

$$\left\{\begin{array}{l} -a_H - 2a_O + 1 \le 0 \\ \frac{3}{2}a_H + 3a_O - 2 \le 0 \\ a_H + a_O - 1 \le 0 \\ -a_H \le 0, -a_O \le 0 \end{array}\right\} \qquad (2)$$

Proof.

The point $\left(a_H, a_O\right) \in \mathbb{R}^2$ belongs to the sub-region's ASAR in the atom-mol fraction space $a_c = 1 - a_H - a_O$ if and only if there exists $\left(F_1, F_2, F_3, F_6\right)$ such that:

$$\left\{\begin{array}{l} a_C = F_1 + F_2 \\ a_H = 2F_3 + 2F_6 \\ a_O = F_1 + 2F_2 + F_6 \\ F_1 \geq 0,\ F_2 \geq 0,\ F_3 \geq 0,\ F_4 = 0,\ F_5 = 0,\ F_6 \geq 0 \\ a_C \geq 0, a_H \geq 0, a_O \geq 0, a_C + a_H + a_O = 1 \end{array}\right\} \Leftrightarrow$$

$$\left\{\begin{array}{l} F_1 = a_C - F_2 \\ F_6 = \dfrac{1}{2} a_H - F_3 \\ F_2 = \dfrac{1}{2} a_O - \dfrac{1}{2} F_1 - \dfrac{1}{2} F_6 \\ F_1 \geq 0,\ F_2 \geq 0,\ F_3 \geq 0,\ F_4 = 0,\ F_5 = 0,\ F_6 \geq 0 \\ a_C \geq 0, a_H \geq 0, a_O \geq 0, a_C + a_H + a_O = 1 \end{array}\right\} \Leftrightarrow$$

$$\left\{\begin{array}{l} F_1 = -\dfrac{3}{2} a_H - 3a_O + 2 - F_3 \\ F_6 = \dfrac{1}{2} a_H - F_3 \\ F_2 = \dfrac{1}{2} a_H + 2a_O - 1 + F_3 \\ F_3 \geq 0,\ F_4 = 0,\ F_5 = 0 \\ -\dfrac{3}{2} a_H - 3a_O + 2 - F_3 \geq 0 \\ \dfrac{1}{2} a_H - F_3 \geq 0 \\ \dfrac{1}{2} a_H + 2a_O - 1 + F_3 \geq 0 \\ a_C \geq 0, a_H \geq 0, a_O \geq 0, a_C = 1 - a_H - a_O \end{array}\right\} \Leftrightarrow$$

$$\left\{\begin{array}{l} F_1 = -\frac{3}{2}a_H - 3a_O + 2 - F_3 \\ F_6 = \frac{1}{2}a_H - F_3 \\ F_2 = \frac{1}{2}a_H + 2a_O - 1 + F_3 \\ \max\begin{bmatrix} -\frac{1}{2}a_H - 2a_O + 1 \\ 0 \end{bmatrix} \le F_3 \le \min\begin{bmatrix} -\frac{3}{2}a_H - 3a_O + 2 \\ \frac{1}{2}a_H \end{bmatrix} \\ F_4 = 0,\ F_5 = 0 \\ -\frac{1}{2}a_H - 2a_O + 1 \le -\frac{3}{2}a_H - 3a_O + 2 \\ -\frac{1}{2}a_H - 2a_O + 1 \le \frac{1}{2}a_H \\ 0 \le -\frac{3}{2}a_H - 3a_O + 2 \\ 0 \le \frac{1}{2}a_H \\ a_C \ge 0, a_H \ge 0, a_O \ge 0, a_C = 1 - a_H - a_O \end{array}\right\} \Leftrightarrow$$

$$\left\{\begin{array}{l} F_1 = -\frac{3}{2}a_H - 3a_O + 2 - F_3 \\ F_6 = \frac{1}{2}a_H - F_3 \\ F_2 = \frac{1}{2}a_H + 2a_O - 1 + F_3 \\ \max\begin{bmatrix} -\frac{1}{2}a_H - 2a_O + 1 \\ 0 \end{bmatrix} \le F_3 \le \min\begin{bmatrix} -\frac{3}{2}a_H - 3a_O + 2 \\ \frac{1}{2}a_H \end{bmatrix} \\ F_4 = 0,\ F_5 = 0 \\ \\ 0 \le 1 - a_H - a_O \\ 0 \le a_H + 2a_O - 1 \\ 0 \le -\frac{3}{2}a_H - 3a_O + 2 \\ a_C \ge 0, a_H \ge 0, a_O \ge 0, a_C = 1 - a_H - a_O \end{array}\right\} O.E.\Delta$$

The ASAR sub-region given by the above set of inequalities, is represented graphically in **Figure 2.2** below, with the following vertices in (a_H, a_O)space: (0, 0.5), (0, 0.667), (0.667, 0.333), and (1, 0). The bottom-shaded region (hatch pattern) constitutes the region in atom-mol space that cannot be accessed in the absence of DME in the reactor inlet. This ASAR sub-region shown in **Figure 2.2** will subsequently be explored to identify regions in (a_H, a_O) space that meet specific process objectives related to DME synthesis.

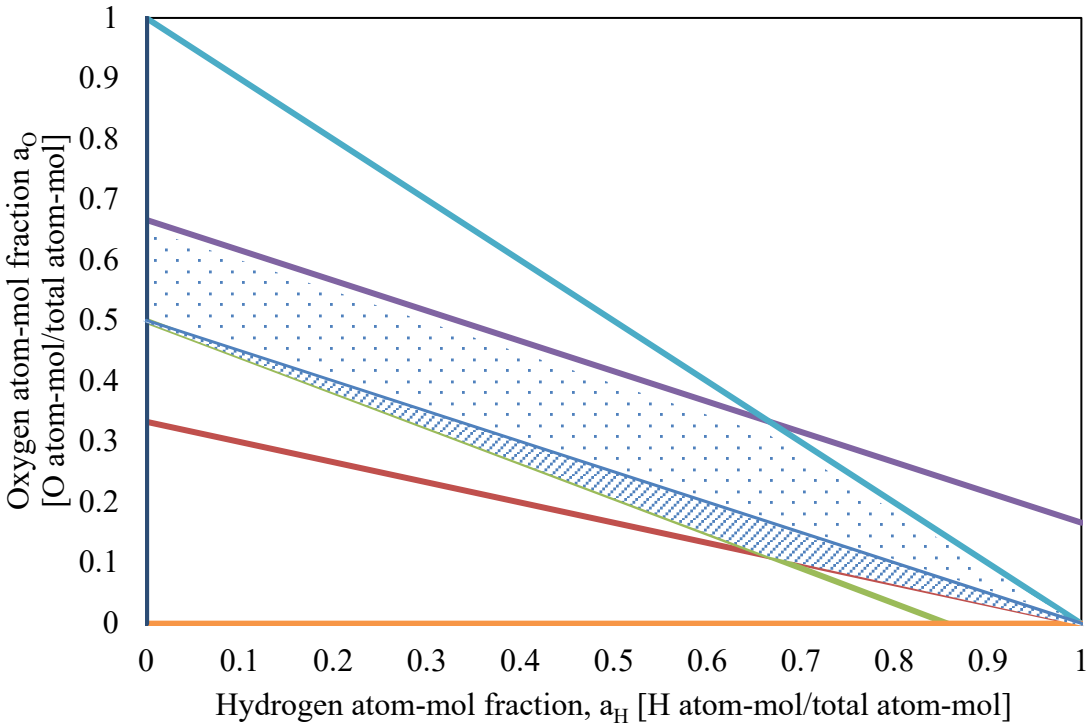

Figure 2.2: ASAR in atom-mol fraction space of {CO, CO_2, H_2, H_2O} mixture

2.4 Thermodynamic Studies of DME Synthesis using Total Gibbs Free Energy Minimization in Atom-Mol Fraction Space

In this work, the total Gibbs free energy minimization method is employed to identify the equilibrium liquid and vapor compositions of the species, CO, CO_2, H_2, CH_3OH, CH_3OCH_3, H_2O, as functions of inlet atom-mol fractions at various temperatures and pressures. Justification of the system's chemical and phase equilibrium stems from the fact that experimental results of

DME synthesis from syngas (CO, CO_2, H_2) approached those predicted at equilibrium for CO conversion and product selectivity [84]. It has also been shown that thermodynamic calculations based on Gibbs minimization method produced results that closely matched experimental data for systems containing syngas such as the reverse water gas shift reaction [27]. For the predicted phases of suitable points in the ASAR, thermodynamic stability is checked by simulating those points using UniSim Design R470 software. UniSim Design R470 carries out phase stability calculations based on Michelson's implementation of the Gibbs' tangent-plane distance criterion for phase stability [85,86]. For simplicity, coke formation is not considered in this thermodynamic analysis. However, from an experimental point of view, coke formation is attenuated by a high hydrogen partial pressure [87], moderate acidity of catalyst [88], and the presence of water in the reaction medium [89–91]. As such, it follows that ASAR points formed from high hydrogen and water feed contents will reduce coke formation.

The general total Gibbs free energy minimization problem [92] at a constant temperature and pressure is presented below.

$$\left\{\begin{array}{l} \bar{\pi}\left(T,P,\left\{\bar{a}_i\right\}_{i=1}^{NE}\right) \triangleq \min\limits_{\left\{n_j^{(k)}\right\}_{(j,k)=(1,1)}^{(NC,NP)}} \bar{G}\left(T,P,\left\{n_j^{(k)}\right\}_{(j,k)=(1,1)}^{(NC,NP)}\right) \\ s.t. \\ \bar{a}_i - \sum\limits_{k}^{NP}\sum\limits_{j}^{NC} \nu_{i,j} n_j^{(k)} = 0, \quad \forall i = 1, NE \\ n_j^{(k)} \geq 0, \quad \forall j = 1, NC \quad \forall k = 1, NP \end{array}\right\} \Leftrightarrow$$

$$\left\{\begin{array}{l}\overline{\pi}\left(T,P,\left\{\overline{a}_i\right\}_{i=1}^{NE}\right)\triangleq\min\limits_{\left\{n_j^{(k)}\right\}_{(j,k)=(1,1)}^{(NC,NP)}}\sum\limits_{k=1}^{NP}\sum\limits_{j=1}^{NC}n_j^{(k)}\mu_j^{(k)}\left(T,P,\left\{\dfrac{n_j^{(k)}}{\sum\limits_{p=1}^{NC}n_p^{(k)}}\right\}_{j=1}^{NC}\right)\\ s.t.\\ \overline{a}_i-\sum\limits_{k}^{NP}\sum\limits_{j}^{NC}\nu_{i,j}n_j^{(k)}=0,\quad\forall i=1,NE\\ n_j^{(k)}\geq 0,\forall j=1,NC\qquad\forall k=1,NP\end{array}\right\}\Leftrightarrow$$

$$\left\{\begin{array}{l}\overline{\pi}\left(T,P,\left\{\overline{a}_i\right\}_{i=1}^{NE}\right)\triangleq\min\limits_{\left\{n_j^{(k)}\right\}_{(j,k)=(1,1)}^{(NC,NP)}}\sum\limits_{k=1}^{NP}\sum\limits_{j=1}^{NC}n_j^{(k)}\left(G_j^o\left(T\right)+RT\ln\dfrac{\hat{f}_j^{(k)}}{f_j^o}\right)\\ s.t.\\ \overline{a}_i-\sum\limits_{k}^{NP}\sum\limits_{j}^{NC}\nu_{i,j}n_j^{(k)}=0,\quad\forall i=1,NE\\ n_j^{(k)}\geq 0,\forall j=1,NC\qquad\forall k=1,NP\end{array}\right\}$$

Because $\overline{G}\left(T,P,\left\{n_j^{(k)}\right\}_{(j,k)=(1,1)}^{(NC,NP)}\right)$ is a first order homogenous function for fixed T,P [92], the following relation holds: $\overline{G}\left(T,P,\left\{n_j^{(k)}\right\}_{(j,k)=(1,1)}^{(NC,NP)}\right)=\overline{a}_T\sum\limits_{k=1}^{NP}\sum\limits_{j=1}^{NC}F_j^{(k)}\left(G_j^o\left(T\right)+RT\ln\dfrac{\hat{f}_j^{(k)}}{f_j^o}\right)$, where $\overline{a}_T\triangleq\sum\limits_{i=1}^{NE}\overline{a}_i$, $a_i\triangleq\dfrac{\overline{a}_i}{\overline{a}_T}$, $F_j^{(k)}\triangleq\dfrac{n_j^{(k)}}{\overline{a}_T}$. Then the above optimization problem's optimum satisfies: $\overline{\pi}\left(T,P,\left\{\overline{a}_i\right\}_{i=1}^{NE}\right)\triangleq\overline{a}_T\cdot\pi\left(T,P,\left\{a_i\right\}_{i=1}^{NE}\right)$, where the latter is defined as:

$$\left\{\begin{array}{l} \pi\left(T,P,\left\{a_i\right\}_{i=1}^{NE}\right) \triangleq \min\limits_{\left\{F_j^{(k)}\right\}_{(j,k)=(1,1)}^{(NC,NP)}} \sum\limits_{k=1}^{NP}\sum\limits_{j=1}^{NC} F_j^{(k)}\left(G_j^o(T)+RT\ln\dfrac{\hat{f}_j^{(k)}}{f_j^o}\right) \\ s.t. \\ a_i-\sum\limits_{k}^{NP}\sum\limits_{j}^{NC}\nu_{i,j}F_j^{(k)}=0, \qquad \forall i=1,NE \\ F_j^{(k)}\geq 0, \qquad \forall j=1,NC; \quad \forall k=1,NP \\ \sum\limits_{i=1}^{NE} a_i = 1 \end{array}\right\} \tag{3}$$

Solution of the above Gibbs minimization problem requires a thermodynamic model to determine the fugacity of each species in each phase. The fugacities of species *j* in the vapor and liquid phases are evaluated using the gamma/phi (γ/ϕ) thermodynamic model. The fugacity, $\hat{f}_j^V$, of species *j* in the vapor mixture is computed using its fugacity coefficient, $\hat{\phi}_j$, while the fugacity $\hat{f}_j^L$ of species *j* in the liquid mixture is computed using its activity coefficient γ_j. The necessary optimality conditions of (3) require the equality of these fugacities, giving rise to the conditions below:

$$\left\{\begin{array}{ll} \hat{f}_j^V = y_j\ \hat{\phi}_j\left(T,P,\left\{y_j\right\}_{j=1}^{NC}\right)P & \forall j=1,\cdots,NC \\ \hat{f}_j^L = x_j\,\gamma_j\left(T,\left\{x_j\right\}_{j=1}^{NC}\right)P_j^{sat}(T) & \forall j=1,\cdots,NC \\ \hat{f}_j^V = \hat{f}_j^L & \forall j=1,\cdots,NC \end{array}\right\} \tag{4}$$

In this work the modified Soave−Redlich−Kwong (SRK) method is used to model the vapor phase, as it has been experimentally validated by van Bennekom et al. [93] at a pressure of 200 bar, which is higher than the maximum pressure of 80 bar investigated in this work, and employs interaction coefficients (**Table 2.1**) to correct for non-ideal effects of the mixture. The UNIFAC activity model is used for the liquid phase, and the Gibbs minimization studies were

carried out using the RGibbs reactor module and the database of physical properties in the Aspen plus software.

Table 2.1: Binary Interaction Parameters (k_{ij}) for SRK ESO [93]

	i					
j		CO	CO_2	CH_3OH	H_2	H_2O
	CO	-	0.1164	-0.37	-0.0007	-0.474
	CO_2	0.1164	-	0.1	0.1164	0.3
	CH_3OH	-0.37	0.1	-	-0.125	-0.075
	H_2	-0.0007	0.1164	-0.125	-	-0.745
	H_2O	-0.474	0.3	-0.075	-0.745	-

Solution of the above optimization problem is carried out for various reactor inlet atom-mol fractions, and reactor outlet temperatures and pressures. Given that the reactor inlet temperature and pressure are unimportant, a gas phase inlet can be considered without loss of generality. For each feasible considered $\left(a_H, a_O, T, P\right)$ combination, the reactor feed is chosen as:

$$\left\{\begin{array}{l} \max\begin{bmatrix} -\frac{1}{2}a_H - 2a_O + 1 \\ 0 \end{bmatrix} \le F_{H_2}^{(g)} \le \min\begin{bmatrix} -\frac{3}{2}a_H - 3a_O + 2 \\ \frac{1}{2}a_H \end{bmatrix} \\ F_{CO}^{(g)} = -\frac{3}{2}a_H - 3a_O + 2 - F_{H_2}^{(g)} \\ F_{H_2O}^{(g)} = \frac{1}{2}a_H - F_{H_2}^{(g)} \\ F_{CO_2}^{(g)} = \frac{1}{2}a_H + 2a_O - 1 + F_{H_2}^{(g)} \end{array}\right\}$$

Equilibrium analysis is carried out at temperature-pressure combinations of $T\left(^oC\right) \in \{100, 200, 300\}$ and $P\left(bar\right) \in \{10, 40, 80\}$, and the obtained results are presented in the form of outlet vapor and liquid species molar flows per total atom-mol, $F_j^{(k)}$.

2.5 Results and Discussion

Figure 2.3 presents iso- a_O lines of mole over total atom-mol normalized ratios of the *i*th species for a_O values ranging from 0.3 to 0.5, and T (°C) = 100 and P = 10 bar. The majority of the species appear in the vapor phase with the exception of H_2O. In the vapor phase, CO_2 increases while DME and CH_3OH decrease. DME and CO_2 production exhibit the same trends of steadily increasing until a peak value is reached, followed by a decrease in the vapor phase. The atom-mol normalized DME amount in the vapor phase, $F_{DME}^{(V)}$, reaches its maximum values of 0.072, 0.05 and 0.033, at $\left(a_H, a_O\right)$= (0.435, 0.3), (0.3, 0.4) and (0.2, 0.5) respectively, while that of CO_2, $F_{CO_2}^{(V)}$, reaches its maximum values of 0.23, 0.15 and 0.12 at $\left(a_H, a_O\right)$= (0.2, 0.3), (0.3, 0.4) and (0.45, 0.5) respectively. When DME production is at its maximum in the vapor phase, a very small amount of CH_3OH and CO are produced. Over 50% of carbon and most of the hydrogen atoms fed to the system are contained in DME, whereas 40% of carbon atoms go to CO_2 production. In the liquid phase, DME, CH_3OH, CO_2 and H_2O production increase linearly while CO decreases reaching near zero as a_H increases. At the maximum a_H, $a_H = 0.6$, the production of CH_3OH surpasses the DME production.

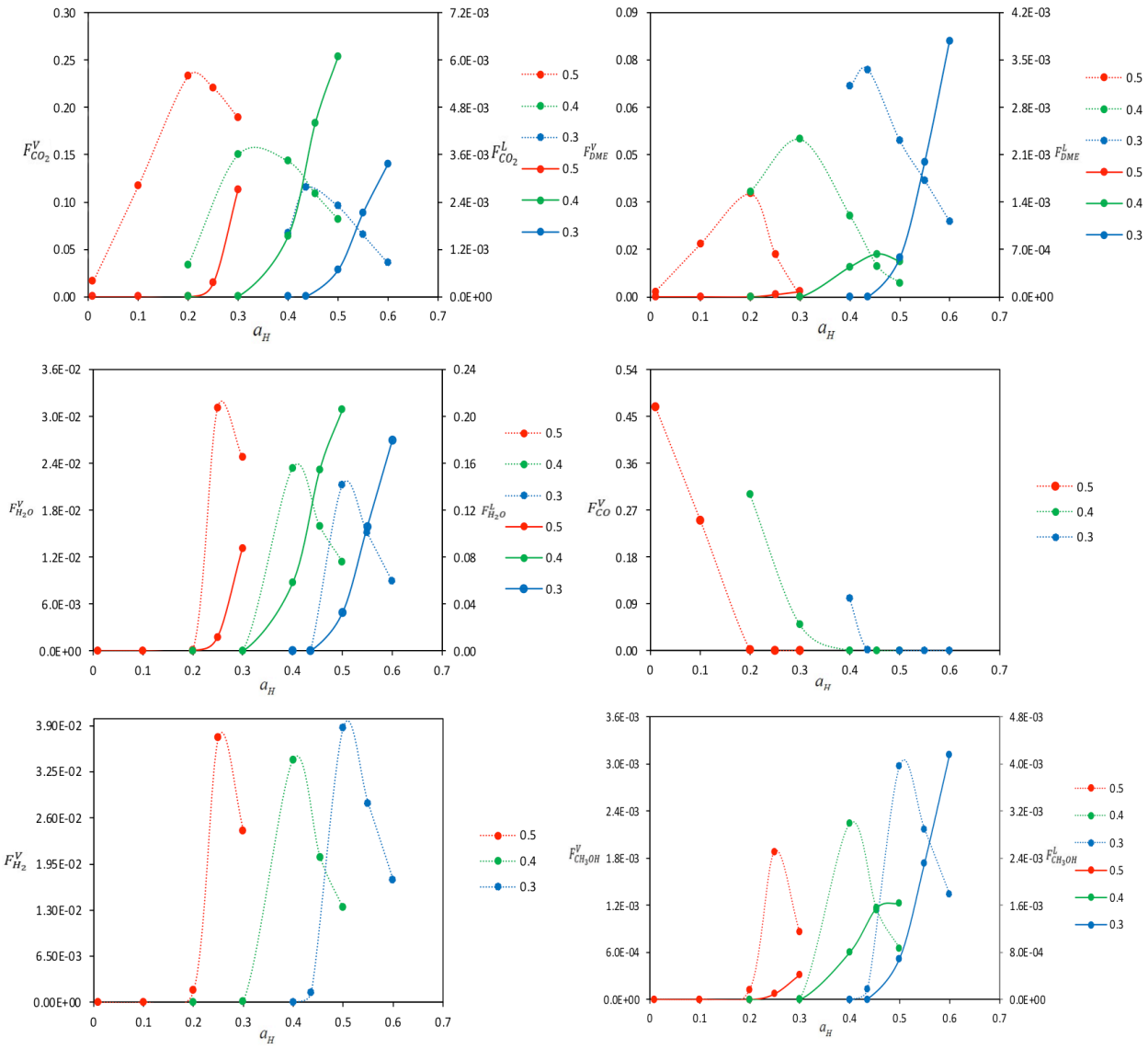

Figure 2.3: $F_j^{(V)}$(dashed, left), $F_j^{(L)}$(solid, right) iso- a_O lines as a_H functions, T=100°C, P=10 bar

More species appear in the liquid phase as P is increased from 10 bar to 40 bar, while maintaining the temperature at 100°C (**Figure 2.4**). The aforementioned CH_3OH, H_2, vapor production trends, and DME, CO_2 vapor and liquid production trends remain intact. At (a_H, a_O) = (0.4, 0.3), DME forms solely in the vapor phase accompanied with CO_2 and CO formation, with $F^{(V)}_{DME} = F^{(V)}_{CO_2} = 0.0667$, $F^{(V)}_{CO}$ =0.1, and $F^{(V)}_{CH_3OH} = 0$. When a_H is increased to 0.435, there is

almost no CO formation and DME and CO_2 formation increases to $F_{DME}^{(V)} = 0.0724$ and $F_{CO_2}^{(V)} = 0.1158$, respectively. CH_3OH forms mostly in the liquid phase and its production is more than doubled compared to 100°C and 10 bar. Thus, the operating points (a_H, a_O, T, P) = (0.435, 0.3, 100°C, 40 bar) is promising for DME production, where the only products are DME and CO_2. As the pressure is increased to 80 bar, a similar pattern occurs where most of the product forms mostly in the liquid phase except for CO and H_2O.

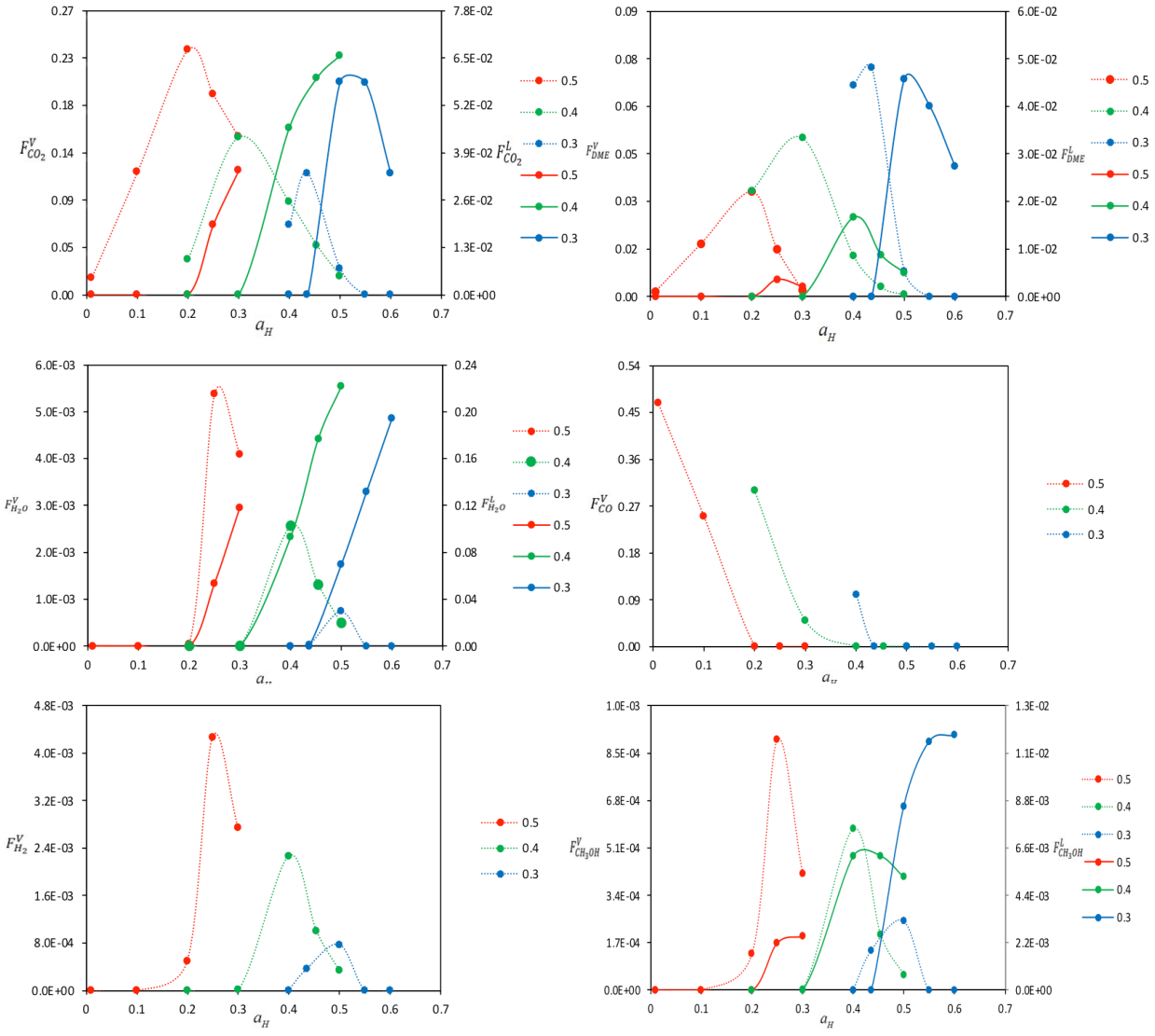

Figure 2.4: $F_j^{(V)}$(dashed, left), $F_j^{(L)}$(solid, right) iso- a_O lines as a_H functions, T=100°C, P=40 bar

As the temperature is increased from 100°C to 200°C at P = 10 bar, all the species appear exclusively in the vapor phase as presented in **Figure 2.5**. The maximum $F_{DME}^{(V)}$ = 0.064 occurs at (a_H, a_O)= (0.4, 0.3), which features a lower a_H value than the one where the maximum $F_{DME}^{(V)}$ occurs at (a_H, a_O)= (0.435, 0.3) for 100°C and 10 bar. When DME production is at its maximum, CO formation is barely observed, and carbon and hydrogen atoms are directed to DME of 43% and 96% respectively. CH_3OH exhibits a similar trend with a maximum of $F_{CH_3OH}^{(V)}$ = 0.0034 at (a_H, a_O) = (0.5, 0.3). As a_H increases at a fixed a_O, CO decreases reaching zero while H_2O increases. At a lower a_O, the effect of increasing a_H has a lower impact on CO_2 formation.

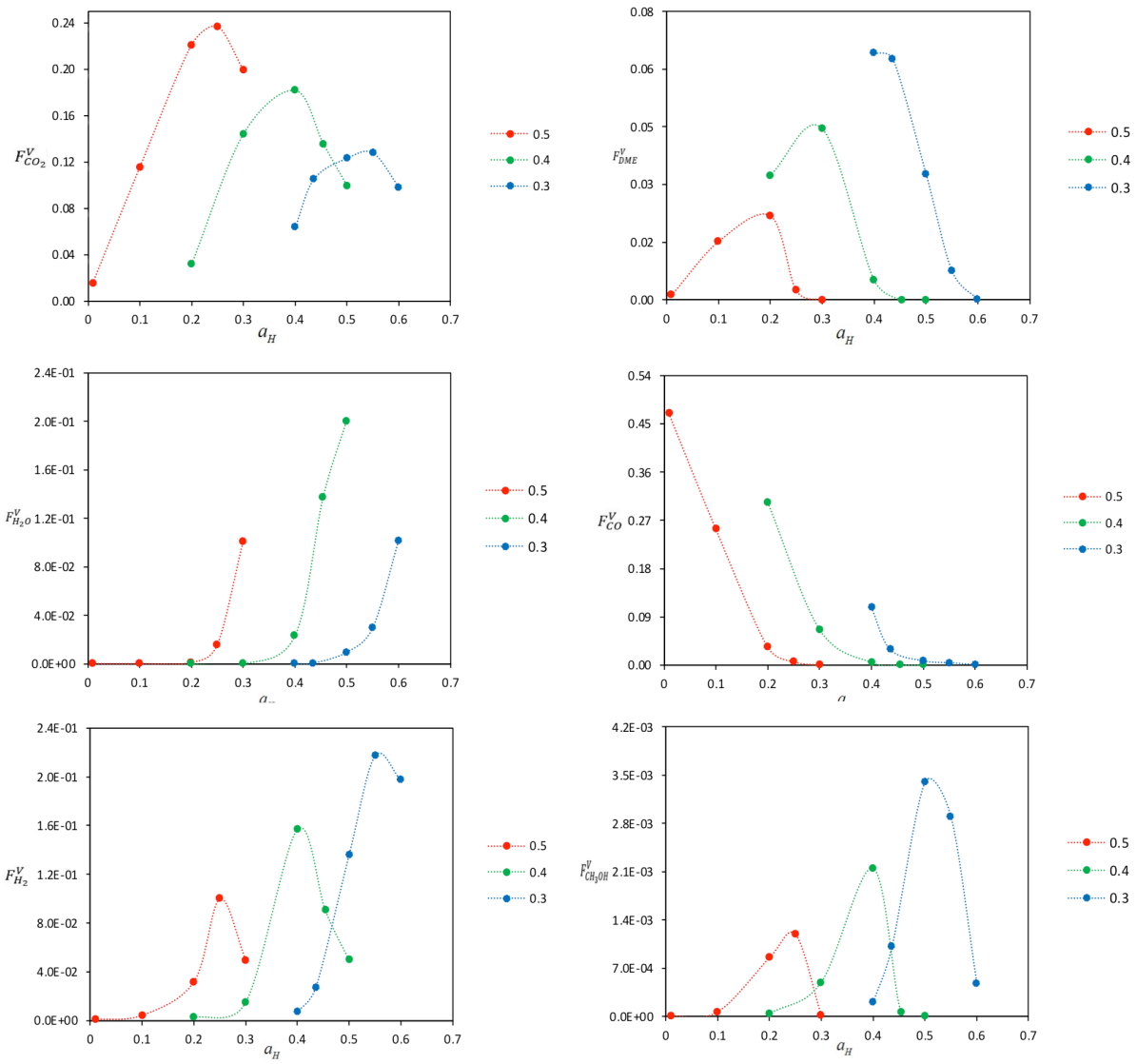

Figure 2.5: $F_j^{(V)}$(dashed, left) iso- a_O lines as a_H functions, T=200°C, P=10 bar

Figure 2.6 shows that as the pressure is increased to 40 bar at a constant temperature of 200°C, small amounts of CH_3OH and H_2O start to appear in the liquid phase at a higher a_H, a_H =0.5. Also, increasing the pressure has little effect on DME production, while it more than doubles the production of CH_3OH. The maximum $F_{DME}^{(V)}$ = 0.069, is observed at (a_H, a_O) = (0.435, 0.3) with a negligible amount of CH_3OH, CO, and H_2O. At this point, carbon and hydrogen atom utilization of 52% and 94%, respectively, is observed with respect to DME

formation, which makes this operating point appealing given that it is in range of commercial processes [51]. As the pressure is increased to 80 bar, more species start to appear in the liquid phase without any significant improvement of DME production, while overall CH_3OH production significantly increases and a considerate amount of CH_3OH forms in the liquid phase.

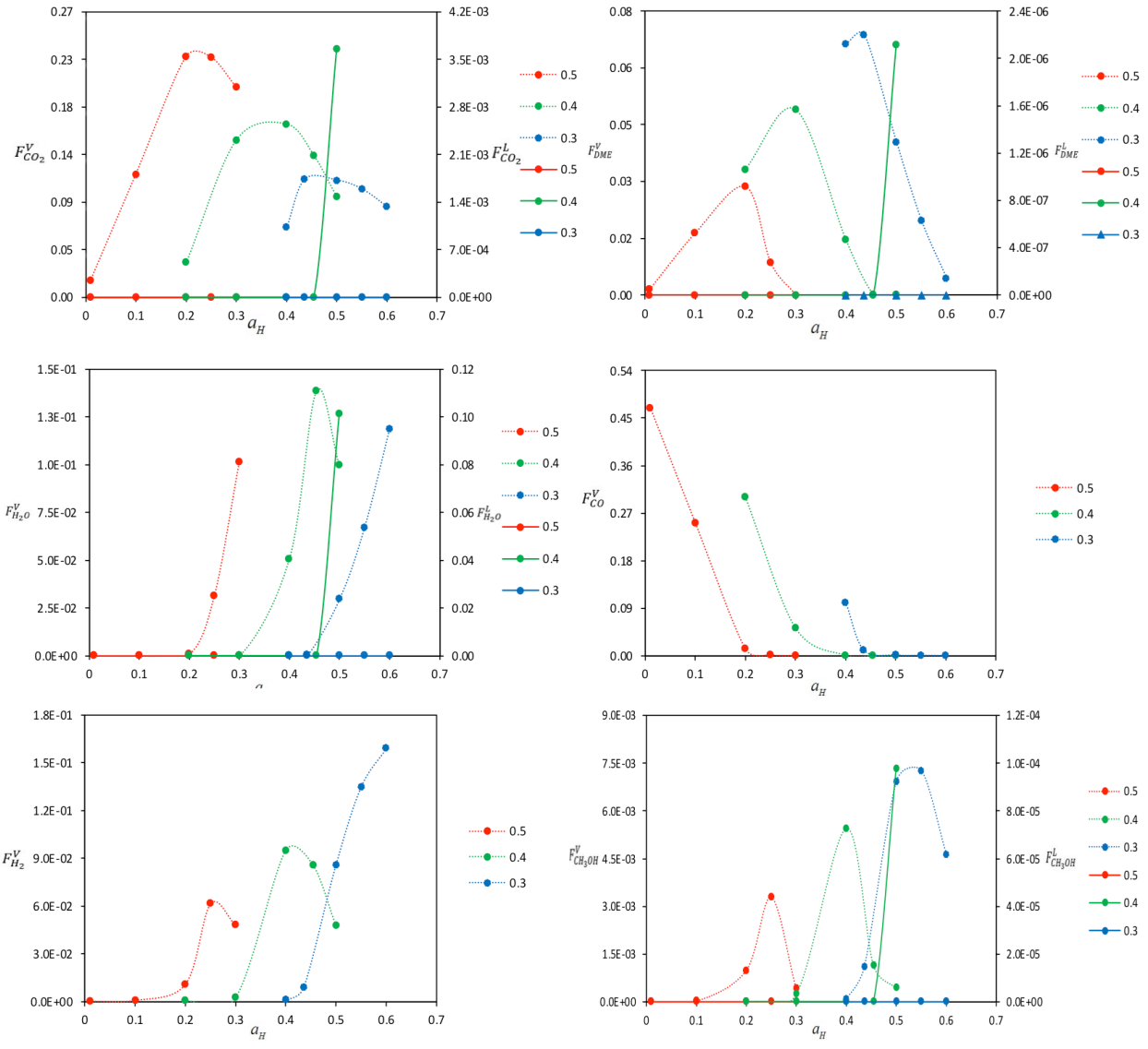

Figure 2.6: $F_j^{(V)}$(dashed, left), $F_j^{(L)}$(solid, right) iso- a_O lines as a_H functions, T=200°C, P=40 bar

Figure 2.7 shows that as the temperature increases from 200°C to 300°C at P = 10 bar, there is a significant decrease in DME formation with the maximum $F_{DME}^{(V)}$ = 0.02 at (a_H, a_O) =

(0.4, 0.3), At this point, only 13% carbon and 30% hydrogen atom utilization is directed to the DME product, with the majority of carbon going into CO formation. As for CH_3OH production, the maximum $F_{CH_3OH}^{(V)}$ = 0.001, occurs at (a_H, a_O) = (0.435, 0.3) compared to its occurrence at (a_H, a_O) = (0.5, 0.3) at 200°C and 10 bar. As a_H decreases, more CO forms for all a_O values.

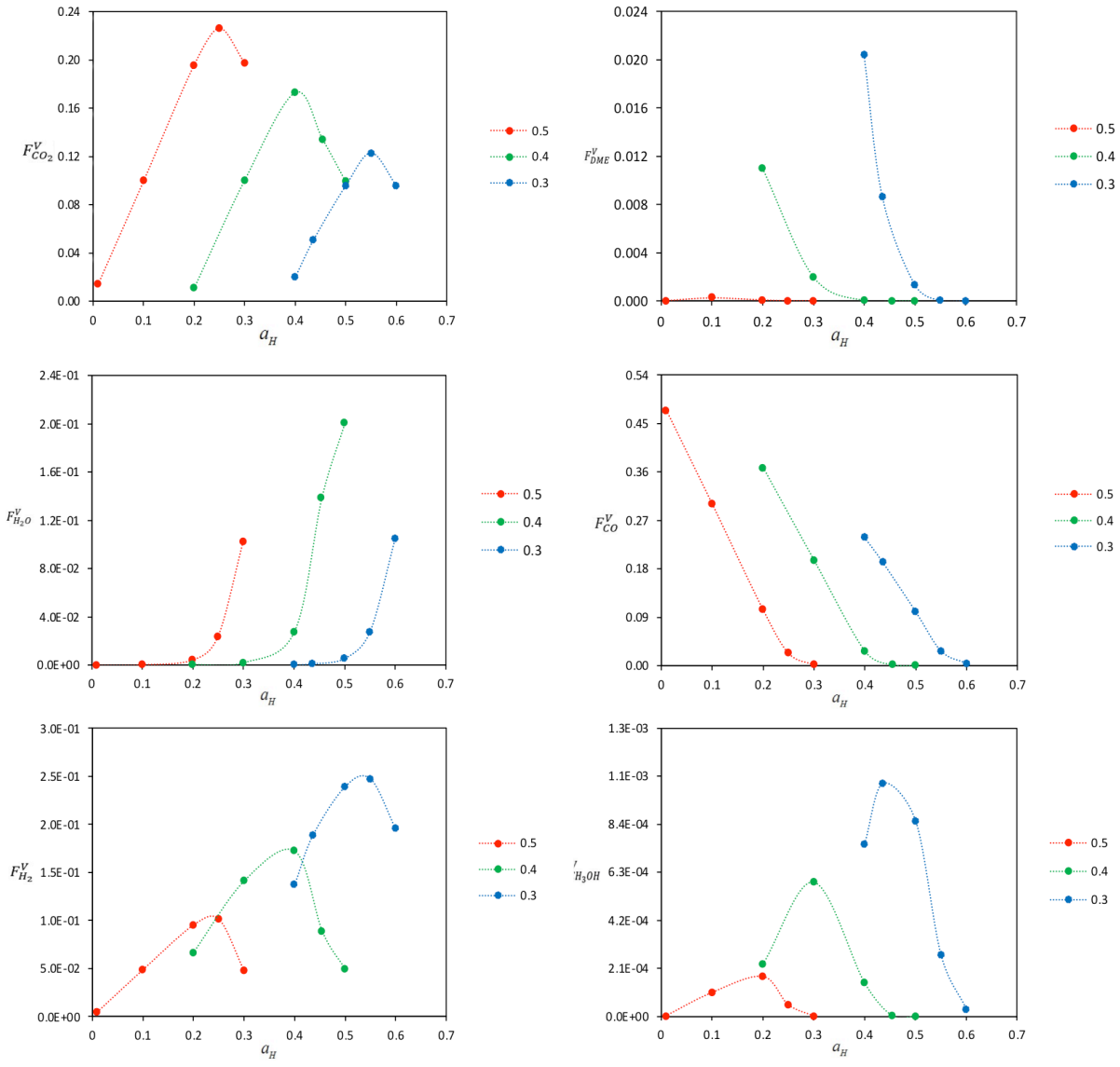

Figure 2.7: $F_j^{(V)}$(dashed, left) iso- a_O lines as a_H functions, T=300°C, P=10 bar

As the pressure is increased to 40 bar at a constant temperature of 300°C, the overall production of DME and CH_3OH increases. The maximum $F_{DME}^{(V)}$ = 0.052 occurs at (a_H, a_O) = (0.4, 0.3) and decreases for larger a_H values, as shown in **Figure 2.8**, whereas for CH_3OH, the maximum $F_{CH_3OH}^{(V)}$ = 0.0047 is achieved at (a_H, a_O) = (0.5, 0.3). CO and H_2O exhibit a similar trend at 300°C and 10 bar, namely that more CO is produced at a lower a_H and more water is produced at a higher a_H for all a_O. As the pressure is increased to 80 bar, all the species have a similar trend where DME and CH_3OH production increases to $F_{DME}^{(V)}$= 0.06 and $F_{CH_3OH}^{(V)}$ = 0.0075 at (a_H, a_O) = (0.4, 0.3).

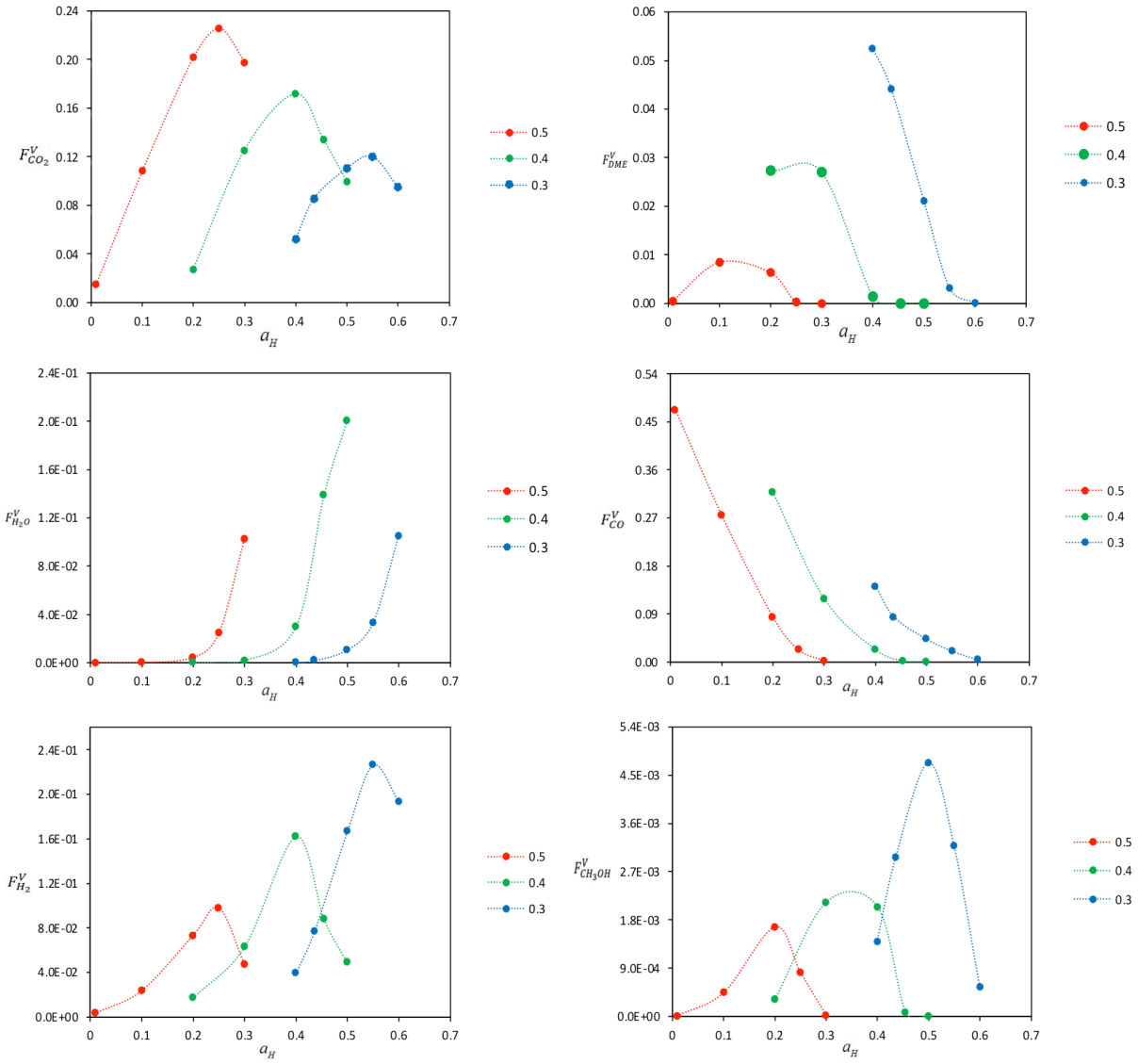

Figure 2.8: $F_j^{(V)}$(dashed, left) iso- a_O lines as a_H functions, T=300°C, P=40 bar

Since low a_O is beneficial for DME production, lower a_O values were tested. For a_O =0.17 and a_H =0.67, which are near the edge of the attainable region, and T = 100°C, P = 40 bar, DME and water make up over 90% of the products in the liquid phase with $F_{DME}^{(L)}$ = 0.0779, $F_{H_2O}^{(L)}$ = 0.0779 and $F_{CH_3OH}^{(L)}$ = 0.0108. In the vapor phase, there is a negligible amount of DME and hydrogen production with $F_{DME}^{(V)}$ = 2.56E-05 and $F_{H_2}^{(V)}$= 2.87E-05. **Table 2.2** shows the mole

fractions of the six species (CO, CO_2, H_2, CH_3OH, CH_3OCH_3 and H_2O) at the most promising a_H and a_O for each temperature and pressure, $T\left(^oC\right)\in\{100,200,300\}$ and $P(bar)\in\{10,40,80\}$, where DME production is maximized and CH_3OH production is minimized. At a_O=0.3 and a_H =0.435, DME and CO_2 production counts for over 90% of the products at all temperatures and pressures. When a_H decreases to a_H =0.4, DME and CO_2 production are almost the same, while CO production counts for over 40% of the most produced product, at all temperatures and pressures.

Table 2.2: Mole fractions of the six species at different operating points in $\left(a_H, a_O, T, P\right)$ space

T (°C)	P (bar)	a_H	a_O		CO_2	CO	H_2	H_2O	CH_3OH	CH_3OCH_3
100	10	0.435	0.3	x_i	0	0	0	0	0	0
				y_i	0.606	0.008	0.007	0.0002	0.0001	0.378
	40	0.4	0.3	x_i	0	0	0	0	0	0
				y_i	0.286	0.429	2.7E-06	9.0E-10	1.9E-06	0.286
		0.435	0.3	x_i	0	0	0	0	0	0
				y_i	0.612	0.003	0.002	0.0001	0.001	0.382
		0.67	0.17	x_i	5.8E-05	4.3E-08	8.5E-07	0.468	0.065	0.467
				y_i	0.0001	9.3E-07	0.510	0.024	0.010	0.455
	80	0.435	0.3	x_i	0.615	0.008	3.9E-10	5.4E-05	0.001	0.384
				y_i	0	0	0	0	0	0
200	10	0.4	0.3	x_i	0	0	0	0	0	0
				y_i	0.265	0.441	0.028	7.34-05	0.001	0.265

	40	0.435	0.3	x_i	0	0	0	0	0	0
				y_i	0.554	0.053	0.043	0.002	0.005	0.341
	80	0.435	0.3	x_i	0	0	0	0	0	0
				y_i	0.578	0.032	0.022	0.002	0.006	0.358
300	10	0.4	0.3	x_i	0	0	0	0	0	0
				y_i	0.048	0.571	0.329	0.001	0.002	0.048
	40	0.4	0.3	x_i	0	0	0	0	0	0
				y_i	0.181	0.493	0.138	0.001	0.005	0.182
	80	0.4	0.3	x_i	0	0	0	0	0	0
				y_i	0.234	0.461	0.064	0.001	0.005	0.235

2.6 Conclusions

Gibbs free energy minimization based equilibrium studies of a six-species (CO, CO_2, H_2, CH_3OH, CH_3OCH_3 and H_2O), three-atom (C, H, O) mixture have been carried out for various inlet hydrogen and oxygen atom-mol fractions $\left(a_H, a_O\right)$, for the temperature and pressure ranges, $T\left({}^{o}C\right) \in \{100, 200, 300\}$ and $P\left(bar\right) \in \{10, 40, 80\}$. The obtained results are expressed in terms of vapor and liquid molar moles of product species per total atom-mol in each phase *k*, $F_j^{(k)}$, and identify promising operating points in $\left(a_H, a_O, T, P\right)$ space for DME production. For an additional process objective of little to no CH_3OH formation, three operating points seem promising:

1. (a_H, a_O, T, P) = (0.4, 0.3, 100°C, 40 bar), which features equimolar DME and CO_2 product formation ($F_{DME}^{(V)} = F_{CO_2}^{(V)} = 0.0667$) in the vapor phase
2. (a_H, a_O, T, P) = (0.435, 0.3, 100°C, 40 bar), which features higher DME ($F_{DME}^{(V)} = 0.0724$) and CO_2 ($F_{CO_2}^{(V)} = 0.1158$) values in the vapor phase, and
3. (a_H, a_O, T, P)= (0.435, 0.3, 200°C, 40 bar), which features a CO_2 and DME production in the vapor phase with $F_{CO_2}^{(V)} = 0.112$ and $F_{DME}^{(V)} = 0.069$

The third operating point is more realistic for an industrial process since it is in the range of commercial operating conditions of 35-100 bar and 200-300°C [61–64]. For such a process, CO_2 will need to be separated, and recycled, to prevent CO_2 emissions.

CHAPTER 3: Equilibrium Analysis of Acetic Acid Production from Carbon Dioxide in C-H-O Atom-Mol Fraction Space

3.1 Introduction

Acetic acid is one of the most important intermediate in the chemical industry and it has been used in the production of different chemicals such as vinyl acetate and acetic anhydride [94–96]. Given its multiple application, the global market of acetic acid was estimated to be 14.4 Mt in 2017, and it is estimated to reach 18.2 Mt by 2023 [97]. Different biological and chemical processes are employed to synthesize acetic acid, and one of these processes is aerobic fermentation of ethanol which is the process currently used for vinegar production [98]. Commercially, acetic acid was first produced by oxidation of acetaldehyde over heterogeneous catalyst of manganese or cobalt acetate [99]. However, due to the toxicity of the organo-mercury compound catalyst that was used for the production of acetaldehyde from acetylene, this process was phased out. Thus, different heterogeneous and homogenous processes were developed to reduce the emission of toxic materials, energy consumption, and cost of raw materials [100–103].

One of these processes is the Hoechst-Waker process, which is based on the direct oxidation of ethylene in the vapor phase over palladium metal combined with heteropolyacid catalyst at 160-210 °C [99]. This process exhibited high selectivity toward acetic acid and did not produce toxic materials, but was energy intensive due to the required separation of different byproducts. Other processes have been investigated for acetic acid production that were based on the oxidation of hydrocarbons such as n-butane and naphtha [104–107]. Nevertheless, these processes produce major byproducts such as formic acid and propionic acid, which require further separation and make the processes economically unfavorable. Currently, acetic acid is

produced commercially via the carbonylation of methanol in the liquid phase, which counts for over 75% of produced acetic acid globally [108].

Many chemical companies such as BASF, Monsanto, and BP chemicals (CATIVA), have their own patented processes utilizing different catalysts to produce acetic acid with over 90% yield. In the BASF process, a homogenous cobalt based catalyst with iodine promoter is utilized at high pressure of 600-800 bar and temperature of 230 °C [109]. The acetic acid yield in the BASF process is ~70% and ~90% based on CO and methanol reactants, respectively, and the main byproducts are methane and ethanol. Monsanto developed an improved process to produce acetic acid using rhodium based catalyst with iodide promoter at 30-50 bar and temperature of 150-200 °C, conditions that are milder than those employed in the BASF process [110]. In 1996, BP Chemical further improved the Monsanto process by utilizing iridium based catalyst, which allows a lower water content in the reactant mixture, improves the stability and activity of the catalyst, and leads to lower byproduct formation [111].

In recent years, more studies have focused on developing a greener route for acetic acid synthesis from abundant carbon dioxide (CO_2) [112–114]. He et al. have used iron nanoparticle catalyst in presence of water at 200 °C to produce acetic acid; however, it suffers from low activity and selectivity [115]. Recently, utilizing methane as a hydrogen source for acetic acid production received much attention, where acetic acid is formed over heterogeneous Pd/carbon and Pt/Alumina catalysts [116]. Nevertheless, utilizing methane requires harsh operating conditions due to unfavorable thermodynamics making the transformation impractical. A novel process has been reported by Qian et al., where methanol, CO_2, and H_2 are used to produce acetic acid over a ruthenium-rhodium bimetallic homogenous catalyst in the presence of imidazole as

the ligand and lithium iodide as the promoter [117]. Qian et al. findings revealed a new way to produce acetic acid utilizing CO_2 and methanol.

In this work, the Gibbs free energy minimization method is employed to carry out chemical-phase equilibrium analysis for acetic acid synthesis, by defining the feed in terms of atom-mole fractions. To this end, first the feed's Attainable Region (AR) in atom-mole space is defined, which has been earlier utilized by our group [28], and contains all possible atom-mol fractions that can be obtained using a list of species than can comprise the feed. Next, Gibbs free energy minimization is carried out for different feasible points within the feed's AR, and different temperatures and pressures. Its results yield the atom-mol fractions, temperature, and pressure at which acetic acid production is maximized.

3.2 Construction of Attainable Region (AR) In Atom-Mol Fraction Space for CO-CO_2-H_2-CH_3OH -H_2O Mixtures

To define the Attainable Region (AR), a five-component mixture and three atoms are considered for the feed, excluding acetic acid and methyl acetate since they are considered as products only. This five-components mixture consists of the following species and elements $\{(1)CO;(2)CO_2;(3)H_2;(4)CH_3OH;(5)H_2O\}$, $\{(1)C;(2)H;(3)O\}$.

Theorem:

A linear variety is considered in the atom-mol fraction space $\{(a_C, a_H, a_O) \in \mathbb{R}^3, a_C + a_H + a_O = 1\}$ for the five-component mixture

$\{(1)CO;(2)CO_2;(3)H_2;(4)CH_3OH;(5)H_2O\}$.

To reduce the atom-mol fraction space to $\left\{\left(a_H, a_O\right) \in \mathbb{R}^2\right\}$, $a_C = 1 - a_H - a_O$ is substituted to enable quantification of the mixture's AR in the reduced form as:

$$\left\{\begin{array}{l} 0 \le -a_H - a_O + 1, \\ 0 \le -\frac{3}{2} a_H - 3a_O + 2 \\ -\frac{5}{4} a_H - 2a_O + 1 \le 0, \\ 0 \le a_H + 2a_O - 1, \\ a_H \ge 0, a_O \ge 0, \\ a_C = 1 - a_H - a_O \end{array}\right\}$$

Proof.

The point $\left(a_C, a_H, a_O\right) \in \mathbb{R}^3$ belongs to the AR in the atom-mol fraction space $\left\{\left(a_C, a_H, a_O\right) \in \mathbb{R}^3\right\}$, if and only if there exists $\left(F_1, F_2, F_3, F_4, F_5\right)$ such that:

$$\left\{\begin{array}{l} a_C = F_1 + F_2 + F_4 \\ a_H = 2F_3 + 4F_4 + 2F_5 \\ a_O = F_1 + 2F_2 + F_4 + F_5 \\ F_1 \ge 0,\ F_2 \ge 0,\ F_3 \ge 0,\ F_4 \ge 0,\ F_5 \ge 0 \\ a_C \ge 0, a_H \ge 0, a_O \ge 0, a_C + a_H + a_O = 1 \end{array}\right\} \Leftrightarrow$$

$$\left\{\begin{array}{l} F_4 = a_C - F_1 - F_2 \\ F_3 = \frac{1}{2} a_H - 2F_4 - F_5 \\ F_5 = a_O - F_1 - 2F_2 - F_4 \\ F_1 \ge 0,\ F_2 \ge 0,\ F_3 \ge 0,\ F_4 \ge 0,\ F_5 \ge 0 \\ a_C \ge 0, a_H \ge 0, a_O \ge 0, a_C + a_H + a_O = 1 \end{array}\right\} \Leftrightarrow$$

$$\left\{\begin{array}{l} F_4 = a_C - F_1 - F_2 \\ F_3 = \dfrac{1}{2}a_H - a_O + F_1 + 2F_2 - F_4 \\ F_5 = a_O - F_1 - 2F_2 - F_4 \\ F_1 \geq 0,\ F_2 \geq 0,\ F_3 \geq 0,\ F_4 \geq 0,\ F_5 \geq 0 \\ a_C \geq 0, a_H \geq 0, a_O \geq 0, a_C + a_H + a_O = 1 \end{array}\right\} \Leftrightarrow$$

$$\left\{\begin{array}{l} F_4 = a_C - F_1 - F_2 \\ F_3 = \dfrac{1}{2}a_H - a_O + F_1 + 2F_2 - \left(a_C - F_1 - F_2\right) \\ F_5 = a_O - F_1 - 2F_2 - \left(a_C - F_1 - F_2\right) \\ F_1 \geq 0,\ F_2 \geq 0,\ F_3 \geq 0,\ F_4 \geq 0,\ F_5 \geq 0 \\ a_C \geq 0, a_H \geq 0, a_O \geq 0, a_C + a_H + a_O = 1 \end{array}\right\} \Leftrightarrow$$

$$\left\{\begin{array}{l} F_4 = a_C - F_1 - F_2 \\ F_3 = \dfrac{1}{2}a_H - a_O + F_1 + 2F_2 - a_C + F_1 + F_2 \\ F_5 = a_O - F_1 - 2F_2 - a_C + F_1 + F_2 \\ F_1 \geq 0,\ F_2 \geq 0,\ F_3 \geq 0,\ F_4 \geq 0,\ F_5 \geq 0 \\ a_C \geq 0, a_H \geq 0, a_O \geq 0, a_C + a_H + a_O = 1 \end{array}\right\} \Leftrightarrow$$

$$\left\{\begin{array}{l} F_4 = a_C - F_1 - F_2 \\ F_3 = \dfrac{1}{2}a_H - a_O - a_C + 2F_1 + 3F_2 \\ F_5 = a_O - a_C - F_2 \\ F_1 \geq 0,\ F_2 \geq 0,\ F_3 \geq 0,\ F_4 \geq 0,\ F_5 \geq 0 \\ a_C \geq 0, a_H \geq 0, a_O \geq 0, a_C + a_H + a_O = 1 \end{array}\right\} \overset{a_C = 1 - a_H - a_O}{\Leftrightarrow}$$

$$\left\{\begin{array}{l} F_4 = \left(1 - a_H - a_O\right) - F_1 - F_2 \\ F_3 = \frac{1}{2}a_H - a_O - \left(1 - a_H - a_O\right) + 2F_1 + 3F_2 \\ F_5 = a_O - \left(1 - a_H - a_O\right) - F_2 \\ F_1 \geq 0,\ F_2 \geq 0,\ F_3 \geq 0,\ F_4 \geq 0,\ F_5 \geq 0 \\ a_C \geq 0, a_H \geq 0, a_O \geq 0, a_C + a_H + a_O = 1 \end{array}\right\} \Leftrightarrow$$

$$\left\{\begin{array}{l} F_4 = -a_H - a_O - F_1 - F_2 + 1 \\ F_3 = \frac{3}{2}a_H + 2F_1 + 3F_2 - 1 \\ F_5 = a_H + 2a_O - F_2 - 1 \\ F_1 \geq 0,\ F_2 \geq 0, \\ \frac{3}{2}a_H + 2F_1 + 3F_2 - 1 \geq 0, \\ -a_H - a_O - F_1 - F_2 + 1 \geq 0, \\ a_H + 2a_O - F_2 - 1 \geq 0 \\ a_C \geq 0, a_H \geq 0, a_O \geq 0, a_C + a_H + a_O = 1 \end{array}\right\} \Leftrightarrow$$

$$\left\{\begin{array}{l} F_4 = -a_H - a_O - F_1 - F_2 + 1 \\ F_3 = \frac{3}{2}a_H + 2F_1 + 3F_2 - 1 \\ F_5 = a_H + 2a_O - F_2 - 1 \\ F_1 \geq 0,\ F_2 \geq 0, \\ F_2 \geq -\frac{1}{2}a_H - \frac{2}{3}F_1 + \frac{1}{3}, \\ F_2 \leq -a_H - a_O - F_1 + 1, \\ F_2 \leq a_H + 2a_O - 1 \\ a_C \geq 0, a_H \geq 0, a_O \geq 0, a_C + a_H + a_O = 1 \end{array}\right\} \Leftrightarrow$$

$$\left\{\begin{array}{l} F_4 = -a_H - a_O - F_1 - F_2 + 1 \\ F_3 = \frac{3}{2}a_H + 2F_1 + 3F_2 - 1 \\ F_5 = a_H + 2a_O - F_2 - 1 \\ F_1 \geq 0, \\ \max\left[\begin{array}{l} 0, \\ -\frac{1}{2}a_H - \frac{2}{3}F_1 + \frac{1}{3} \end{array}\right] \leq F_2 \leq \min\left[\begin{array}{l} -a_H - a_O - F_1 + 1, \\ a_H + 2a_O - 1 \end{array}\right], \\ a_C \geq 0, a_H \geq 0, a_O \geq 0, a_C + a_H + a_O = 1 \end{array}\right\} \Leftrightarrow$$

$$\left\{\begin{array}{l} F_4 = -a_H - a_O - F_1 - F_2 + 1 \\ F_3 = \frac{3}{2}a_H + 2F_1 + 3F_2 - 1 \\ F_5 = a_H + 2a_O - F_2 - 1 \\ F_1 \geq 0, \\ \max\left[\begin{array}{l} 0, \\ -\frac{1}{2}a_H - \frac{2}{3}F_1 + \frac{1}{3} \end{array}\right] \leq F_2 \leq \min\left[\begin{array}{l} -a_H - a_O - F_1 + 1, \\ a_H + 2a_O - 1 \end{array}\right], \\ 0 \leq -a_H - a_O - F_1 + 1, \\ 0 \leq a_H + 2a_O - 1, \\ -\frac{1}{2}a_H - \frac{2}{3}F_1 + \frac{1}{3} \leq -a_H - a_O - F_1 + 1, \\ -\frac{1}{2}a_H - \frac{2}{3}F_1 + \frac{1}{3} \leq a_H + 2a_O - 1 \\ a_C \geq 0, a_H \geq 0, a_O \geq 0, a_C + a_H + a_O = 1 \end{array}\right\} \Leftrightarrow$$

$$\left\{\begin{array}{l} \\ F_4 = -a_H - a_O - F_1 - F_2 + 1 \\ F_3 = \dfrac{3}{2}a_H + 2F_1 + 3F_2 - 1 \\ F_5 = a_H + 2a_O - F_2 - 1 \\ \max\begin{bmatrix} 0, \\ -\dfrac{1}{2}a_H - \dfrac{2}{3}F_1 + \dfrac{1}{3} \end{bmatrix} \le F_2 \le \min\begin{bmatrix} -a_H - a_O - F_1 + 1, \\ a_H + 2a_O - 1 \end{bmatrix}, \\ \max\begin{bmatrix} 0, \\ -\dfrac{9}{4}a_H - 3a_O + 2 \end{bmatrix} \le F_1 \le \min\begin{bmatrix} -a_H - a_O + 1, \\ -\dfrac{3}{2}a_H - 3a_O + 2 \end{bmatrix} \\ 0 \le a_H + 2a_O - 1, \\ a_C \ge 0, a_H \ge 0, a_O \ge 0, a_C + a_H + a_O = 1 \end{array}\right\} \Leftrightarrow$$

$$\left\{\begin{array}{l} \\ F_4 = -a_H - a_O - F_1 - F_2 + 1 \\ F_3 = \dfrac{3}{2}a_H + 2F_1 + 3F_2 - 1 \\ F_5 = a_H + 2a_O - F_2 - 1 \\ \max\begin{bmatrix} 0, \\ -\dfrac{1}{2}a_H - \dfrac{2}{3}F_1 + \dfrac{1}{3} \end{bmatrix} \le F_2 \le \min\begin{bmatrix} -a_H - a_O - F_1 + 1, \\ a_H + 2a_O - 1 \end{bmatrix}, \\ \max\begin{bmatrix} 0, \\ -\dfrac{9}{4}a_H - 3a_O + 2 \end{bmatrix} \le F_1 \le \min\begin{bmatrix} -a_H - a_O + 1, \\ -\dfrac{3}{2}a_H - 3a_O + 2 \end{bmatrix} \\ 0 \le a_H + 2a_O - 1, \\ a_C \ge 0, a_H \ge 0, a_O \ge 0, a_C + a_H + a_O = 1 \end{array}\right\} \Leftrightarrow$$

$$\left\{\begin{array}{l} F_4 = -a_H - a_O - F_1 - F_2 + 1 \\ F_3 = \frac{3}{2}a_H + 2F_1 + 3F_2 - 1 \\ F_5 = a_H + 2a_O - F_2 - 1 \\ \max\left[\begin{array}{l} 0, \\ -\frac{1}{2}a_H - \frac{2}{3}F_1 + \frac{1}{3} \end{array}\right] \le F_2 \le \min\left[\begin{array}{l} -a_H - a_O - F_1 + 1, \\ a_H + 2a_O - 1 \end{array}\right], \\ \max\left[\begin{array}{l} 0, \\ -\frac{9}{4}a_H - 3a_O + 2 \end{array}\right] \le F_1 \le \min\left[\begin{array}{l} -a_H - a_O + 1, \\ -\frac{3}{2}a_H - 3a_O + 2 \end{array}\right] \\ 0 \le -a_H - a_O + 1, \\ 0 \le -\frac{3}{2}a_H - 3a_O + 2 \\ -\frac{9}{4}a_H - 3a_O + 2 \le -a_H - a_O + 1, \\ -\frac{9}{4}a_H - 3a_O + 2 \le -\frac{3}{2}a_H - 3a_O + 2 \\ 0 \le a_H + 2a_O - 1, \\ a_C \ge 0, a_H \ge 0, a_O \ge 0, a_C + a_H + a_O = 1 \end{array}\right\} \Leftrightarrow$$

$$\left\{\begin{array}{l} F_4 = -a_H - a_O - F_1 - F_2 + 1 \\ F_3 = \frac{3}{2} a_H + 2F_1 + 3F_2 - 1 \\ F_5 = a_H + 2a_O - F_2 - 1 \\ \max\begin{bmatrix} 0, \\ -\frac{1}{2} a_H - \frac{2}{3} F_1 + \frac{1}{3} \end{bmatrix} \le F_2 \le \min\begin{bmatrix} -a_H - a_O - F_1 + 1, \\ a_H + 2a_O - 1 \end{bmatrix}, \\ \max\begin{bmatrix} 0, \\ -\frac{9}{4} a_H - 3a_O + 2 \end{bmatrix} \le F_1 \le \min\begin{bmatrix} -a_H - a_O + 1, \\ -\frac{3}{2} a_H - 3a_O + 2 \end{bmatrix} \\ 0 \le -a_H - a_O + 1, \\ 0 \le -\frac{3}{2} a_H - 3a_O + 2 \\ -\frac{5}{4} a_H - 2a_O + 1 \le 0, \\ \frac{3}{4} a_H \ge 0 \\ 0 \le a_H + 2a_O - 1, \\ a_C \ge 0, a_H \ge 0, a_O \ge 0, a_C + a_H + a_O = 1 \end{array}\right\} \Leftrightarrow$$

$$
\left\{
\begin{array}{l}
F_4 = -a_H - a_O - F_1 - F_2 + 1 \\
F_3 = \dfrac{3}{2} a_H + 2F_1 + 3F_2 - 1 \\
F_5 = a_H + 2a_O - F_2 - 1 \\
\\
\max\left[\begin{array}{l} 0, \\ -\dfrac{1}{2} a_H - \dfrac{2}{3} F_1 + \dfrac{1}{3} \end{array}\right] \le F_2 \le \min\left[\begin{array}{l} -a_H - a_O - F_1 + 1, \\ a_H + 2a_O - 1 \end{array}\right], \\
\max\left[\begin{array}{l} 0, \\ -\dfrac{9}{4} a_H - 3a_O + 2 \end{array}\right] \le F_1 \le \min\left[\begin{array}{l} -a_H - a_O + 1, \\ -\dfrac{3}{2} a_H - 3a_O + 2 \end{array}\right] \\
0 \le -a_H - a_O + 1, \\
0 \le -\dfrac{3}{2} a_H - 3a_O + 2 \\
-\dfrac{5}{4} a_H - 2a_O + 1 \le 0, \\
0 \le a_H + 2a_O - 1, \\
a_H \ge 0, a_O \ge 0, \\
a_C = 1 - a_H - a_O
\end{array}
\right\}
$$

The AR given by the above set of inequalities is graphically illustrated in **Figure 3.1**. The AR (shaded area) is a polygon in $\left(a_H, a_O\right)$ space with vertices (0, 0.5), (0,0.667), (0.667, 0.367) and (1, 0). The AR shown in Figure 1 will subsequently be investigated to identify regions in $\left(a_H, a_O\right)$ space that yields the maximum acetic acid production.

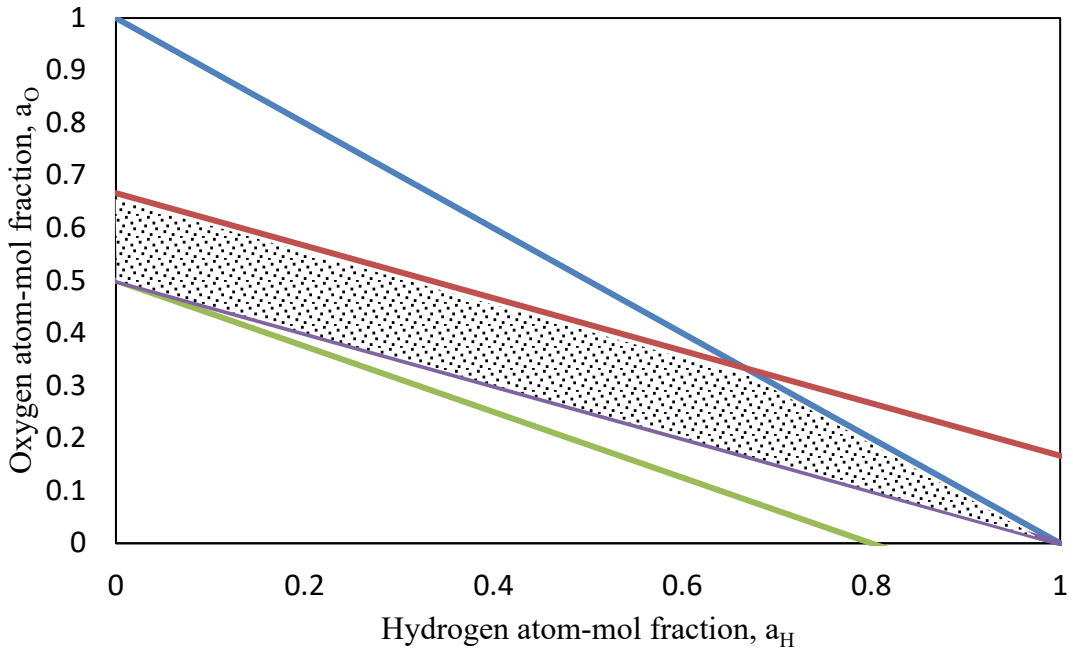

Figure 3.1: AR in atom mol-fraction space of {CO, CO_2, H_2, CH_3OH, H_2O}

3.3 Thermodynamic Studies of Acetic acid Synthesis Using Total Gibbs Free Energy Minimization in Atom-Mol Fraction Space

In this work, the total Gibbs free energy minimization method is utilized to identify and study the equilibrium behavior of a mixture consisting of seven species: CO, CO_2, H_2, CH_3OH, H_2O, CH_3COOH, and $C_3H_6O_2$. The total Gibbs free energy minimization method states that at constant pressure and temperature, a system reaches chemical and phase equilibrium, if and only if the system's total Gibbs free energy is at its minimum. To reduce the number of variables for the equilibrium analysis, the analysis is conducted in atom mole fraction space $\left(a_C, a_H, a_O\right)$ at different combination of temperatures and pressures. The total Gibbs free energy minimization problem, presented below, is solved at different operating conditions at $\left(a_H, a_O, T, P\right)$ space to determine the points that yield the maximum production of acetic acid.

$$\left\{\begin{array}{l}\overline{\pi}\left(T,P,\left\{\overline{a}_i\right\}_{i=1}^{NE}\right)\triangleq\min\limits_{\left\{n_j^{(k)}\right\}_{(j,k)=(1,1)}^{(NC,NP)}}\overline{G}\left(T,P,\left\{n_j^{(k)}\right\}_{(j,k)=(1,1)}^{(NC,NP)}\right)\\ \qquad s.t.\\ \qquad \overline{a}_i-\sum\limits_{k}^{NP}\sum\limits_{j}^{NC}\nu_{i,j}n_j^{(k)}=0\quad\forall i=1,NE\\ \qquad n_j^{(k)}\geq 0\quad\forall j=1,NC;\quad\forall k=1,NP\end{array}\right\}\Leftrightarrow$$

$$\left\{\begin{array}{l}\overline{\pi}\left(T,P,\left\{\overline{a}_i\right\}_{i=1}^{NE}\right)\triangleq\min\limits_{\left\{n_j^{(k)}\right\}_{(j,k)=(1,1)}^{(NC,NP)}}\sum\limits_{k=1}^{NP}\sum\limits_{j=1}^{NC}n_j^{(k)}\mu_j^{(k)}\left(T,P,\left\{\dfrac{n_j^{(k)}}{\sum\limits_{p=1}^{NC}n_p^{(k)}}\right\}_{j=1}^{NC}\right)\\ \qquad s.t.\\ \qquad \overline{a}_i-\sum\limits_{k}^{NP}\sum\limits_{j}^{NC}\nu_{i,j}n_j^{(k)}=0\quad\forall i=1,NE\\ \qquad n_j^{(k)}\geq 0\quad\forall j=1,NC;\quad\forall k=1,NP\end{array}\right\}\Leftrightarrow$$

$$\left\{\begin{array}{l}\overline{\pi}\left(T,P,\left\{\overline{a}_i\right\}_{i=1}^{NE}\right)\triangleq\min\limits_{\left\{n_j^{(k)}\right\}_{(j,k)=(1,1)}^{(NC,NP)}}\sum\limits_{k=1}^{NP}\sum\limits_{j=1}^{NC}n_j^{(k)}\left(G_j^o\left(T\right)+RT\ln\dfrac{\hat{f}_j^{(k)}}{f_j^o}\right)\\ \qquad s.t.\\ \qquad \overline{a}_i-\sum\limits_{k}^{NP}\sum\limits_{j}^{NC}\nu_{i,j}n_j^{(k)}=0\quad\forall i=1,NE\\ \qquad n_j^{(k)}\geq 0\quad\forall j=1,NC;\quad\forall k=1,NP\end{array}\right\}$$

At a fixed temperature and pressure, $\overline{G}\left(T,P,\left\{n_j^{(k)}\right\}_{(j,k)=(1,1)}^{(NC,NP)}\right)$ function is a first order homogenous function and that means the following relation holds true: $\overline{G}\left(T,P,\left\{n_j^{(k)}\right\}_{(j,k)=(1,1)}^{(NC,NP)}\right)=\overline{a}_T\sum\limits_{k=1}^{NP}\sum\limits_{j=1}^{NC}F_j^{(k)}\left(G_j^o\left(T\right)+RT\ln\dfrac{\hat{f}_j^{(k)}}{f_j^o}\right)$ where $\overline{a}_T\triangleq\sum\limits_{i=1}^{NE}\overline{a}_i$, $a_i\triangleq\dfrac{\overline{a}_i}{\overline{a}_T}$,

$F_j^{(k)} \triangleq \dfrac{n_j^{(k)}}{\overline{a}_T}$. Then, the above optimization problem's optimum satisfies: $\overline{\pi}\left(T,P,\left\{\overline{a}_i\right\}_{i=1}^{NE}\right) \triangleq \overline{a}_T \cdot \pi\left(T,P,\left\{a_i\right\}_{i=1}^{NE}\right)$, where the latter is defined as:

$$\left\{ \begin{array}{l} \pi\left(T,P,\left\{a_i\right\}_{i=1}^{NE}\right) \triangleq \min\limits_{\left\{F_j^{(k)}\right\}_{(j,k)=(1,1)}^{(NC,NP)}} \sum\limits_{k=1}^{NP}\sum\limits_{j=1}^{NC} F_j^{(k)}\left(G_j^o\left(T\right) + RT\ln\dfrac{\hat{f}_j^{(k)}}{f_j^o}\right) \\ \quad s.t. \\ \quad a_i - \sum\limits_{k}^{NP}\sum\limits_{j}^{NC} \nu_{i,j} F_j^{(k)} = 0 \qquad \forall i = 1, NE \\ \quad F_j^{(k)} \geq 0, \qquad \forall j = 1, NC; \quad \forall k = 1, NP \\ \quad \sum\limits_{i=1}^{NE} a_i = 1 \end{array} \right\}$$

To solve the total Gibbs free energy minimization problem, a thermodynamic model is required to determine the fugacity of each of the species in each phase. The fugacity $\hat{f}_j^V$ of species *j* in the vapor phase is calculated using its fugacity coefficient $\hat{\phi}_j$, while the fugacity $\hat{f}_j^L$ of species *j* in the liquid phase is calculated using its activity coefficient γ_j. To satisfy the optimization problem, it is required for these fugacities to be equal, which gives a rise to the below condition:

$$\left\{ \begin{array}{ll} \hat{f}_j^V = y_j\,\hat{\phi}_j\left(T,P,\left\{y_j\right\}_{j=1}^{NC}\right)P & \forall j = 1,\cdots,NC \\ \hat{f}_j^L = x_j\,\gamma_j\left(T,\left\{x_j\right\}_{j=1}^{NC}\right)P_j^{sat}\left(T\right) & \forall j = 1,\cdots,NC \\ \hat{f}_j^V = \hat{f}_j^L & \forall j = 1,\cdots,NC \end{array} \right\}$$

The equilibrium analysis was carried out using RGibbs Module in Aspen Plus software and its Non-Random Two-Liquid model (NRTL) physical property method [118–120]. The analysis was conducted for various reactor inlet atom-mol fractions at different temperature-pressure combinations of $T\left(^{o}C\right)\in\left\{100,150,200,250\right\}$ and $P\left(bar\right)\in\left\{10,30,50\right\}$. The obtained results are presented in the form of outlet vapor and liquid species molar flows per total atom-mol, $F_j^{(k)}$.

3.4 Results and Discussions

Figure 3.2 presents iso- a_O lines of mole over total atom-mol normalized ratios of the *i*th species for a_O values ranging from 0.3 to 0.5, and T (°C) = 100 and P = 10 bar. Acetic acid forms mostly in liquid phase along with water which makes the majority of the products. In liquid phase, the atom-mol normalized acetic acid production increases as a_O decreases reaching maximum of $F_{AA}^{(L)}=0.086$ at $(a_O,a_H)=(0.3,0.5)$ where over 85% of carbon is being utilized for acetic acid production. On the other hand, water production increases as a function of a_H and decreases as a function of a_O reaching maximum of $F_{H_2O}^{(L)}=0.263$ at $(a_O,a_H)=(0.3,0.667)$. At the maximum acetic acid production, its yield surpasses the water yield, $\frac{F_{AA}^{(L)}}{F_{H_2O}^{(L)}}=1.17$. In the vapor phase, CO_2 makes up most of the products, and CO_2 production increases as a_O increases reaching the maximum production of $F_{CO_2}^{(V)}=0.199$ at $(a_O,a_H)=(0.5,0.2)$. A similar trend is observed for CO where the maximum of $F_{CO}^{(V)}=0.267$ is achieved at $(a_O,a_H)=(0.4,0.2)$, and negligible amount is observed for CH_3OH, Methyl acetate, and H_2.

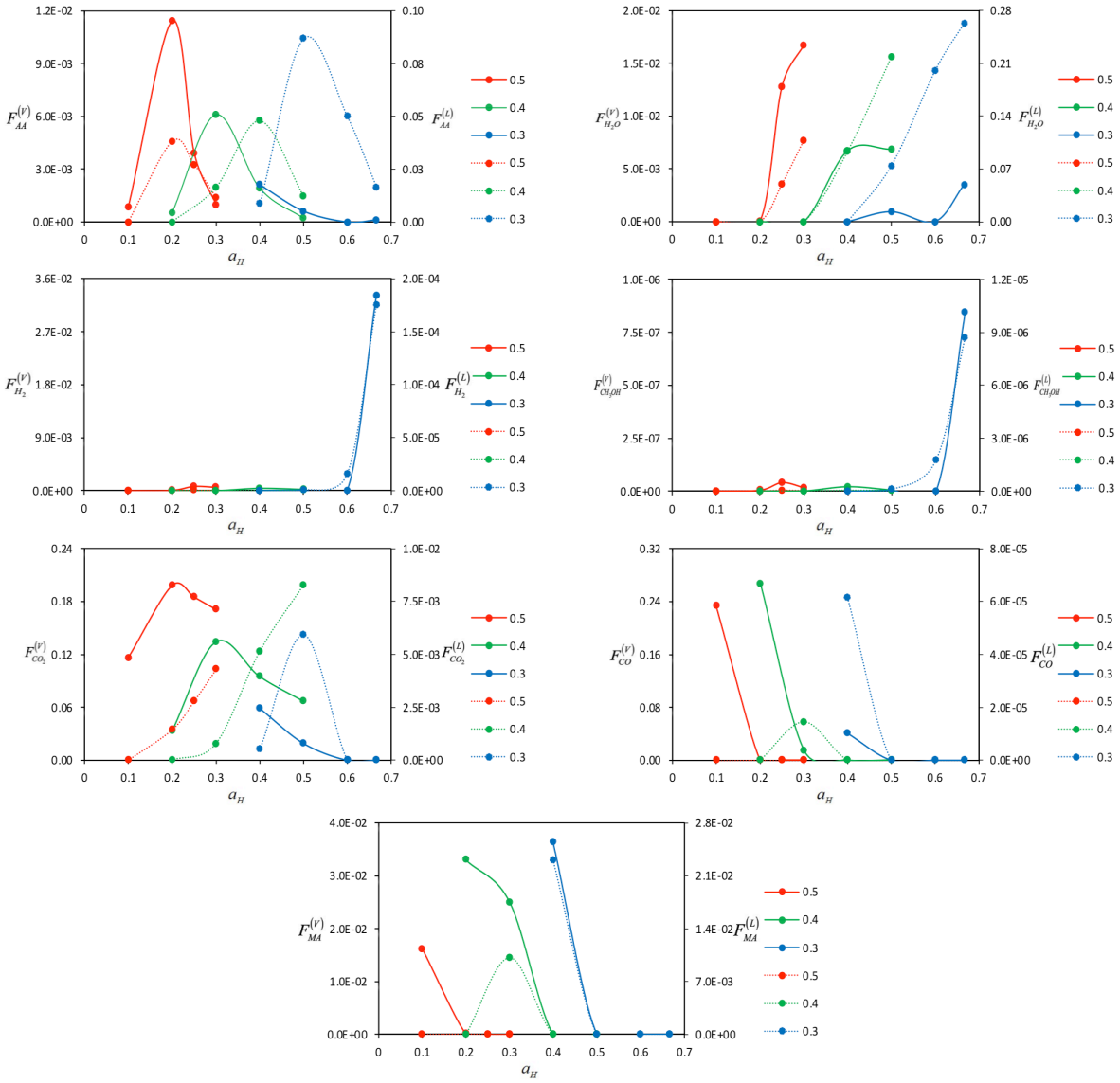

Figure 3.2: $F_j^{(V)}$(solid, left), $F_j^{(L)}$(dash, right) iso- a_O lines as a_H functions, T=100°C, P=10 bar

As the pressure increases from 10 bar to 30 bar, more products appear in the liquid phase, as illustrated in **Figure 3.3**. Acetic acid production in the liquid phase remains constant with $F_{AA}^{(L)} = 0.087$ at $(a_O, a_H) = (0.3, 0.5)$ and 87% of carbon is utilized. Conversely, acetic acid concentration in the liquid phase drops from 53% to 47% due to the fact that more CO_2 is formed. CO_2 production at $(a_O, a_H) = (0.3, 0.5)$ increases more than three folds, from

$F_{CO_2}^{(L)} = 0.006$ to $F_{CO_2}^{(L)} = 0.021$. As for water, it exhibits a similar trend as acetic acid where its production remains the same with $F_{H_2O}^{(L)} = 0.265$ at $(a_O, a_H) = (0.3, 0.667)$. The overall production in the vapor phase decreases; but, the maximum CO and CO_2 production continues to be almost the same with $F_{CO}^{(V)} = 0.267$ and $F_{CO_2}^{(V)} = 0.195$ at $(a_O, a_H) = (0.4, 0.2)$, and $(a_O, a_H) = (0.5, 0.2)$, respectively. The maximum production of methyl acetate, $F_{MA}^{(V)} = 0.033$, occurs at $(a_O, a_H) = (0.4, 0.2)$ compared to $(a_O, a_H) = (0.3, 0.4)$ at T (°C) = 100 and P = 10 bar.

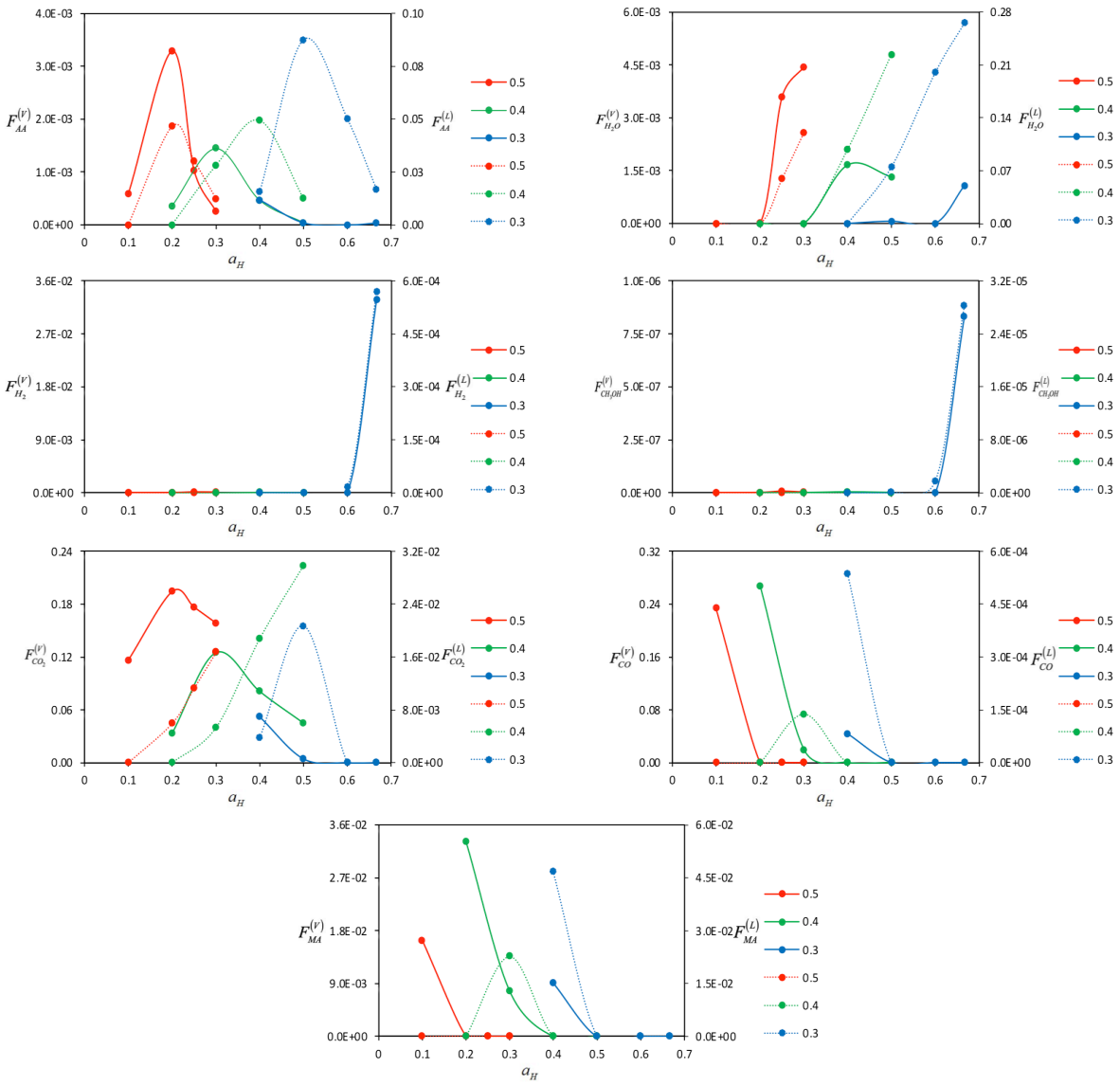

Figure 3.3: $F_j^{(V)}$(solid, left), $F_j^{(L)}$(dash, right) iso- $a_O$lines as a_H functions, T=100°C, P=30 bar

Figure 3.4 shows that the overall liquid production increases when the pressure is further increased to 50 bar; however, acetic acid and water production remain the same for almost all investigated a_O and a_H points. Thus, increasing pressure further is not beneficial to enhance acetic acid production at T (°C) = 100. On the contrary, CO_2 and CO production improve with increasing pressure reaching maximum of $F_{CO_2}^{(L)} = 0.055$ and $F_{CO}^{(L)} = 0.001$ at $(a_O, a_H) = (0.4, 0.5)$

and $(a_O, a_H) = (0.3, 0.4)$, respectively. In the vapor phase, acetic acid and water continue to decrease dramatically, although, CO_2 production stays constant with $F_{CO_2}^{(V)} = 0.189$ at $(a_O, a_H) = (0.5, 0.2)$. A small amount of CH_3OH, methyl acetate, and H_2 is observed in the vapor phase.

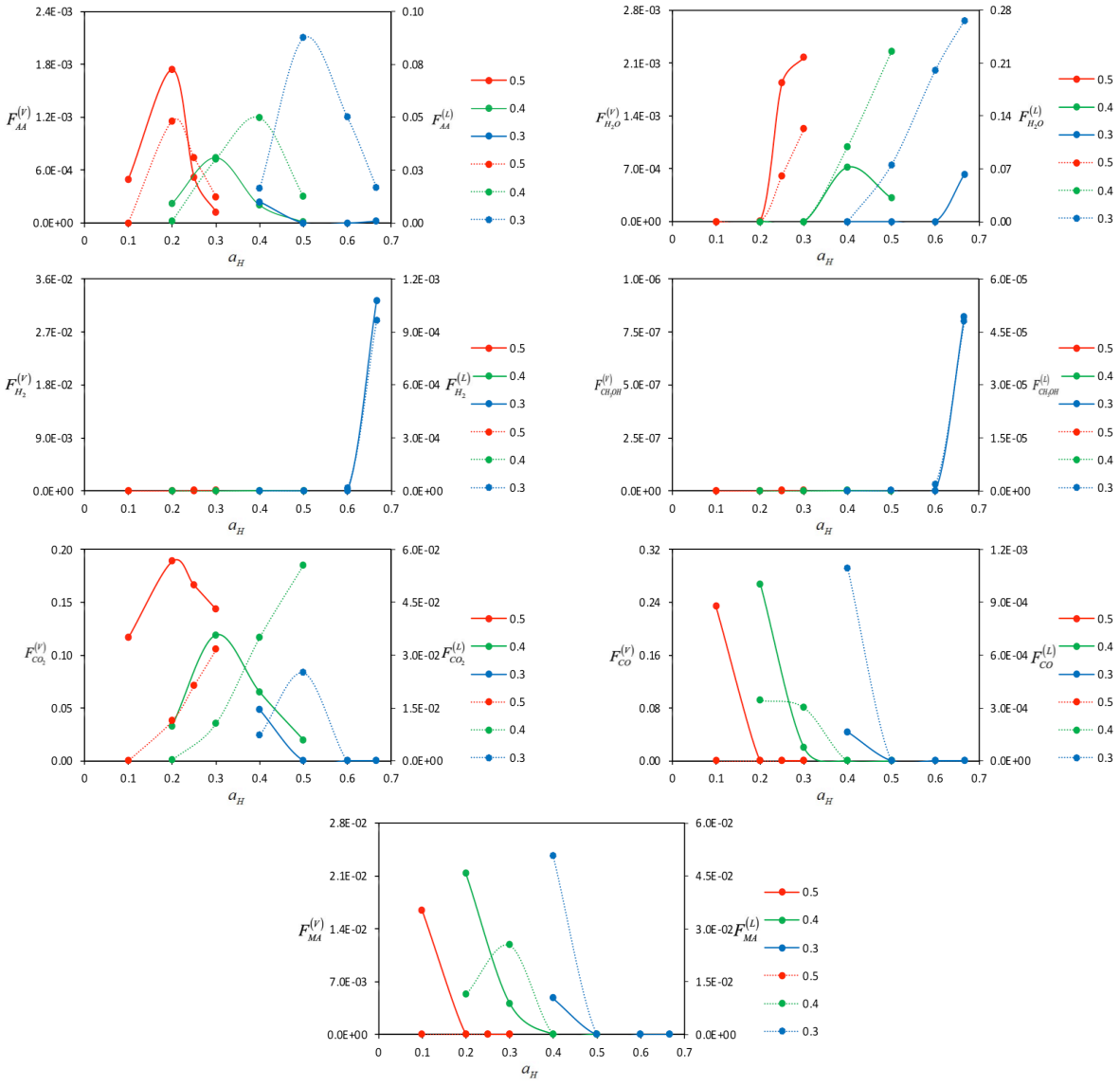

Figure 3.4: $F_j^{(V)}$(solid, left), $F_j^{(L)}$(dash, right) iso- a_O lines as a_H functions, T=100°C, P=50 bar

As the temperature is increased from 100°C to 150°C at a constant pressure of 10 bar, the overall liquid products decrease, as shown in **Figure 3.5**. In fact, the behavior of acetic acid and water production changes where it only forms at $a_O \leq 0.4$ compared to $a_O \leq 0.5$ at T (°C) = 100; however, the maximum production of $F_{AA}^{(L)} = 0.082$ still occurs at the same points $(a_O, a_H) = (0.3, 0.5)$. Similarly, water yield decreases at higher temperature reaching a maximum of $F_{H_2O}^{(L)} = 0.239$ at $(a_O, a_H) = (0.3, 0.667)$. In the vapor phase, CO_2 still makes up the majority of the product with a slight increase in the maximum production of $F_{CO_2}^{(V)} = 0.201$ at $(a_O, a_H) = (0.5, 0.2)$. The maximum CO production remains the same with $F_{CO}^{(V)} = 0.267$ at $(a_O, a_H) = (0.4, 0.2)$, and more H_2 starts to form compared to T (°C) = 100 with maximum of $F_{H_2}^{(V)} = 0.034$ at $(a_O, a_H) = (0.3, 0.667)$.

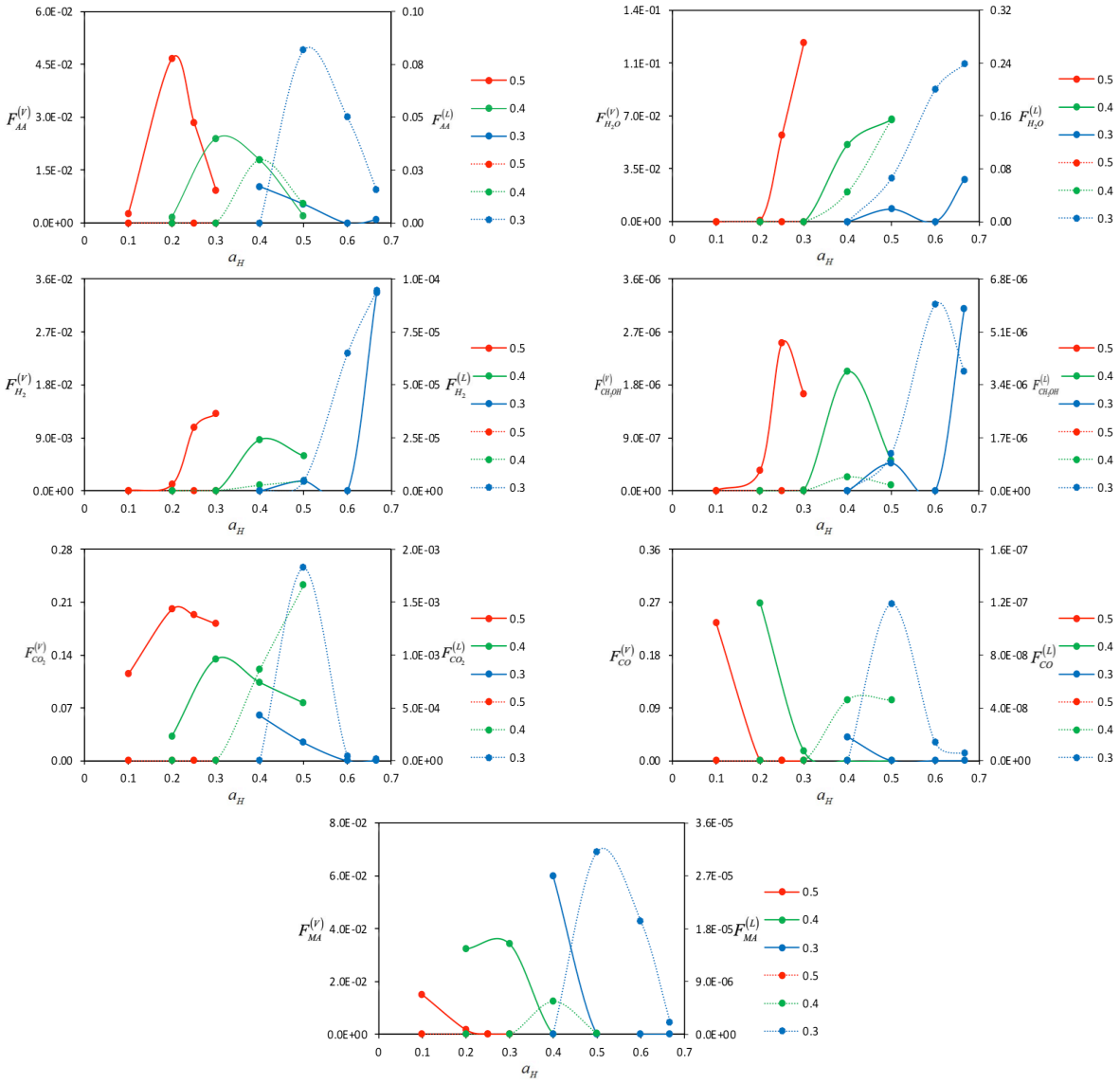

Figure 3.5: $F_j^{(V)}$(solid, left), $F_j^{(L)}$(dash, right) iso- a_O lines as a_H functions, T=150°C, P=10 bar

Figure 3.6 shows the equilibrium composition of the products as the pressure is increased from 10 bar to 30 bar at a constant temperature of 150°C. In liquid phase, increasing the pressure had a more pronounced effect on CO_2 production in which maximum production increases from $F_{CO_2}^{(L)} = 0.002$ to $F_{CO_2}^{(L)} = 0.012$. On the other hand, acetic acid production increases slightly reaching the maximum of $F_{AA}^{(L)} = 0.086$, and forms at $a_O \leq 0.5$. A similar trend is observed with

water, where it forms at $a_O \leq 0.5$, and water production increases linearly with increasing a_H reaching maximum of $F_{H_2O}^{(L)} = 0.261$. In the vapor phase, maximum methyl acetate production dramatically decreases reaching maximum of $F_{MA}^{(V)} = 0.06$ compared to $F_{MA}^{(V)} = 0.033$ at 150°C and 10 bar, whereas CO production remains the same at the maximum of $F_{CO}^{(V)} = 0.267$.

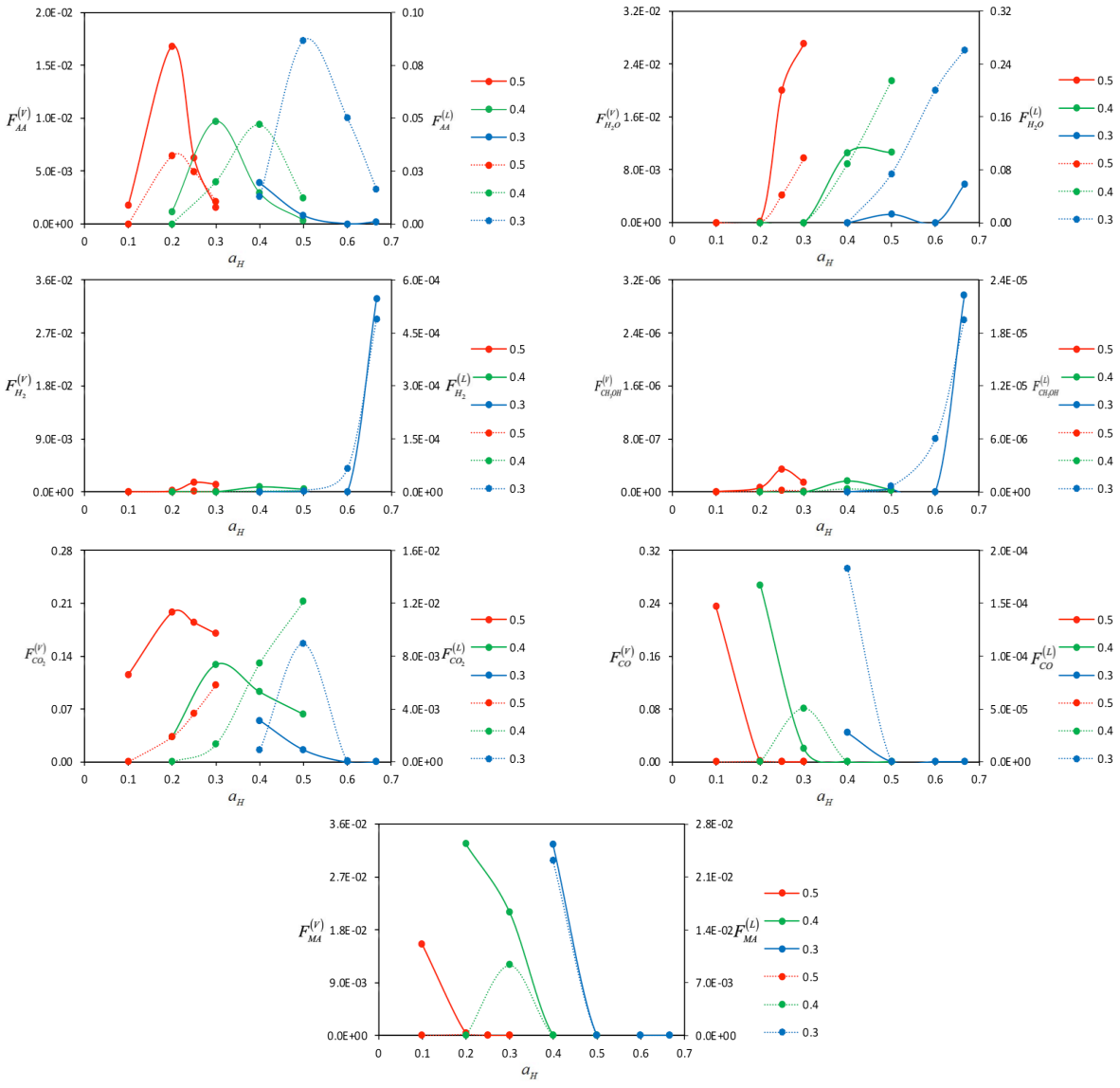

Figure 3.6: $F_j^{(V)}$(solid, left), $F_j^{(L)}$(dash, right) iso- a_O lines as a_H functions, T=150°C, P=30 bar

As the pressure increases to 50 bars and at $(a_O, a_H) = (0.3, 0.5)$, 95% of the total products occur in the liquid phase in which acetic acid, $F_{AA}^{(L)} = 0.087$, and water, $F_{H_2O}^{(L)} = 0.075$, count for ~ 41% and ~ 49 %, respectively. In the vapor phase, CO_2, $F_{CO_2}^{(V)} = 0.008$, counts for over 90% of the products as shown in **Figure 3.7**. Consequently, $\left(a_H, a_O, T, P\right)$ =(0.3, 0.5, 150°C, 50 bar) is a promising operating point for maximum acetic acid production where minimum separation process is required.

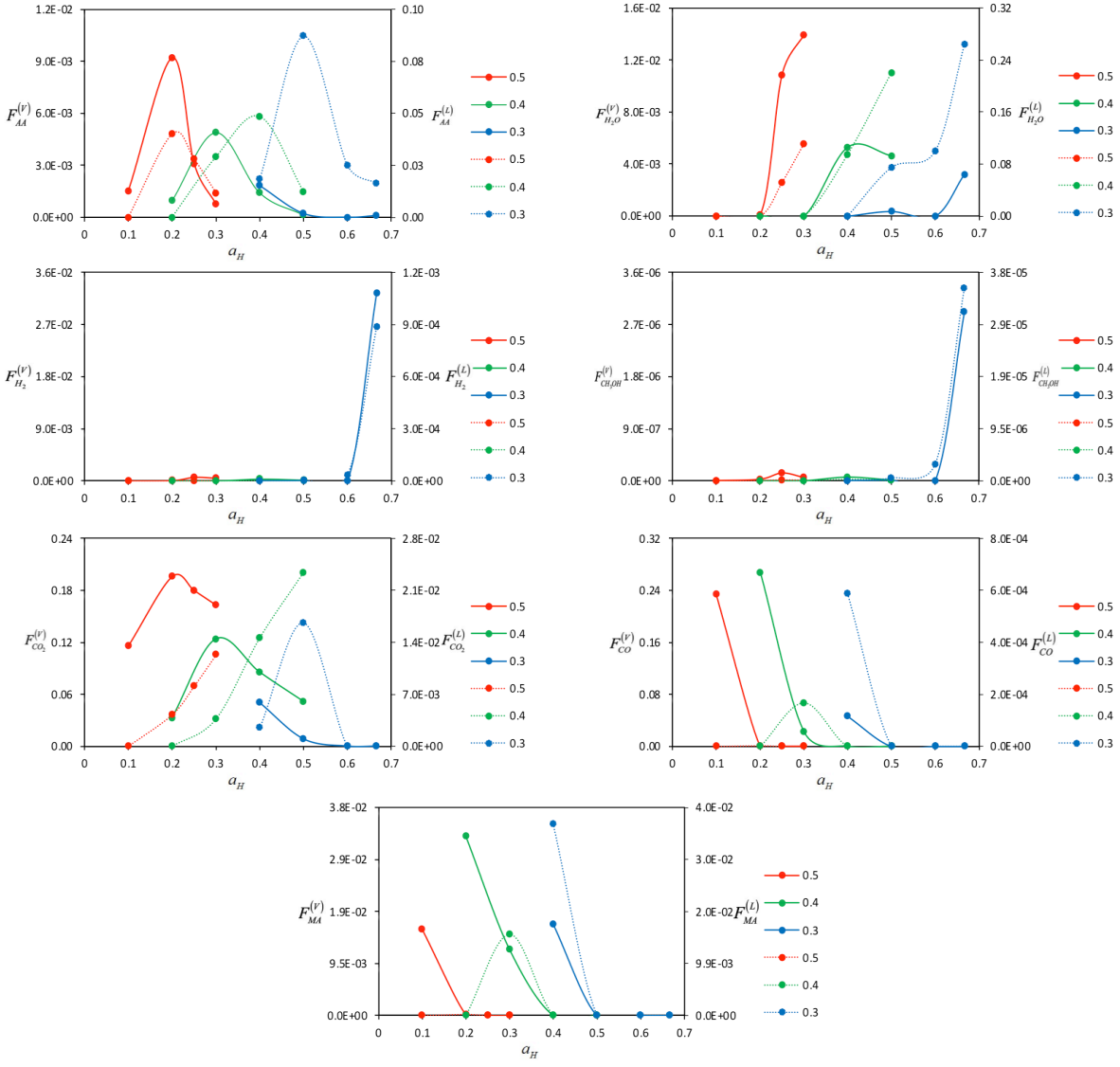

Figure 3.7: $F_j^{(V)}$(solid, left), $F_j^{(L)}$(dash, right) iso- a_O lines as a_H functions, T=150°C, P=50 bar

Figure 3.8 shows that only vapor phase exists when temperature is increased from 150°C to 200°C at constant pressure of 10 bar. At this temperature, the maximum acetic acid production of $F_{AA}^{(V)} = 0.071$ occurs at $(a_O, a_H) = (0.3, 0.5)$ compared to $(a_O, a_H) = (0.5, 0.2)$ at 150 °C and 10 bar; this only counts for 31% of the total products. As for water, its production increases as a function of a_H and deceases as a function of a_O and reaches maximum yield of $F_{H_2O}^{(V)} = 0.237$ at $(a_O, a_H) = (0.3, 0.667)$. The production of CO, methyl acetate, and CO_2 remains almost the same, whereas H_2 production doubles reaching maximum of $F_{H_2}^{(V)} = 0.101$.

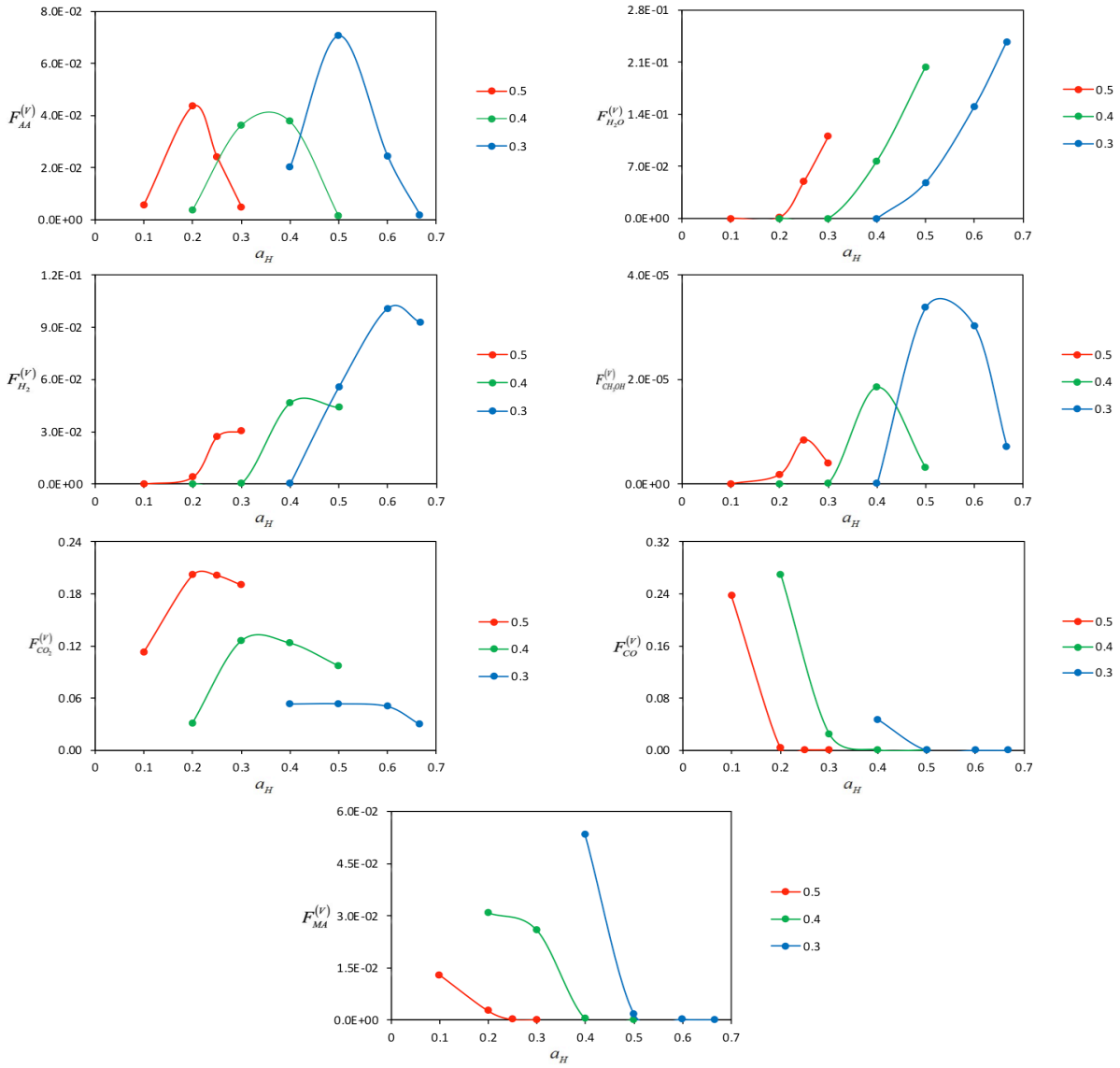

Figure 3.8: $F_j^{(V)}$(solid, left) iso- a_O lines as a_H functions, T=200°C, P=10 bar

More liquid forms particularly at $a_O \in \{0.3, 0.4\}$, when the pressure is increased to 30 bar as shown in **Figure 3.9**. In liquid phase, acetic acid production only occurs at $a_O \leq 0.4$, reaching maximum of $F_{AA}^{(L)} = 0.081$ at $(a_O, a_H) = (0.3, 0.5)$ where acetic acid yield surpasses water yield, $\frac{F_{AA}^{(L)}}{F_{H_2O}^{(L)}} = 1.25$. The maximum water production is achieved at the same a_O, but at a higher a_H,

$a_H = 0.667$, with $F_{H_2O}^{(L)} = 0.232$. In the vapor phase, CO_2 makes the majority of the products and its maximum of $F_{CO_2}^{(V)} = 0.201$ occurs at $(a_O, a_H) = (0.5, 0.2)$, whereas the production of the other species, namely CO, methyl acetate, and CH_3OH, remain the same.

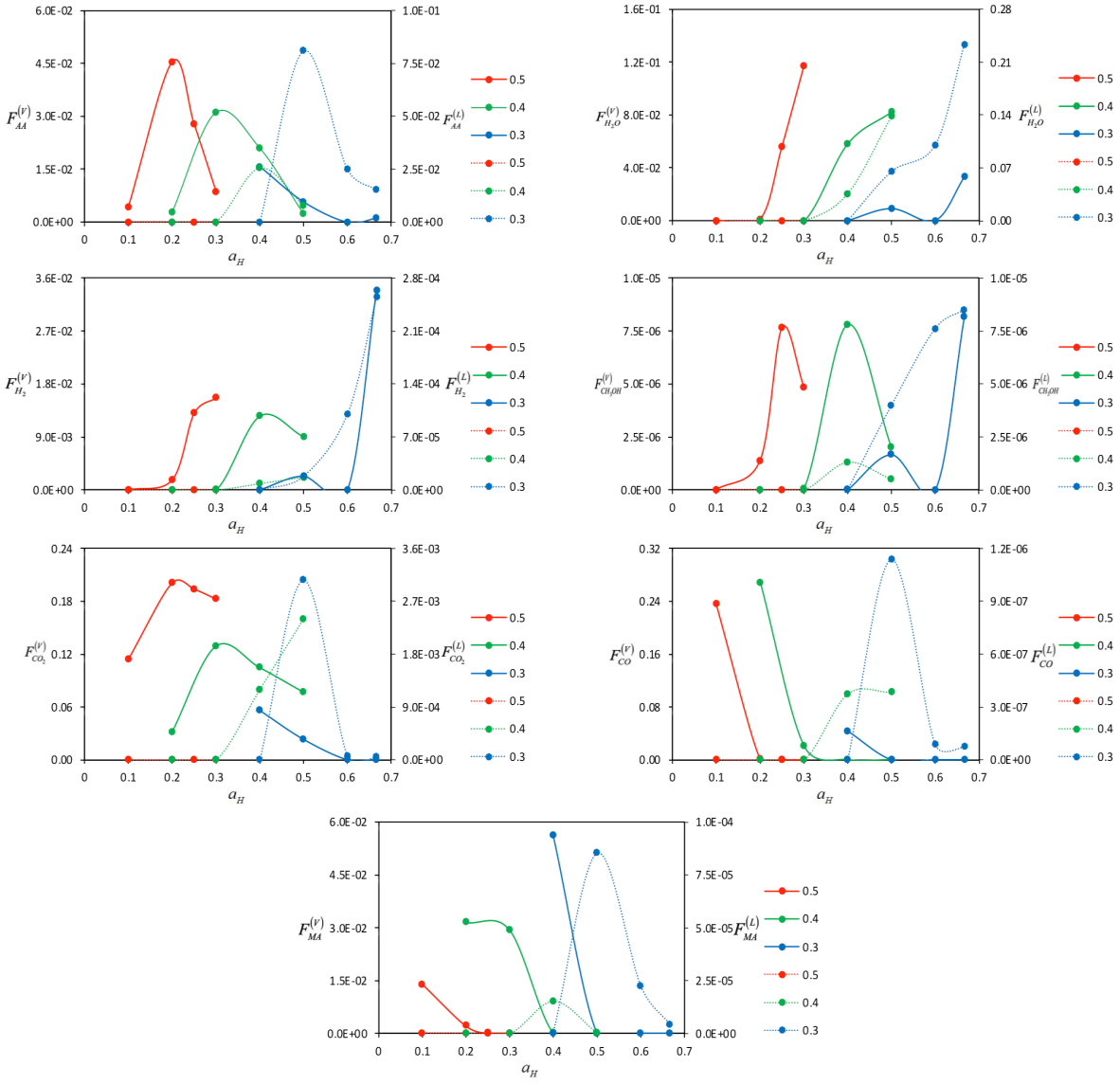

Figure 3.9: $F_j^{(V)}$(solid, left), $F_j^{(L)}$(dash, right) iso- a_O lines as a_H functions, T=200°C, P=30 bar

A further increase of the pressure to 50 bar results in more liquid products with maximum production of acetic acid at $F_{AA}^{(L)} = 0.085$. The maximum production of water with $F_{H_2O}^{(L)} = 0.072$ occurs at $(a_O, a_H) = (0.3, 0.5)$, shown in **Figure 3.10**. At this point, acetic acid count for ~52% of liquid products and over 85% of carbon is utilized for acetic acid production. In the vapor phase and at $(a_O, a_H) = (0.3, 0.5)$, CO_2 counts for ~75% of the products with maximum production of $F_{CO_2}^{(V)} = 0.017$, which makes this operating point another promising point that results in maximum acetic acid production.

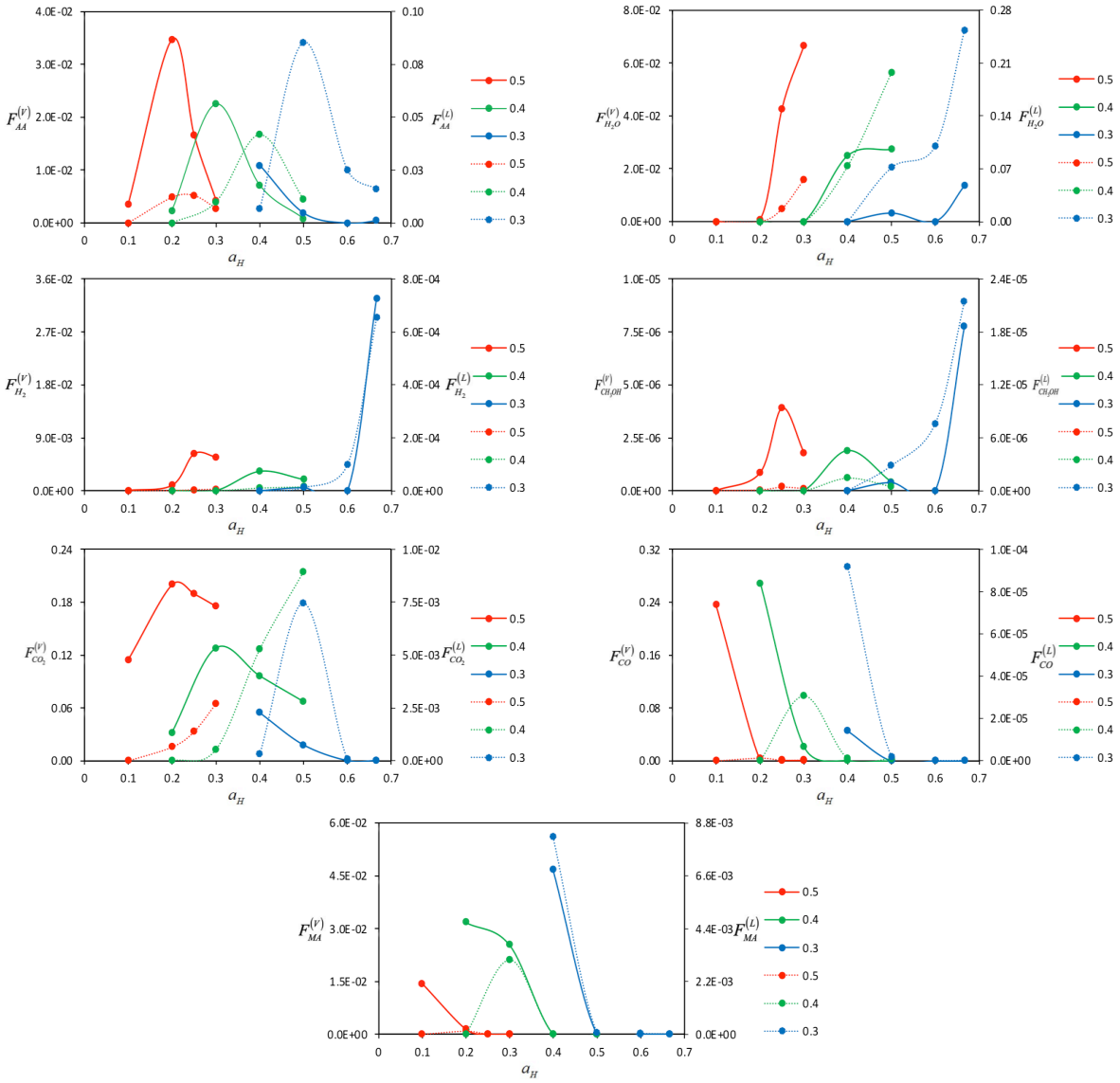

Figure 3.10: $F_j^{(V)}$(solid, left), $F_j^{(L)}$(dash, right) iso- a_O lines as a_H functions, T=200°C, P=50 bar

Increasing the temperature to 250°C at 10 bar is detrimental for acetic acid as its maximum production decreases to $F_{AA}^{(V)} = 0.059$ as shown in **Figure 3.11**. Nonetheless, acetic acid production decreases at a slower rate compared to water which results in increasing the ratio of acetic acid to water, $\frac{F_{AA}^{(V)}}{F_{H_2O}^{(V)}} = 1.91$. At the same (a_O, a_H) points, CO_2 production increases where

it surpasses acetic acid, $\frac{F_{AA}^{(V)}}{F_{CO_2}^{(V)}} = 0.82$, and CO_2 maximum production occurs at a slightly higher a_H, $a_H = 0.25$, compared to $a_H = 0.20$ at 200°C. As for other species, CO and H_2 production slightly increase, whereas a slight decrease is observed for methyl acetate.

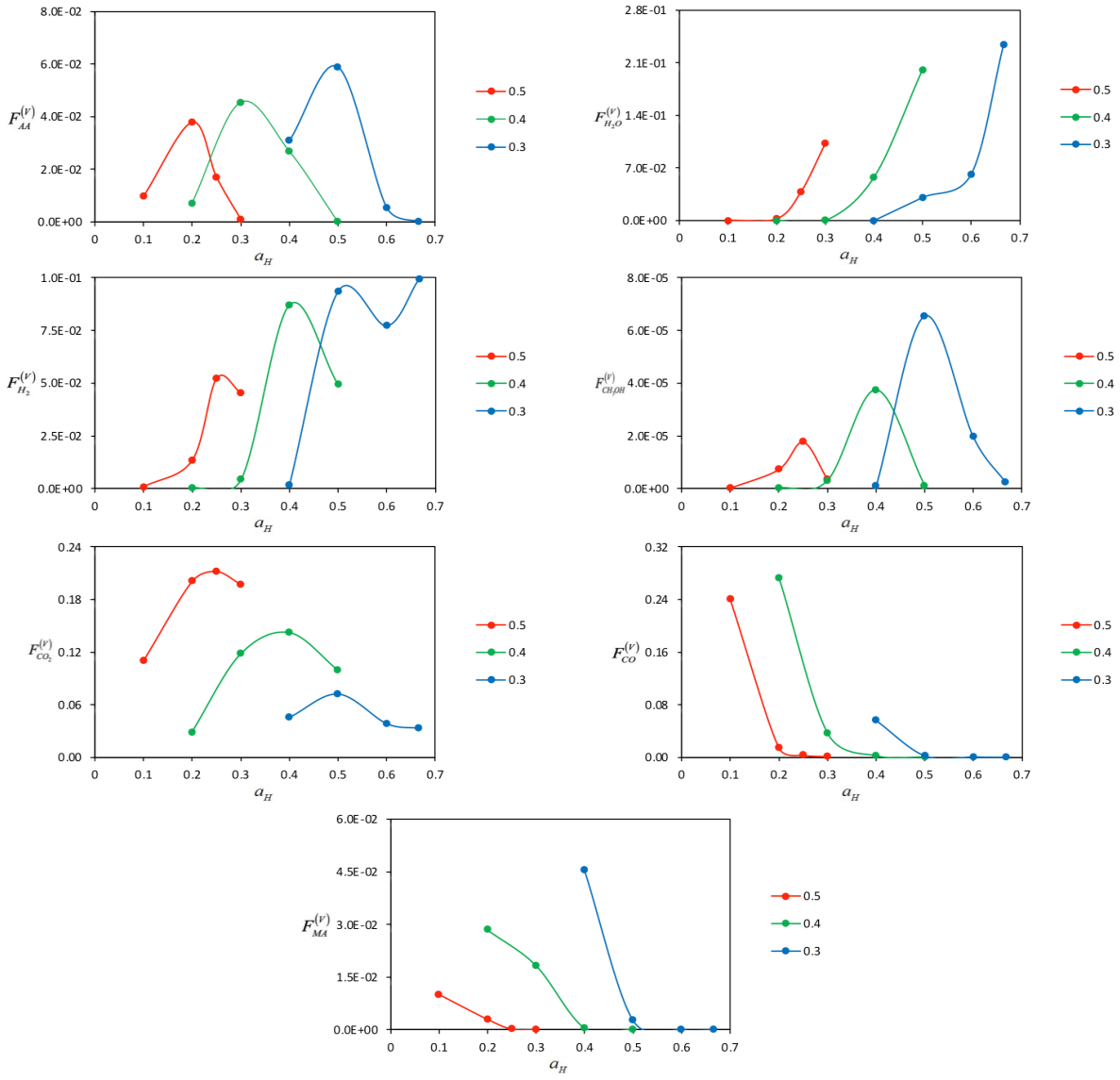

Figure 3.11: $F_j^{(V)}$(solid, left) iso- a_O lines as a_H functions, T=250°C, P=10 bar

Figure 3.12 shows that acetic acid production in vapor phase increases with increasing the pressure to 30 bar reaching maximum of $F_{AA}^{(V)} = 0.069$; however, water production increases at a higher rate for the same points of $(a_O, a_H) = (0.3, 0.5)$, reaching maximum of $F_{H_2O}^{(V)} = 0.049$. Further increase of pressure to 50 bar results in a lower acetic acid yield where its maximum yield occurs at a higher a_O, $a_O = 0.5$.

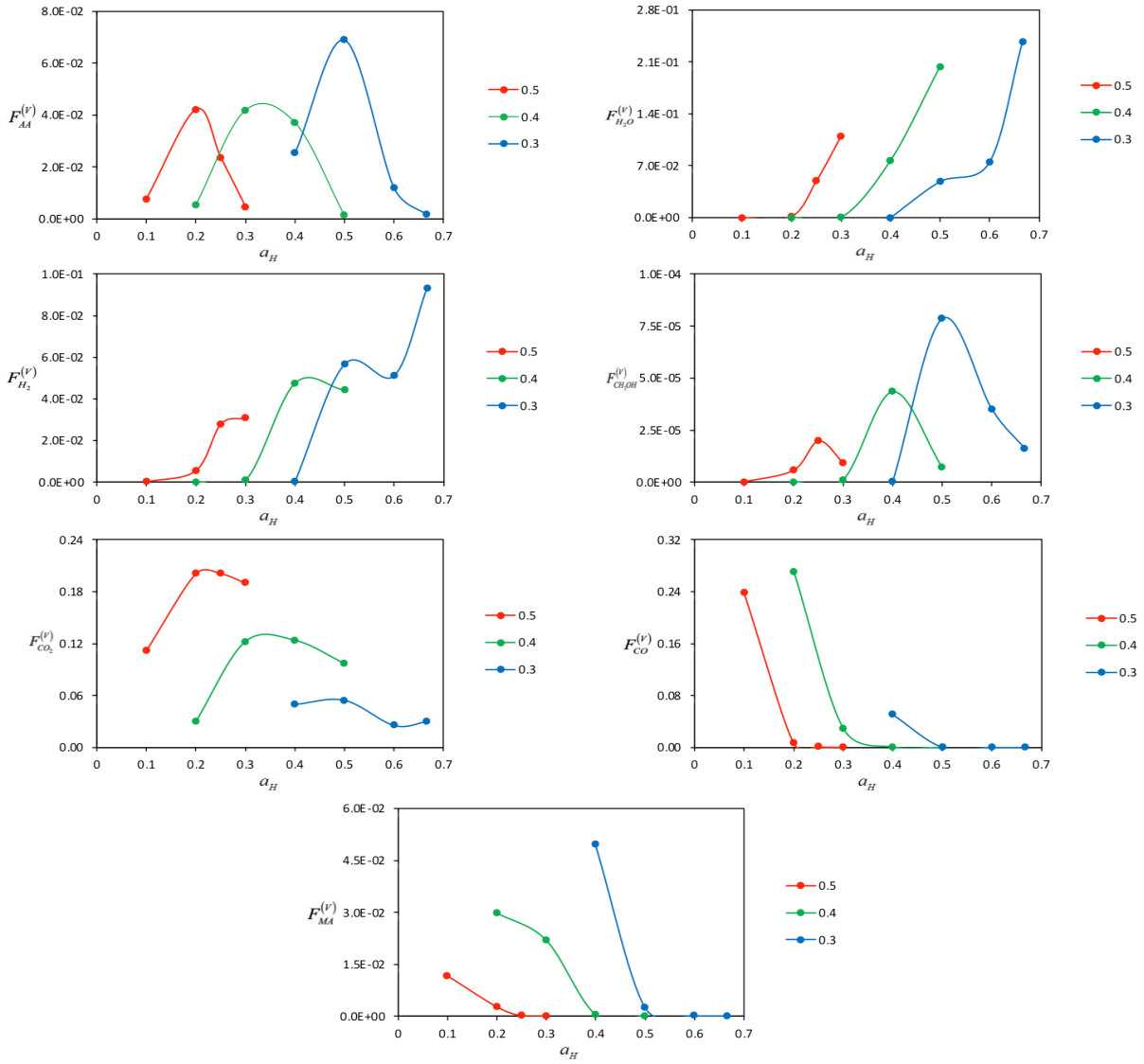

Figure 3.12: $F_j^{(V)}$(solid, left) iso- a_O lines as a_H functions, T=250°C, P=30 bar

The above equilibrium analysis indicates that low a_O is preferred for acetic acid production; thus, we investigated the equilibrium behavior at a lower a_O, in particular at $\left(a_H, a_O\right)$= (0.55, 0.25), which exists at the edge of the attainable region of the five species considered for the feed. The result of the investigated point shows that the maximum production of acetic acid with $F_{AA}^{(L)} = 0.124$ occurs at T=100°C and P=50 bar, where acetic acid makes 98.8% of the total products and ~99% of carbon fed to the system are contained in acetic acid. At this operating point, a negligible amount of CO_2 and water are produced with $F_{CO_2}^{(L)} = F_{H_2O}^{(L)} = 3.88\text{E}-04$. A more practical operating point occurs at a higher temperature of 200°C and pressure of 50 bar as it is in the range of the commercial operating conditions. At this condition, acetic acid production reaches maximum of $F_{AA}^{(L)} = 0.120$ which makes 95.5% of total products and consumes ~96% of the carbon fed to the system. Also, little CO_2 and water are produced with maximum production of $F_{CO_2}^{(L)} = F_{CO_2H_2O}^{(L)} = 1.36\text{E}-03$.

3.5 Conclusions

A general conceptual frame based on Gibbs free energy minimization was utilized to study the phase equilibrium of a system containing seven species: CO, CO_2, H_2, CH_3OH, H_2O, CH_3COOH, and $C_3H_6O_2$. The equilibrium analysis was carried out to determine promising operating points $\left(a_H, a_O, T, P\right)$ space which resulted in maximum acetic acid production. To reduce the number of variables involved in the equilibrium analysis, the analysis was performed in atom mole fraction space $\left(a_H, a_O, a_C\right)$, by varying the inlet hydrogen and oxygen atom-mol fractions $\left(a_H, a_O\right)$ atoms for different range of temperatures and pressures,

$T\left(^{o}C\right)\in\left\{100,150,200,250\right\}$ and $P\left(bar\right)\in\left\{10,30,50\right\}$. The following operating points are promising points for maximum acetic acid production, which require minimum product separation:

1. $\left(a_H, a_O, T, P\right)$ = (0.5, 0.3, 150 °C, 50 bar), which features maximum production of acetic acid, water, and CO_2 at $F_{AA}^{(L)}=0.087$, $F_{H_2O}^{(L)}=0.075$, and $F_{CO_2}^{(V)}=0.008$, respectively.
2. $\left(a_H, a_O, T, P\right)$ = (0.5, 0.3, 200 °C, 50 bar), which features maximum production of acetic acid, water, and CO_2 at $F_{AA}^{(L)}=0.085$, $F_{H_2O}^{(L)}=0.072$, and $F_{CO_2}^{(V)}=0.017$, respectively.
3. $\left(a_H, a_O, T, P\right)$ = (0.55, 0.25, 100 °C, 50 bar), which features maximum production of acetic acid, water, and CO_2 at $F_{AA}^{(L)}=0.124$, and $F_{H_2O}^{(L)}=F_{CO_2}^{(L)}=3.88\text{E}-04$, respectively.
4. $\left(a_H, a_O, T, P\right)$ = (0.55, 0.25, 200 °C, 50 bar), which features maximum production of acetic acid, water, and CO_2 at $F_{AA}^{(L)}=0.120$ and $F_{H_2O}^{(L)}=F_{CO_2}^{(L)}=1.36\text{E}-03$, respectively.

The fourth operating condition is the most practical from industrial perspective as the current commercial processes are operating in a similar range.

CHAPTER 4: Design of Dilute Palladium-Indium Alloys for The Selective Hydrogenation of CO_2 to Methanol

4.1 Introduction

Carbon dioxide (CO_2) is a major air pollutant and a potent greenhouse gas emitted from a wide range of human activities including transportation, electricity generation, and industry. In the past few decades, a dramatic increase in the CO_2 concentration in the earth's atmosphere (up to >400 parts per million (ppm)) has led to concerns about global climate changes with possibly irreversible environmental ramifications [121]. Catalytic conversion of CO_2 into value-added chemicals is an attractive route for mitigation [122] as it provides a clear economic incentive for harvesting CO_2 rather than emitting it. The conversion of CO_2 to methanol has been at the nexus of these utilization efforts due to the high reactivity of methanol and the fact that it already serves as a key building block in the chemical industry for the production of acetic acid [98,117], formaldehyde [123] , and dimethyl ether [124], prompting calls for the establishment of a "methanol economy [125]".

Although methanol is commercially synthesized from syngas ($CO/CO_2/H_2$ mixtures) using a $Cu/ZnO/Al_2O_3$ catalyst [126], this material has a low tolerance for high CO_2 concentrations [127]. In the quest for a novel catalyst for methanol synthesis from CO_2, indium oxide (In_2O_3), has emerged as a promising catalyst as predict by density functional theory (DFT) calculations [41,42]. Subsequent tests of ZrO_2-supported In_2O_3 displayed 100% methanol selectivity and stability for over 1000 hours at relevant industrial conditions (T=573 K, P = 5.0 MPa, H_2/CO_2 = 4, and GHSV = 16,000 h^{-1}) [44]. Nonetheless, indium inherently has a limited hydrogen splitting ability; hence, a second promoting metal such as, palladium (Pd) [48,128] or platinum (Pt) [50,129] is required to enhance the material's catalytic activity toward CO_2 conversion.

Due to the scarcity and high costs of these noble metal promoters, it is of economic importance to expose as much of the noble metals to the reactant stream as possible while maintaining their catalytically active configurations under reaction conditions. This has been achieved at the extreme limit with the promoter fully dispersed either on a support (single-atom catalyst) [130,131] or within another host metal (single-atom alloy) [132,133]. In some cases, however, isolated atoms are inactive for the desired transformation (e.g., the cleavage of C-C and C-H bonds in propane/propene oxidation [134]). In such cases nanoclusters of the noble metals may instead be required.

Recently Peŕez-Ramiŕez and co-workers highlighted the importance of forming small ensembles of Pd (2-3 atoms) on In_2O_3 to promote the rate, selectivity, and stability of methanol synthesis from CO_2 [48]. While the addition of isolated Pd atoms increased the reaction rate and selectivity to methanol, ensembles in the 2-3 atoms range were more effective due to their improved H_2 dissociation capabilities. Synthesis of these ensembles required the use of low Pd loadings to ensure that Pd was primarily anchored to the In_2O_3 rather than to other Pd atoms. Larger clusters (>4) behaved more like Pd and promoted the parasitic reverse water-gas shift (RWGS) reaction which converts CO_2 undesirably to CO instead of methanol. Pérez-Ramírez and co-workers also noted that the choice of synthesis method was important, with coprecipitation generally producing more uniform and stable catalytic materials than dry impregnation. Tunability of this system is somewhat limited, however, as the support identity is critical and thus cannot be varied, while the selectivity and stability are highly sensitive to Pd loading.

Herein we investigate the promotional effects of dilute Pd in metal-in-metal Pd-In alloys rather than in metal-on-metal oxide Pd/In_2O_3 in order to decouple the active phase from the

support and expand opportunities for selective CO_2 hydrogenation. We demonstrate a new synthesis approach for In-based CO_2 hydrogenation catalysts whereby the galvanic replacement (GR) method is used to controllably exchange Pd into In nanoparticles anchored to a conventional metal oxide support (γ-Al_2O_3) which only serves to disperse the In. Prior studies have shown this method to be effective in synthesizing dilute alloys with controllable composition while mitigating deposition of the promoter metal onto the support [135–139], but this has not yet been demonstrated with In systems to our knowledge. We hypothesized that this colocation of Pd and In is likely to be important here for selectivity control since it has been previously shown that alloying with In greatly reduces the catalytic activity of Pd for CO formation in methanol steam reforming [140]. Here the structural and catalytic natures of Pd in GR-synthesized Pd-In alloys were interrogated to reveal that distinct Pd structures can be produced by varying the alloy composition and exploited to obtain favorable catalytic performance. The Pd-In alloy catalysts showed unique reactivities with the alloy containing small aggregates of Pd demonstrating a substantial improvement in methanol production rate and selectivity relative to isolated Pd atoms.

4.2 Experimental

4.2.1 Catalyst Preparation

In_2O_3 supported on gamma alumina, γ-Al_2O_3, (Inframat, 99.995%) was synthesized via incipient wetness impregnation (IWI) where a desired amount of indium (III) nitrate hydrate, $In(NO_3)_3 \cdot xH_2O$ (Aldrich, 99.9%), was dissolved in deionized water and then impregnated on γ-Al_2O_3 (~1.08 mL $g_{\gamma\text{-}Al2O3}^{-1}$). The as-synthesized catalyst was then thermally treated in air at 300°C (5°C min^{-1} ramp) for 3 h and then reduced at 350°C (10°C min^{-1} ramp) under 5% H_2 in Ar (20 mL min^{-1}) for 2 h. Separately, 150 mL of DI-water was brought to a boil in an argon

environment. Sodium borohydride, $NaBH_4$ (Aldrich, 99%), was added dropwise to the water to reach a concentration of 0.1M and stirred for 15 minutes. The reduced In_2O_3 was added to the boiled DI water without exposure to air. To further prevent the oxidation of the supported In_2O_3, 0.1M ascorbic acid (Aldrich, 99%) was added to the solution after 15 minutes of stirring. The subsequent addition of Pd atoms exclusively to In nanoparticles was then achieved via galvanic replacement (ΔE^o=1.28 V) where the Pd precursor is favorably reduced by In, host metal, according to the following two half-reactions:

$$Pd^{2+} + 2e \rightarrow Pd^0 \qquad \Delta E^o = 0.951\,V$$

$$In^0 \rightarrow In^{3+} + 3e \qquad \Delta E^o = 0.338\,V$$

To achieve this a desired amount of palladium (II) nitrate hydrate, $Pd(NO_3)_2 \cdot xH_2O$, (Aldrich) was dissolved in DI H_2O and then added to the solution while stirring. The resulting material was filtered and washed with 1 L of DI H_2O. The acquired powder was then dried overnight under vacuum at 120°C.

4.2.2 Catalyst Characterization

Inductively coupled plasma atomic emission spectroscopy (ICP-AES) measurements were conducted on a Leeman Labs PS1000 instrument. The catalyst samples were digested in 2 mL of an aqua regia solution overnight and then further diluted in DI-H_2O to obtain a desired concentration (typically 1-100 ppm) of the metal at a neutral pH. X-ray diffraction (XRD) was performed on a Rigaku instrument. Cu Kα radiation was used with a power setting of 30 mA and 15 kV. Data was collected for 2θ between 10° and 70° with a step size of 0.01° and a scan speed of 0.15° min^{-1}. X-ray photoelectron (XPS) spectra were obtained on a Kratos Axis Ultra DLD system equipped with a monochromatic Al Kα X-ray source and a double focusing hemispherical analyzer. For all samples, 40 scans were collected for the Pd 3d region and 20 scans for the In 3d region, and the XPS data were analyzed using the Thermo Avantage software.

The reduced fresh catalysts were exposed to air for ~1-2 min during sample loading. Scanning transmission electron microscopy imaging and energy dispersive X-ray spectroscopy (STEM-EDS) as well as high resolution transmission electron microscopy (HRTEM) were performed using a Titan ST microscope (FEI company) operated at an accelerating voltage of 300 kV equipped with field emission electron gun and a 4k×4k CCD camera. The HR-TEM beam focus was 100 nm while that of STEM was 1.0 nm. Energy Dispersive X-ray (EDS) analyses were performed on catalysts with exposed areas smaller than or equal to the image size to facilitate the microscopic analysis when EDS was conducted in the TEM mode of operation. For each sample, approximately 50 EDS spectra were collected.

Diffuse reflectance infrared Fourier transform spectroscopy (DRIFTS) measurements were performed on a Thermo Scientific Nicolet iS50 FTIR spectrometer equipped with a DTGS KBr detector and a Harrick Praying Mantis high temperature reaction cell (HVC-DRP4) equipped with ZnSe and quartz windows. In a typical experiment, the catalyst sample was purged with He while heating to 300°C, after which the gas mixture was switched to 10% H_2 in He at a flow rate of 12 mL min^{-1} for 1 h. After reduction the sample was purged with He gas at 300°C for 10 min and subsequently cooled to room temperature under He with flow of 12 mL min^{-1}, after which a background spectrum was recorded. Thereafter a 3% CO in He gas mixture was introduced into the cell for 30 min at a flowrate of 12 mL min^{-1} during which spectra were collected every 2-5 min. While continuing to collect spectra, the sample cell was then purged with He at a flow rate of 12 mL min^{-1} for a minimum of 30 min. Each CO-DRIFTS spectrum was recorded at 25°C with a spectral resolution of 4 cm^{-1} and as an average of 96 scans.

X-ray Absorption Spectroscopy (XAS) measurements were carried out in the 8-ID beamline at the National Synchrotron Light Source II of Brookhaven National Laboratory. The

in situ Pd K-edge (24359 eV) XANES spectra were collected using the fluorescence mode during the CO_2 hydrogenation reaction in a Clausen cell flow reactor under atmospheric pressure. The catalyst (~2 mg) was loaded in a quartz tube (1.0 mm OD and 0.9 mm ID), and a gas mixture of 2 mL/min CO_2 and 6 mL/ min H_2 was introduced to the system. The sample was heated from room temperature to the desired temperatures with a 10°C/min ramping rate. The *ex-situ* EXAFS spectra were collected in the same beamline with samples mounted via Kapton tape. The energy calibration was performed based on the Pd K-edge energy (24.359 keV) of a palladium foil standard. Data processing was performed using the IFEFFIT package. Depending on the Pd loading, fifteen to thirty-five spectra were averaged. The average spectra were fit using WinXAS software. Phase and amplitude functions were prepared from experimental references, e.g., Pd foil (12 Pd-Pd at 2.75 Å and PdO (4 Pd-O at 2.05 Å). Fitting was initial performed on k^2-weighted chi in R space from $\Delta k = 2.8 – 11.4$ Å^{-1} and $\Delta R = 1.0\text{-}2.0$ Å for PdO or $\Delta R = 1.3\text{-}2.9$ Å for used and reduced samples. Optimized fits were determined in k-space on k^2-weighted chi of the isolated Pd-O or Pd-M (M=Pd or In) shells to determine the best $\Delta\sigma^2$ values. The $\Delta\sigma^2$ values of each sample were similar; therefore, the average value of all samples was taken and fixed in the final fits.

4.2.3 Catalyst Testing

The catalytic performance of the Pd-In catalysts for CO_2 hydrogenation to methanol was evaluated in a fixed bed reactor at a pressure of 30 bar, temperatures of 240-300°C, and gas-hourly space velocity (GHSV) of 9000 h^{-1}. The reactor was loaded with 0.4 mL of catalyst with particle size of 125 and 250 μm between two beds of quarts wool. The catalyst was reduced prior to reaction under 20% H_2 in Ar at 300°C (10°C min^{-1} ramp) and atmospheric pressure for 1 h. After reduction, a premixed feed of H_2 and CO_2 (3:1 molar ratio), was introduced to the reactor

via a mass flow controller at 30 bar. Once the reaction reached steady state after 90 min, the product mixture was analyzed online by two gas chromatographs: one equipped with a thermal conductivity detector (TCD) to analyze CO, CO_2 and H_2, and one equipped with a flame ionization detector (FID) to analyze methanol, methane, and dimethyl ether. All products lines were heated above 100°C to prevent product condensation.

4.3 Results and discussion

4.3.1 Structural and compositional characterization of Pd-In alloys

Three different alloys of Pd-In/γ-Al_2O_3 catalysts were prepared by employing the galvanic replacement (GR) method, in which a controlled amount of Pd was exchanged with pre-reduced In supported on γ-Al_2O_3. The Pd concentration was varied to achieve distinct Pd surface structures and the nominal loadings of palladium and indium were closely matched as confirmed by inductively coupled plasma atomic emission spectroscopy (ICP-AES) (**Table 4.1**).

Table 4.1: Indium and palladium compositions as measured by ICP-AES

Catalyst	In nominal loading (wt%)	In measured loading (wt%)	Pd nominal loading (wt%)	Pd measured loading (wt%)
Pd_1In_5	9.0	8.2	1.8	1.62
Pd_1In_{50}	9.0	8.5	0.18	0.14
Pd_1In_{100}	9.0	8.7	0.09	0.08

High angle annular dark-field scanning transmission electron microscopy (HAADF-STEM) images and elemental mapping by energy dispersive X-ray spectroscopy (EDS) revealed that that palladium was deposited on indium rather than γ-Al_2O_3 support and formed Pd-In alloys (**Figure 4.1**). In some cases, indium alone was detected (e.g., Pd_1In_{100}) due to the low palladium contents in the materials and the possibility of palladium being predominantly isolated (i.e., single atom alloy), which can be challenging to discern from the host metal. Representative spectra (~50 were collected for each sample) are shown for each catalyst in **Figure 4.1**.

Furthermore, the calculated d-spacing value of 0.229 nm is similar to reported value in the literature (**Figure A5),** which further support alloy formation [128]. The average particle sizes of different fresh (prior to reaction) Pd-In alloys were estimated by STEM to be 2.5±1.6 nm for Pd_1In_5 and 1.8±0.5 nm for Pd_1In_{50}. A larger average particle sizes were observed after reaction with Pd_1In_5 increasing to 3.9±1.5, and Pd_1In_{50} increasing to 2.3±0.5 nm.

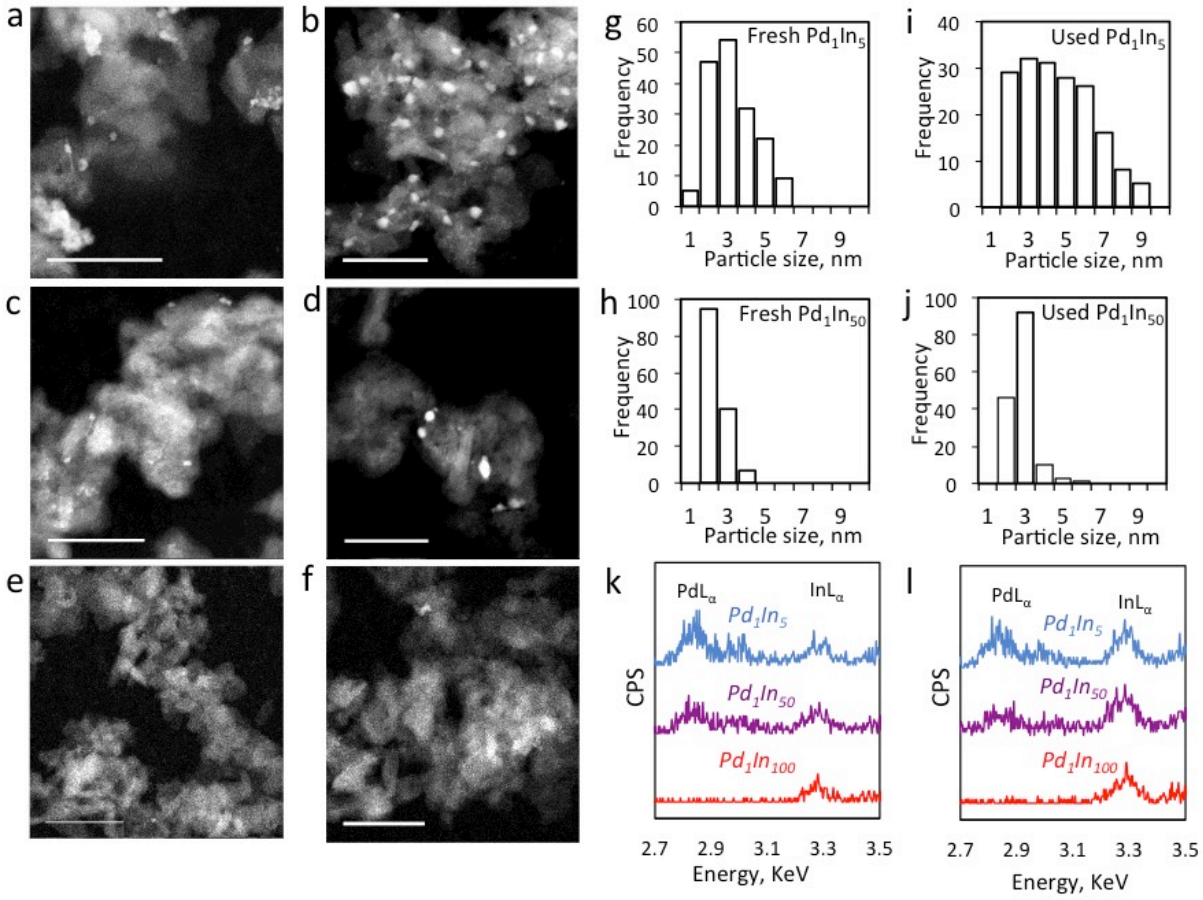

Figure 4.1: HAADF-STEM images of Pd-In alloys, their average particle size distributions and their STEM EDS. (a) Fresh Pd_1In_5 catalyst. **(c)** Fresh Pd_1In_{50} catalyst. **(e)** Fresh Pd_1In_{100} catalyst **(b)** Used Pd_1In_5 catalyst. **(d)** Used Pd_1In_{50} catalyst. **(f)** Used Pd_1In_{100} catalyst. **(g to j)** Average particle distribution for Pd-In alloys. **(k)** STEM-EDS spectra of fresh Pd-In alloys. **(l)** STEM-EDS spectra of used Pd-In alloys. The scale bar in all images is 50 nm

To identify the crystalline phases present in the samples, powder X-ray diffraction (XRD) was obtained for the fresh and spent catalysts (**Figure 4.2**). Substantial overlap between γ-Al_2O_3

reflections (from the support) with those from the anticipated Pd/Pd-In phases and segregated In_2O_3 particles makes conclusive determinations difficult to make [48,141]. This is especially true given that γ-Al_2O_3 contributes a signal near 2θ=40° where the most intense reflections of Pd and several Pd-In phases manifest. However, the spent Pd_1In_5 catalyst shows a clear intensity increase in this region without any other changes However, a clear increase in the signal near 40° 2θ in the Pd_1In_5 catalyst after reaction without any other clear changes is more consistent with the presence of a PdIn alloy than pure Pd. Additionally decreases in features at 21.7°, 35.6°, 51.2°, and 60.8° corresponding to In_2O_3 and In phases suggest that a larger fraction of the In is alloyed as the Pd content increases (**Figure A6)**, a notion supported by the other techniques utilized here.

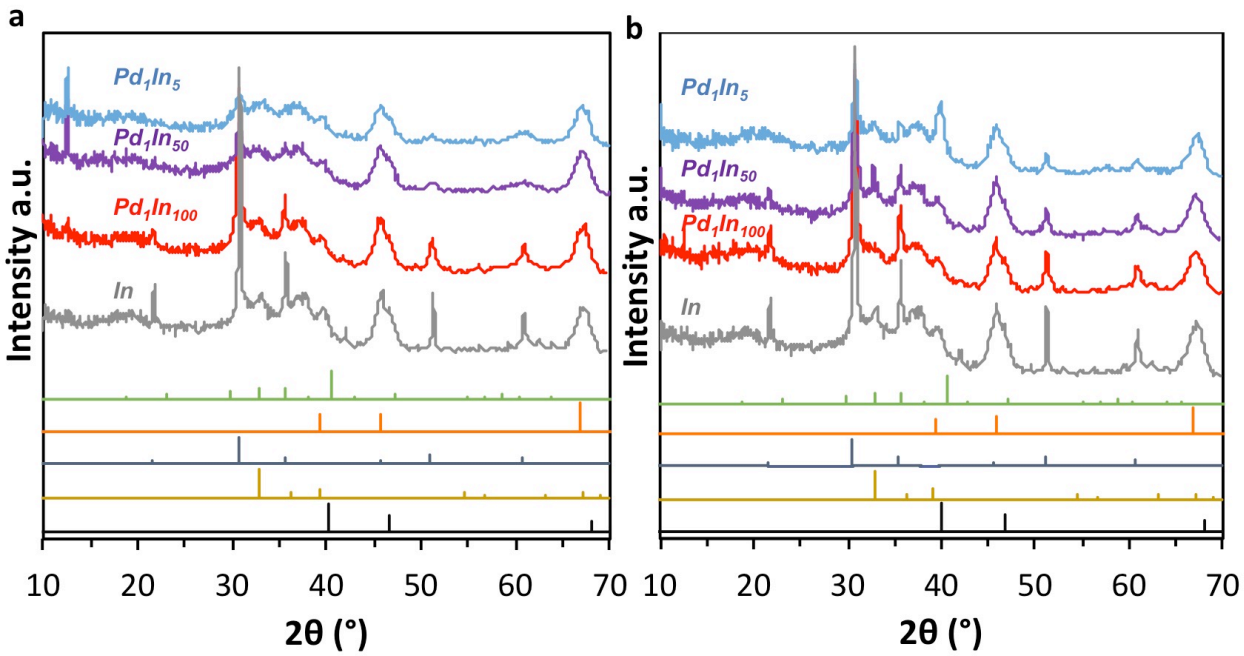

Figure 4.2: XRD diffractograms of the investigated catalysts. (a) Fresh catalysts. (b) Used catalysts. Reference diffractograms of Pd (black) , PdIn (green), γ-Al_2O_3 (orange),In (yellow) and In_2O_3 (blue) (JCPDS 00-046-1043, 01-073-8988, 00-010-0425,00-005-0642, and 00-006-0416 respectively).

X-ray photoelectron spectroscopy (XPS) was used to assess the Pd:In ratios of the reduced fresh and spent catalysts (**Table 4.2**, **Figure A7**, **Figure A8**). Both surface and bulk

atoms contribute substantially to the XPS data since the electron mean free path (~1.5 nm) is comparable to the average particle radii (~1-2 nm). Acknowledging that the technique is nonetheless biased toward the former, the tabulated data suggest that Pd_1In_{50} retains a substantially larger fraction of surface Pd after reaction than does Pd_1In_5 (94 *vs* 58%). Since the GR synthesis places Pd on the surface initially, migration of Pd into the bulk during reaction is a plausible explanation. Pd_1In_{50} may therefore be more effective in exposing the Pd promoter to the reactant stream than Pd_1In_5.

Table 4.2: Indium and palladium corrected peak area as measured by XPS

Catalyst	In corrected peak area	Pd corrected peak area	In:Pd ratio
Pd_1In_5	612.93	86.60	7.08
Pd_1In_{50}	580.50	16.13	35.98
Pd_1In_{100}	339.08	9.78	34.68
Spent Pd_1In_5	557.01	46.26	12.04
Spent Pd_1In_{50}	406.04	10.68	38.03
Spent Pd_1In_{100}	684.60	13.17	51.99

4.3.2 Coordination environment via X-ray absorption spectroscopy

X-ray absorption spectroscopy (XAS) at the Pd K-edge was performed to evaluate the chemical bonding and electronic structure of these samples with *in-situ* and *ex-situ* studies. The k^2-weighted magnitudes of the Fourier transforms of the *ex-situ* sample spectra in the extended X-ray absorption fine structure (EXAFS) regime are displayed in **Figure. 4.3a**. For the fresh samples, the XANES energy (23.2531 keV, **Table A1**) is characteristic of Pd^{+2}. The EXAFS shows a first shell peak at a phase-uncorrected distance of about 1.5 Å, attributed to Pd-O scattering. The fits of each sample indicate the presence of 4 Pd-O bonds at 2.05 Å, similar to the PdO reference. The higher shell peaks of the catalysts due to Pd-O-Pd scattering are much

smaller than those in PdO, indicating the presence of small oxide clusters which decrease in size with decreasing Pd content. Dilution greatly impacts this feature, which becomes negligible for the sample with highest Pd dilution (Pd_1In_{100}). This suggests that Pd_1In_{100} is the only sample which contains predominantly isolated Pd species.

The *ex-situ*, k^2-magnitudes of the used catalysts (**Figure 4.4**) indicate that the majority of Pd is present in a metallic Pd or PdIn alloy phase after reaction. In addition to the metallic peaks, there is a small fraction of oxidized Pd (i.e., peaks due to Pd-O) likely due to surface oxidation upon exposure to air. Since the atomic number of Pd and In differ by only 3, Pd-Pd and Pd-In configurations lead to almost identical scattering making it impossible to resolve these two scattering paths. However, the metallic Pd-M bond distance is shifted toward slightly larger R for the Pd_1In_{50} and Pd_1In_5 samples (inset of **Figure 4.3a**), indicating that strong interactions are present between Pd and In in these samples with different interatomic distances [142–144]. The Pd-M (M = Pd or In) coordination numbers (CN) in the used samples fall in the 4.6 to 5.7 range (**Table A1**), much smaller than that of bulk Pd (CN=12) which suggests that much of the Pd is present at the surface of the nanoparticles. The Pd-O CNs in these catalysts can additionally be utilized to estimate the fraction of the Pd which is present on the surface. Surface Pd readily oxidizes in air to yield PdO with a Pd-O CN of 4, thus dividing the measured Pd-O CN by 4 gives an estimation of the surface Pd content [145,146]. Pd_1In_{100} and Pd_1In_{50} materials have a similar CN of 1.3 (33% surface Pd) and 1.5 (38% surface Pd), respectively, whereas the CN of Pd_1In_5 decreases to 0.5 (13% surface Pd). The decrease in CN indicates that smaller portions of Pd atoms are located on the surface of Pd_1In_5 compared to Pd_1In_{100} and Pd_1In_{50} materials. Additionally, this suggests that increasing the Pd content from Pd_1In_{100} to Pd_1In_{50} minimally affects Pd accessibility, while increasing it further to Pd_1In_5 leads to a substantial decrease in

accessibility and therefore an inefficient use of this costly dopant metal. Pd_1In_{100} and Pd_1In_{50} therefore differ primarily in ensemble size rather than Pd dispersion, as the EXAFS data suggest Pd is predominantly isolated in the former material but clustered in the latter.

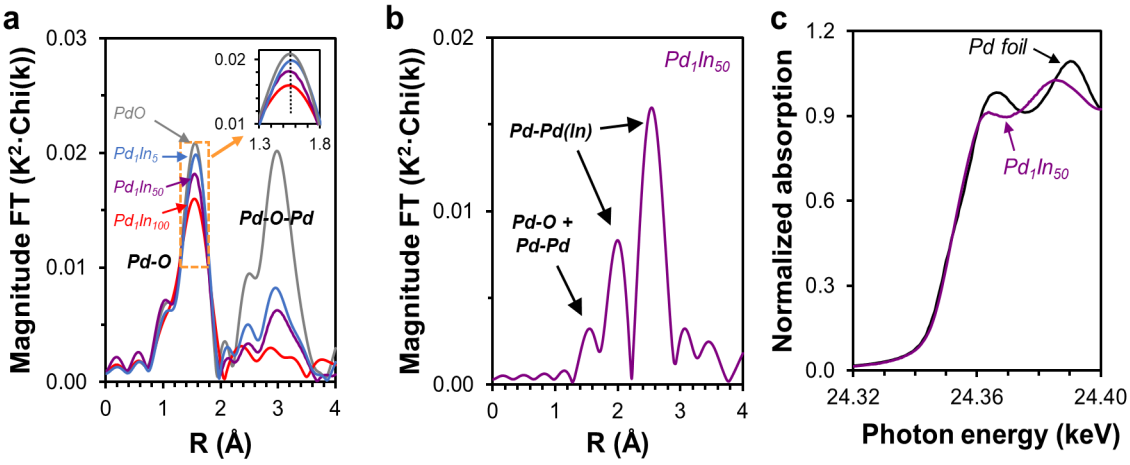

Figure 4.3: X-ray absorption spectroscopy of Pd-In alloys. (a) *Ex-situ* Pd-K edge EXAFS spectra reference PdO (gray) and fresh Pd_1In_{100} (red), Pd_1In_{50} (purple), and Pd_1In_5 (blue). Inset shows enlargement of the orange rectangular section. **(b)** *In-situ* reduced Pd_1In_{50} (purple). **(c)** Pd K-edge XANES for *in-situ* reduced Pd_1In_{50} (purple) and Pd foil reference (black).

Upon reduction of Pd_1In_{50} (analyzed *in-situ*), only metallic Pd-Pd/Pd-In scattering were observed (**Figure 4.3b**). This is consistent with the X-ray absorption near-edge spectroscopy (XANES) shown in **Figure 4.3c**. The XANES energies of these samples at the inflection of the leading edge are very similar to Pd foil (**Table A1**). The leading edge intensity and white line energy of Pd_1In_{50} differ substantially from those of Pd foil, however, which may indicate the presence of Pd-In neighbors (i.e. PdIn alloy formation). As discussed above, the Pd-Pd and Pd-In scattering paths are nearly identical, making deconvolution challenging. However, an average CN for the grouped Pd-Pd/Pd-In interaction can be measured to be 7.4 (**Table A1**), consistent with nanoparticles in the 2-3 nm range [147]. At this size, one would expect a contraction of the bond distance if all interactions were derived from pure Pd. However, the average bond distance is larger than that of a Pd foil (2.77 *vs* 2.75 Å), consistent with the formation of a Pd-In alloy.

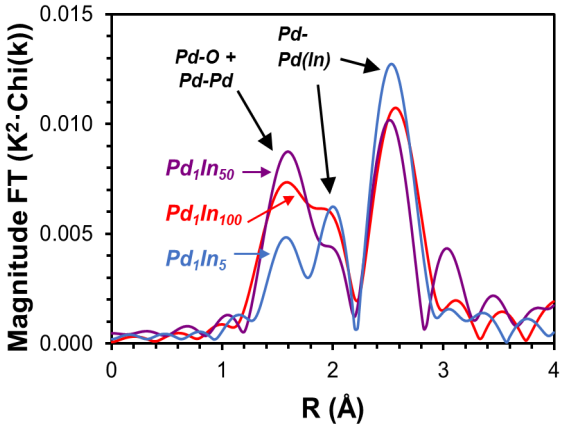

Figure 4.4: X-ray absorption spectroscopy of Pd-In alloys after reaction. *Ex-situ* Pd-K edge EXAFS spectra for used Pd_1In_{100} (red), Pd_1In_{50} (purple), and Pd_1In_5 (blue).

4.3.3 Ensemble size characterization via infrared spectroscopy of adsorbed CO

The ensemble sizes of Pd in the alloys were further investigated by diffuse reflectance infrared adsorption Fourier transform spectroscopy (DRIFTS) of adsorbed CO which possesses highly characteristic vibrational frequencies in the bound state. **Figure 4.5** shows a series of spectra in the range of 2250-1750 cm^{-1} for the fresh reduced catalysts and after reaction without further treatment. These measurements were recorded at room temperature during CO exposure (adsorption) and subsequent purge in He (desorption). The Pd_1In_{100} catalyst (**Figure 4.5a**) did not show any observable peaks for bound CO which suggests that any Pd present in the alloy surface is isolated since isolated Pd is known to adsorb CO much more weakly than pure Pd [148] and therefore would desorb rapidly prior to full evacuation of gaseous CO from the DRIFTS cell. The absence of a clear peak for CO bound to an isolated Pd atom has also been noted in several prior studies [48,149,150]. This notion that Pd is predominantly isolated in this sample is additionally consistent with the EXAFS data. With a higher Pd loading, the Pd_1In_{50} catalyst showed a clear adsorption band at a wavenumber of ~2050 cm^{-1}, lower than the 2070-2110 cm^{-1} region where CO linearly adsorbs atop Pd atoms [151–155]. This peak vanishes after 10 mins of CO desorption,

indicating weak binding to Pd relative to bulk Pd, thus the Pd here must exist in a highly dispersed form such as sub-nanometer clusters. The lack of any observable peak below 2000 cm^{-1} corresponding to CO adsorbed to two-fold and three-fold Pd sites [152,156] provides further evidence that the Pd_1In_{50} catalyst does not contain substantial amounts of extended Pd ensembles (**Figure 4.5b**). The alloy with the highest Pd content (Pd_1In_5) similarly showed an adsorption band near 2050 cm^{-1}, though it was much broader and quite persistent (remaining clearly visible after 20 minutes of CO desorption). No peak associated with bridge bound CO was detected below 2000 cm^{-1}. The increased persistence and breadth of the 2050 cm^{-1} band is consistent with the Pd_1In_5 alloy comprising ensembles which are larger on average and less uniform than those in Pd_1In_{50}, a notion also supported by STEM and EXAFS. In combination with the data discussed prior, these results allow for the three materials to be classified by their dominant states of Pd aggregation: isolated atoms for Pd_1In_{100}, small clusters for Pd_1In_{50}, and large clusters for Pd_1In_5.

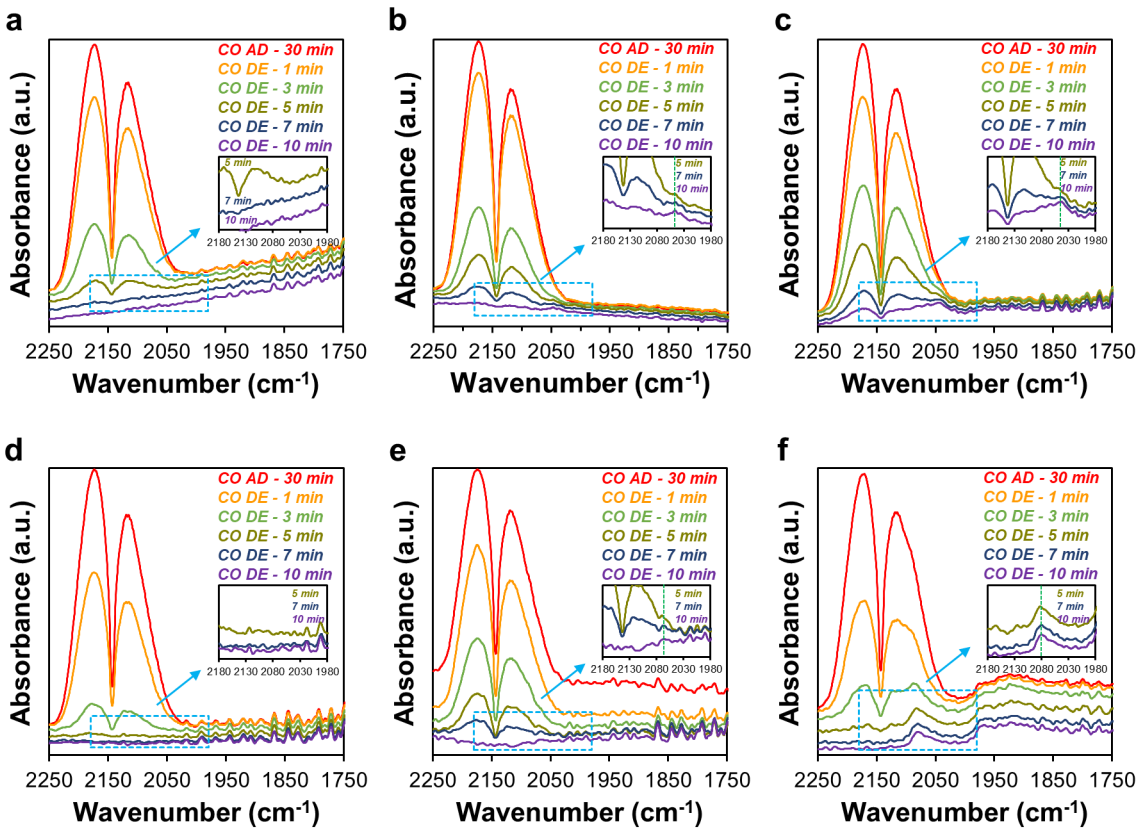

Figure 4.5: FTIR spectra of CO adsorbed at room temperature for PdIn catalysts as a function of Pd loading. (a-c) Fresh reduced Pd1In100, Pd1In50, and Pd1In5, respectively. (d-f) Used Pd1In100, Pd1In50, and Pd1In5, respectively. The labels in the upper right corner indicate CO adsorption (CO AD) and CO desorption (CO DE) via He purge. Insets show the enlarged picture of the corresponding rectangle section.

This classification becomes clearer in the analyses of post-reaction samples prior to CO uptake (**Figure 4.5d-f**). The Pd_1In_{100} catalyst does not show any new bands, suggesting that isolated Pd atoms do not aggregate under reaction conditions when sufficiently diluted in In (**Figure 4.5d**). The Pd_1In_{50} catalyst does show some change after reaction with a subtle blue shift in the peak at ~2050 by ~20 cm^{-1} to ~2070 cm^{-1} though this may be due to partial oxidation of Pd atoms in air [157]. As with the Pd_1In_{50} catalyst, no features below 2000 cm^{-1} developed from the reaction, suggesting that these small Pd ensembles do not aggregate to form extended ensembles under reaction conditions. A blue-shift in the peak at ~2050 cm^{-1} was also observed with the Pd_1In_5 material, though the most pronounced change was in the regime below 2000 cm^{-1} where a

broad feature appeared indicating the presence of highly non-uniform bridge and hollow sites (**Figure 4.5f**). These features—which are associated with strong-binding sites as indicated by their persistence after an extended desorption period—are likely derived from CO adsorption to large Pd ensembles. These ensembles are therefore less stable under reaction conditions than the smaller ensembles. These *in-situ* CO-DRIFTS experiments therefore suggest strongly that the fresh and spent catalysts have unique surface structures, though further characterizations were performed to support this notion.

4.3.4 Implications of Pd-In alloy surface structure and cluster size on CO_2 hydrogenation

To probe the effect of the different Pd ensemble sizes on CO2 hydrogenation performance, the three alloy catalysts (Pd_1In_{100}, Pd_1In_{50}, and Pd_1In_5 on Al_2O_3) along with In/Al_2O_3 and Pd/Al_2O_3 were tested for CO_2 hydrogenation to methanol, as described in the materials and characterization section. At the tested reaction temperatures (240-300°C), all three Pd-In catalysts were stable for over 24 hours (**Figure 4.6**) with methanol and CO comprising >80% of the analyzed products. At elevated temperatures (e.g. >260°C), dimethyl ether and methane were also produced, accounting for the remaining products.

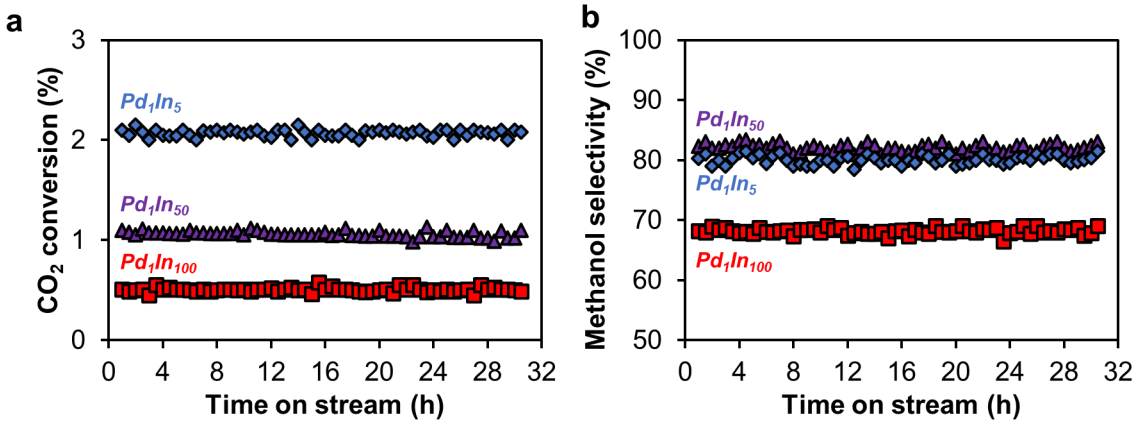

Figure 4.6: Stability test of Pd-In alloy catalysts for over 24h. (a) CO_2 conversion of $Pd\text{-}In/Al_2O_3$ catalysts with different Pd loading at 260°C, 30 bar, $H_2:CO_2$=3:1, and GHSV=9000h^{-1} **(b)** Methanol selectivity for the aforementioned catalysts under similar reaction condition as (a).

The addition of Pd to In was found to promote the reaction regardless of Pd loading with the CO_2 conversion increasing from 0.2% with In to 0.5, 1.1, and 2.1% for Pd_1In_{100} (isolated Pd), Pd_1In_{50} (small Pd clusters), and Pd_1In_5 (large Pd clusters), respectively, at 260°C (**Figure 4.7a**). In addition to improving the CO_2 conversion, the presence of Pd shifted the product formation more toward methanol especially when clusters were present. Pd_1In_{50} exhibited the highest methanol selectivity of 82% while Pd_1In_5 was similar (80%) and Pd_1In_{100} was considerably lower (68%) though still higher than In (62%) (**Figure 4.7b**). While Pd/Al_2O_3 on its own is catalytically active for CO_2 conversion under these conditions, it is much less selective—only 5% of the CO_2 converted at 0.5% conversion becomes methanol. In addition to demonstrating the impact of Pd ensemble size on selectivity, this result also confirms that the galvanic replacement method was effective in depositing Pd exclusively on the In nanoparticles rather than the Al_2O_3 support (which would have led to low methanol selectivities), in agreement with the STEM/EDS and XRD results.

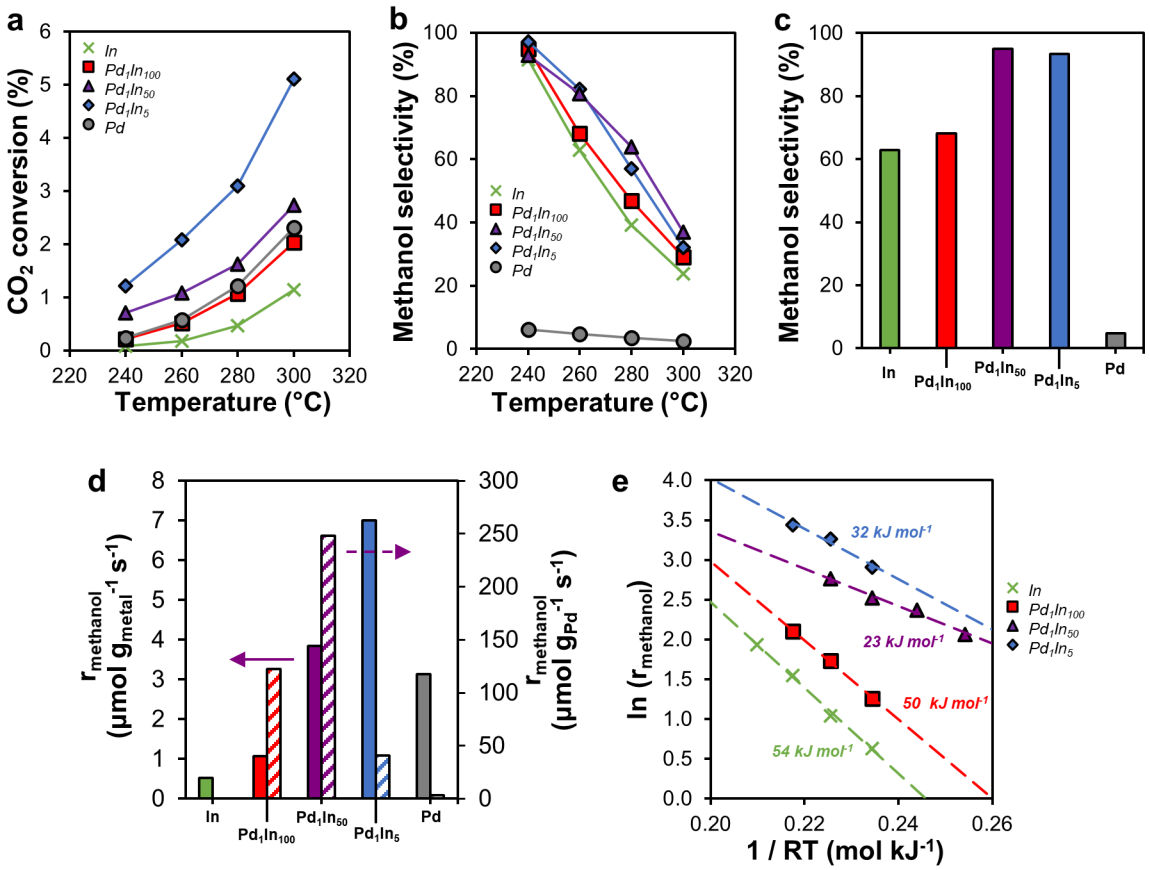

Figure 4.7: Catalytic performance of Pd-In alloy catalysts. (a) CO_2 conversion of Pd-In/Al_2O_3 catalysts with different Pd loading at various reaction temperatures (H_2:CO_2=3:1, 30 bar, GHSV=9000 h^{-1}), compared to In/Al_2O_3 and Pd/Al_2O_3. **(b)** Methanol selectivity for the aforementioned catalysts under similar reaction condition as (a). **(c)** Methanol selectivity at 260°C, 30 bar, H_2:CO_2=3:1, GHSV adjusted to obtain ~0.5% conversion for all catalysts. **(d)** Methanol synthesis rate per gram metal and per gram Pd at ~0.5% conversion. **(e)** Arrhenius plot (rate in units of µmol $g_{catalyst}^{-1}$ min^{-1}) and activation energies for the investigated catalysts. Subscripts indicate nominal molar ratios of metals. Pd_1In_{100} catalyst contains predominantly isolated Pd, Pd_1In_{50} contains small Pd clusters, Pd_1In_5 contains extended Pd ensembles.

These trends in selectivity additionally hold when comparing the materials at a fixed conversion of ~0.5% at 260°C (**Figure 4.7c**). The methanol selectivity increased upon addition of Pd to In from 62% for pure In to 68, 95, and 93% for Pd_1In_{100}, Pd_1In_{50}, and Pd_1In_5, respectively. These results are in line with the results obtained by Frei et al. for their Pd/In_2O_3 catalysts in which the single atom catalysts yielded lower methanol selectivities than the ones with different Pd cluster sizes. However, Frei et al. also showed that when the Pd cluster size is larger than two atoms, the catalyst starts to behave like metallic Pd and the methanol production

is compromised [48]. A similar deleterious behavior was not observed in the present study, as no significant decline in the methanol selectivity was detected between Pd_1In_{50} and Pd_1In_5. Our results instead demonstrate that aggregated Pd within In, even at the relatively high loadings present in Pd_1In_5, remains selective to methanol whereas Pd clusters on In_2O_3 do not. This result reveals an important distinction between the catalytic performance of Pd sites in metal-on-oxide single (or few) atom catalysts and the metal-in-metal alloys present in our series of materials. Indeed, the synthesis approach utilized in this work allowed for the manipulation of Pd loading and structure to a greater extent than the prior work with In_2O_3 supports (which relied on conventional synthesis methods such as dry impregnation and coprecipitation), while maintaining high methanol selectivity and abating CO formation.

The catalyst possessing small clusters of Pd utilized the Pd most efficiently based on differences in methanol synthesis rate per Pd atom at constant conversion. Normalizing rates to the total metal loading (Pd+In) shows In to be the least active and Pd_1In_5 to be the most active, but the improvement in synthesis rate from Pd_1In_5 to Pd_1In_{50} does not scale with Pd content. As a result, the rate per Pd atom (here referred to as the turnover frequency, TOF) for Pd_1In_{50} is two times that of Pd_1In_{100}, six times that of Pd_1In_5, and 80 times that of pure Pd. This may indicate that the large clusters in the Pd_1In_5 catalyst are less reactive than the small clusters in Pd_1In_{50}.

The different dependencies of rate on temperature for the In-based materials further support our hypothesis that distinct active sites comprised of different Pd ensemble sizes give rise to the different catalytic performances of each catalyst (**Figure 4.7e**). The activation energy on pure In (54 +/- 2 kJ mol^{-1}) is similar to that of Pd_1In_{100} (50 +/- 2 kJ mol^{-1}) while substantially higher than that of Pd_1In_{50} (23 +/- 2 kJ mol^{-1}), which is just below that of Pd_1In_5 (32 +/- 6 kJ mol^{-1}). These activation energy differences suggest that the active sites themselves change with

dilution, especially when comparing Pd_1In_{50} and Pd_1In_5 to Pd_1In_{100}. The non-monotonic relationship between apparent activation energy and Pd content further highlights the important point that Pd ensembles larger than an atom but smaller than those in bulk Pd nanoparticles are the most efficient active sites for the CO_2 hydrogenation reaction.

Together these data show that the most effective spatial arrangement of Pd atoms in Pd-In alloys for CO_2 hydrogenation is a small cluster. The lower Pd-specific rate for Pd_1In_5 (large clusters) *vs* Pd_1In_{50} (small clusters) can be explained by 1) the more extensive partitioning of Pd into the inaccessible bulk and 2) the lower fraction of surface Pd atoms which are adjacent to In atoms. The importance of the Pd-In interface for selective hydrogenation has been noted for Pd/In_2O_3 catalysts in DFT studies performed by Ge and co-workers, which indicated that the interfacial Pd-In sites of 4-atom and 13-atom Pd clusters possessed similar reactivities [158]. Smaller Pd clusters therefore yield higher rates per Pd atom since a larger fraction of the Pd within them is present at this interface. The beneficial shift in hydrogenation reactivity and selectivity between isolated Pd and Pd atoms in close proximity has also been noted in Au, Ag, and Ga hosts. While isolated Pd in Au is capable of dissociating H_2, the resulting H atoms are not strongly stabilized because they interact very weakly with Au [159–161]. Clusters of Pd provide bridge and hollow sites where H atoms can be strongly stabilized via coordination with multiple Pd atoms. Friend and co-workers showed how this shifts the rate-limiting step in H_2/D_2 exchange from dissociation (of H_2 or D_2) to re-association (of H with D) and increases the overall reaction rate [162]. While the subsequent spillover step from Pd to Au does not appear to be rate-limiting to H_2/D_2 exchange, its endothermic nature has raised questions about the ability of the dissociated hydrogen to participate substantially in catalytic reactions on these materials. This is thought to be the case in PdAg catalysts as well as noted by Greiner and co-workers, with acetylene

hydrogenation benefitting from Pd concentrations high enough to bring Pd atoms sufficiently close together for H_2 dissociated on one Pd atom to be accessible to acetylene bound to another [163]. Electronic factors also play an important role in these materials, especially in the PdGa intermetallics prepared from high-temperature melts investigated by Armbrüster and co-workers [164]. In these structures the Pd atoms are formally isolated from one another in both PdGa and Pd_2Ga stoichiometries, though the latter material contains Pd atoms in closer proximity (2.8 *vs* 3.0 Å shortest Pd-Pd distance) and has a d-band with a substantially higher density of states at the Fermi level (0.3 *vs* 0.1 eV^{-1} $atom^{-1}$). These changes underly a 30 time increase in acetylene hydrogenation rate for Pd_2Ga over PdGa. A Pd_2In intermetallic produced in the same manner showed comparable catalytic behavior due to similarities in electronic structure, though the dilution effect was not critiqued for this material. Altogether these prior findings provide support for the notion that geometric, mechanistic, and electronic effects may be responsible for the trends observed here, where small clusters of Pd yield the most efficient Pd-In alloys for CO_2 conversion to methanol.

4.4 Conclusions

Pd-In alloys with distinct atomic configurations were synthesized via galvanic replacement and utilized to promote the selective hydrogenation of CO_2 to methanol. Obtaining definitive conclusions regarding atomic ensembles in dilute alloys from any one characterization method presents a major challenge due to the low signals these materials typically yield, thus we probed Pd-In alloy structures here using a multi-pronged approach. The synthesis method employed enabled the production of alloys with distinct Pd ensembles which yielded stable catalytic performance in this reaction. Our findings further lead us to conclude that Pd can be most efficiently used to promote selective CO_2 hydrogenation to methanol (up to 95%

selectivity) when present in small clusters, while isolated Pd is both less reactive and selective and large clusters of Pd inefficiently trap Pd below the nanoparticle surface or in the interior of Pd islands, away from reactive Pd-In interfaces. Developing further understandings of how to manipulate galvanic replacement to generate unique reactive structures in dilute alloys on under-researched host metals, such as In, and examining how these materials behave with less "innocent" supports will expand the toolkit that catalysis researchers have to address sustainability challenges in synthesizing the chemicals which underpin the global economy.

CHAPTER 5: Controlled Deposition of Palladium Atoms on Cu/In_2O_3 by Galvanic Replacement

5.1 Introduction

Supported metal catalysts are employed in various chemical applications, including in selective hydrogenation, selective oxidation, and selective reduction [165–167]. The catalytic performance of such a material is determined by a number of factors including surface, interface, electronic structures, and metal particle size [168,169]. The reactivity, selectivity, and stability of the catalyst may be further tuned by alloying the primary metal with other metals, typically, noble metals [170]. In the published literature, typically, traditional synthesis techniques including impregnation, sequential deposition, co-precipitation, and sol-gel methods are used to synthesize catalytic alloys. However, these synthesis techniques often result in surface inhomogeneity and lack atomic level precision that is required to design precise surface structures, particularly for bi- and tri-metallic catalyst systems, thus, making establishing structure-activity relationships rather difficult [171,172]. As such, it is imperative to seek a facile and versatile synthesis method, one that provides flexibility and control over different parameters for optimal catalyst design.

Galvanic replacement, as a synthesis technique, has garnered much attention in the literature due to its ability to fabricate nanostructured materials and multi-metallic catalysts with well-defined surface structures and distinct atomic arrangements [173–176]. In principle, galvanic replacement is an electro-chemical process that utilizes the difference in the electrical reduction potential between two metals, the host metal and dopant metal, and requires that the dopant metal to have a more positive potential for galvanic replacement to proceed [177]. For instance, Wang et al. used galvanic replacement to selectively replace Fe atoms with Ru atoms in Pt-Fe-type nanoparticles, resulting in the formation of a different alloy than the parent alloy, which had

an improved catalytic performance than bimetallic Pt-Fe nanoparticles [178,179]. Furthermore, Miyazaki et al. modified the surface of $PdZn/SiO_2$ by replacing surface metallic Zn atoms with Pb [137]. The modified catalyst showed a better catalytic performance compared to the Pd-Zn bimetallic and Pd-Zn-Pb tri-metallic catalysts, which was attributed to the steric effect from the specific surface structure of surface Pb. Wang et al. demonstrated another key capability of galvanic replacement. Specifically, the authors selectively replaced Co and Cu atoms in Pd_6CoCu/C nanoparticles by Au atoms without distributing the structure of the host particle, that is, Pd_6CoCu/C (in spite of the Au atoms penetrating the Pd–Co–Cu lattice) [180]. All of these results point to the suitability of galvanic replacement as a synthesis technique for the synthesis of supported alloy-type catalysts.

Indium (In) and In-based catalysts have received considerable interest recently due to their catalytic performance in ethane dehydrogenation, nitrate reduction, acetylene hydrogenation, semi hydrogenation of alkynes, reverse water gas shift, methanol steam reforming, and methanol synthesis [44,144,181,182]. Furthermore, several studies demonstrated that alloying different metals with indium results in different catalytic activity. For instance, metals which are known to be unselective for methanol, such as cobalt (Co), nickel (Ni), and rhodium (Rh), became methanol selective catalysts due to the strong interaction between the two metals and change in their electronic structure [49,183–185].

Inspired by these findings, we utilized the reduction step of Cu/In_2O_3 nanoparticles in the galvanic replacement reaction to synthesize two different Pd alloys on indium support by modifying the surface of Cu/In_2O_3 nanoparticles via selective deposition of Pd atoms on the surface of different host metals. The change of the catalytic activities of the two synthesized alloys were assessed in CO_2 hydrogenation-to-methanol and reverse water gas shift reaction

(RWGS). The structures of the synthesized catalysts were characterized by inductively coupled plasma atomic emission spectroscopy (ICP-AES), X-ray diffraction (XRD), hydrogen temperature programmed reduction (H_2-TPR), and aberration-corrected scanning transmission electron microscopy (STEM).

5.2 Experimental

5.2.1 Catalyst preparation

5.2.1.1 Synthesis of In_2O_3

In_2O_3 was synthesized by a controlled calcination of Indium hydroxide ($In(OH)_3$) which was a precipitated by dissolving $In(NO_3)_3 \cdot xH_2O$ (Aldrich, 99.99%) in 94 mL of deionized water, followed by the addition of 18mL of NH_4OH (28 wt.% in H_2O). The resulting slurry was aged at 80°C for 60 mins before the precipitate was collected by filtration and washed with deionized water (2 L). The obtained solid was dried under vacuum at 65°C for 12 hrs and calcined at 350°C (5°C min^{-1}) for 3 hrs.

5.2.1.2 Synthesis of Cu/In_2O_3

Cu supported on In_2O_3 was synthesized via incipient wetness impregnation (IWI) where a desired amount of copper (II) nitrate hydrate, $Cu(NO_3)_2 \cdot xH_2O$ (Aldrich, 99.999%), was dissolved in deionized water and then impregnated on In_2O_3 (~0.624 mL/g_{In2O3}). The as-synthesized catalyst was then dried over night at 65°C and calcined at 300°C (5°C min^{-1}) for 3 hrs.

5.2.1.3 Synthesis of Pd_1Cu_{100}/In_2O_3-LRT and Pd_1Cu_{100}/In_2O_3-HRT

The obtained Cu/In_2O_3 was reduced at 215°C (10°C min^{-1}), for Pd_1Cu_{100}/In_2O_3-LRT (Low Reduction Temperature), and 350°C (10°C min^{-1}), for Pd_1Cu_{100}/In_2O_3-HRT (High

Reduction Temperature), under 5% H_2 in Ar (20 mL min^{-1}) for 2 hrs. Separately, 150 mL of DI-water was brought to a boil under reflux in an argon environment. Sodium borohydride, $NaBH_4$ (Aldrich, 99%), was added dropwise to the water to reach a concentration of 0.1 M and stirred for 15 minutes. The reduced In_2O_3 was added to the boiled DI water without exposure to air. To further prevent the oxidation of the supported In_2O_3, 0.1 M ascorbic acid (Aldrich, 99%) was added to the solution after 15 minutes of stirring. The subsequent addition of Pd atoms to In or Cu nanoparticles was then achieved via galvanic replacement where the Pd precursor is favorably reduced by the host metal, according to the following two half-reactions:

$$Pd^{2+} + \ In^0 \rightarrow Pd^0 + In^{3+} \qquad \Delta E^o = 1.28\,V$$

$$Cu^0 + Pd^{2+} \rightarrow \ Cu^{2+} + Pd^0 \qquad \Delta E^o = 0.575\,V$$

To achieve this, a desired amount of palladium (II) nitrate hydrate, $Pd(NO_3)_3 \cdot xH_2O$, (Aldrich) was dissolved in DI H_2O and then added to the solution while stirring. The resulting material was filtered and washed with 1 L of DI H_2O. The acquired powder was then dried overnight under vacuum at 120°C.

5.2.2 Catalytic Testing

The catalytic performance of the Pd_1Cu_{100}/In_2O_3-LRT and Pd_1Cu_{100}/In_2O_3-HRT materials was assessed for CO_2 hydrogenation to methanol and reverse water-gas shift (RWGS) reaction. For the CO_2 hydrogenation to methanol reaction, the catalysts were evaluated in a fixed bed reactor at a pressure of 30 bar, at temperatures between 240 and 300°C, and with a gas-hourly space velocity (GHSV) of 9000 h^{-1}. The reactor was loaded with 0.4 g of catalyst (sieved to 125-250 μm) between two beds of quartz wool. The catalysts were reduced prior to reaction under 20% H_2 in Ar at 350°C (10°C/min) and atmospheric pressure for 1 h. After reduction, a premixed feed of H_2 and CO_2 (3:1 molar ratio) was introduced to the reactor via mass flow

controllers at 30 bar. Once the reaction reached a steady state after 90 mins, the product mixture was analyzed online by two gas chromatographs: one equipped with a thermal conductivity detector (TCD) to quantify CO, CO_2 and H_2, and one equipped with a flame ionization detector (FID) to quantify methanol, methane, and dimethyl ether. All reactor effluent lines were heated above 100°C to prevent product condensation.

For the RWGS reaction, the catalysts were evaluated in a fixed bed reactor at atmospheric pressure, at temperatures between 200 and 500°C, and with a gas-hourly space velocity (GHSV) of 27000 h^{-1}. The reactor was loaded with 0.05 g of catalyst (sieved to 125-250 μm) between two beds of quartz wool. The catalysts were reduced prior to reaction under 20% H_2 in Ar at 300°C (10°C/min) and atmospheric pressure for 1 h. After reduction, a premixed feed of H_2 and CO_2 (1:1 molar ratio) was introduced to the reactor via mass flow controllers at atmospheric pressure. Once the reaction reached steady state after 30 mins, the product mixture was analyzed online by gas chromatograph was equipped with a thermal conductivity detector to quantify CO, CO_2 and H_2. All reactor effluent lines were heated above 100°C to prevent product condensation. For both reactions, the operating conditions were chosen to operate far away from equilibrium.

5.2.3 Catalyst Characterization

Inductively coupled plasma atomic emission spectroscopy (ICP-AES) measurements were conducted on a Leeman Labs PS1000 instrument. The catalyst samples were digested in 2 mL of an aqua regia solution overnight and then further diluted in DI-H_2O to obtain a desired concentration (typically 1-100 ppm) of the metal at a neutral pH. X-ray diffraction (XRD) was performed on a Rigaku instrument. Cu Kα radiation was used with a power setting of 40 mA and 45 kV. Data were collected for 2θ between 10° and 70° with a step size of 0.01° and a scan speed

of 0.15° min^{-1}.

H_2-temperature programmed reduction measurements were conducted using a Micromeritics AutoChem 2920 equipped with a thermal conductivity detector. The reduction measurements were carried out by exposing the sample to a 50 mL min^{-1} of 20% H_2/Ar while ramping the temperature linearly and monitoring with TCD. Scanning transmission electron microscopy imaging and energy dispersive X-ray spectroscopy (STEM-EDS) as well as high resolution transmission electron microscopy (HRTEM) were performed using a JEOL NEOARM operated at an accelerating voltage of 200 kV equipped with field emission electron gun. A condenser lens aperture of 40 μm was used. For imaging and EDS, a camera length of 4 cm and a probe current of 150 pA were used

5.3 Results and Discussion

5.3.1 Characterization of Pd_1Cu_{100}/In_2O_3-LRT and Pd_1Cu_{100}/In_2O_3-HRT

Two different materials were synthesized utilizing galvanic replacement, where Pd atoms are deposited on Cu/In_2O_3 nanoparticles. The nominal loadings of palladium and copper in the synthesized catalysts were closely matched as confirmed by inductively coupled plasma atomic emission spectroscopy (ICP-AES) (**Table 5.1**).

Table 5.1: Copper and palladium compositions as measured by ICP-AES

Catalyst	Cu nominal loading (wt%)	Cu measured loading (wt%)	Pd nominal loading (wt%)	Pd measured loading (wt%)
Pd_1Cu_{100}/In_2O_3-LRT	5.0	4.75	0.05	0.045
Pd_1Cu_{100}/In_2O_3-HRT	5.0	4.75	0.05	0.043

Figure 5.1 shows X-ray diffraction (XRD) patterns of the as-synthesized Cu/In_2O_3, Pd_1Cu_{100}/In_2O_3-LRT, and Pd_1Cu_{100}/In_2O_3-HRT catalysts. XRD patterns of all three catalysts

show similar peaks, thus, suggesting that adding a small amount of Pd through galvanic replacement does not change the lattice structure of the host metal, that is, copper or indium, which is similar to what has been reported in the literature [186]. Furthermore, the XRD patterns of Pd_1Cu_{100}/In_2O_3-LRT and Pd_1Cu_{100}/In_2O_3-HRT catalysts do not show any characteristic diffraction peaks for Pd or PdM (M=Cu,In) alloys.

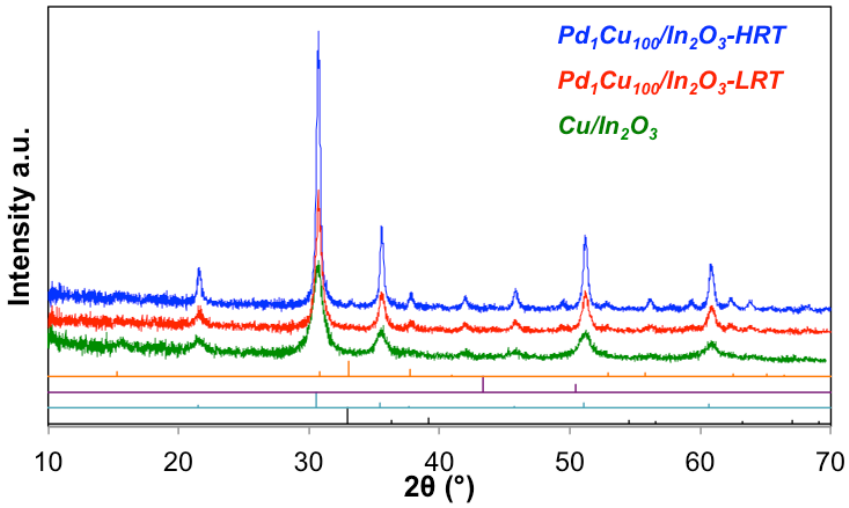

Figure 5.1: XRD diffractograms of Pd_1Cu_{100}/In_2O_3-LRT, and Pd_1Cu_{100}/In_2O_3-HRT, and Cu/In_2O_3 Reference diffractograms of CuIn (orange), Cu (purple), In_2O_3 (light blue), and In (black) (JCPDS 04-008-0042, 00-004-0836, 00-006-0416, and 00-005-0642 respectively).

The reduction behavior of the two synthesized catalysts along with Cu/In_2O_3 reference was investigated by H_2-temperature programmed reduction (H_2-TPR), as shown in **Figure 5.2**. The H_2-TPR of Cu/In_2O_3 material shows a narrow peak centered at ~173°C which is attributed to Cu [136,187]. The TPR profiles of the catalysts containing Pd, namely Pd_1Cu_{100}/In_2O_3-LRT, and Pd_1Cu_{100}/In_2O_3-HRT, reveal a shift in the reduction temperature of Cu to a lower temperature indicating that that there is close contact between Cu and Pd in these samples, as Pd is known to accelerate the reduction of its host metal when alloyed [188–191]. For $100PdCu/In_2O_3$-HRT, H_2-

TPR shows that the Cu reduction peak center is shifted to ~150°C and the peak has a shoulder which corresponds to the reduction of Pd. Similarly, TPR of Pd_1Cu_{100}/In_2O_3-LRT reveals that Cu is reduced at an even lower temperature of ~ 133°C compared to Pd_1Cu_{100}/In_2O_3-HRT and the peak has a similar shoulder which also attributed to the reduction of Pd. The change in the reduction temperature of Cu suggests that when Pd is alloyed with Cu in Pd_1Cu_{100}/In_2O_3-LRT, the reduction of Cu is further reduced compared to when Pd is alloyed with Cu and/or In in Pd_1Cu_{100}/In_2O_3-HRT.

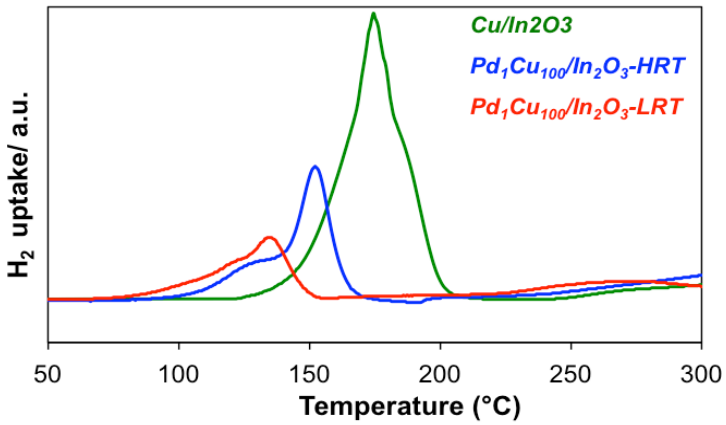

Figure 5.2: H_2-TRP profile of Pd_1Cu_{100}/In_2O_3-LRT, Pd_1Cu_{100}/In_2O_3-HRT, and Cu/In_2O_3

In an effort to visualize the location of Pd atoms, the synthesized catalysts were characterized by high angle annular dark-field scanning transmission electron microscopy (HAADF-STEM) and energy dispersive X-ray spectroscopy (EDS) (**Figure 5.3**). Pd atoms were not detected in HAADF-STEM-EDS, although they were detected in ICP, which is likely due to the low Pd loading.

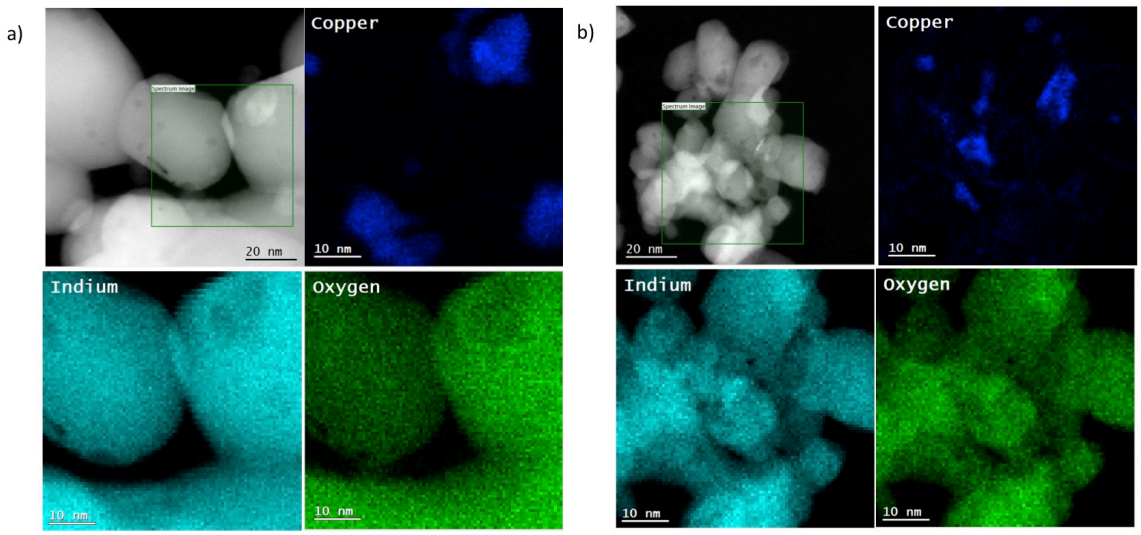

Figure 5.3: HAADF-STEM images of synthesized catalysts and their elemental mapping. **(a)** Pd_1Cu_{100}/In_2O_3-HRT **(b)** Pd_1Cu_{100}/In_2O_3-LRT

5.3.2 Catalytic performance of Pd_1Cu_{100}/In_2O_3-LRT and Pd_1Cu_{100}/In_2O_3-HRT

CO_2 hydrogenation to methanol and RWGS experiments were carried out to investigate the effect of Pd location on reactivity (**Figure 5.4** and **Figure 5.5**). **Figure 5.4a** shows that the CO_2 conversion over Pd_1Cu_{100}/In_2O_3-LRT surpasses that over Pd_1Cu_{100}/In_2O_3-HRT in the CO_2 hydrogenation to methanol reaction at all tested temperatures (240-300°C). For instance, the CO_2 conversion over Pd_1Cu_{100}/In_2O_3-LRT reaches ~1.3% compared to ~1.0% for Pd_1Cu_{100}/In_2O_3-HRT at 240°C and it increases with temperature reaching ~4.8% for Pd_1Cu_{100}/In_2O_3-LRT and ~3.4% for Pd_1Cu_{100}/In_2O_3-HRT at 300°C. On the other hand, Pd_1Cu_{100}/In_2O_3-HRT is more selective toward methanol (**Figure 5.4b**). Specifically, Pd_1Cu_{100}/In_2O_3-HRT exhibits ~97% methanol selectivity at 240°C compared to ~90% for Pd_1Cu_{100}/In_2O_3-LRT, and as the temperature increases, the methanol selectivities decrease reaching ~48.5% and ~23% at 300°C for Pd_1Cu_{100}/In_2O_3-HRT and Pd_1Cu_{100}/In_2O_3-LRT, respectively. To gain further insight into the impact of the Pd deposit site on reactivity, we performed kinetics experiments on both catalysts.

Figure 5.4c shows that apparent activation energy for Pd_1Cu_{100}/In_2O_3-HRT (E=43.7±4.7 kJ/mol) is ca. 5% lower than Pd_1Cu_{100}/In_2O_3-LRT (E=49.2±1.7 kJ/mol).

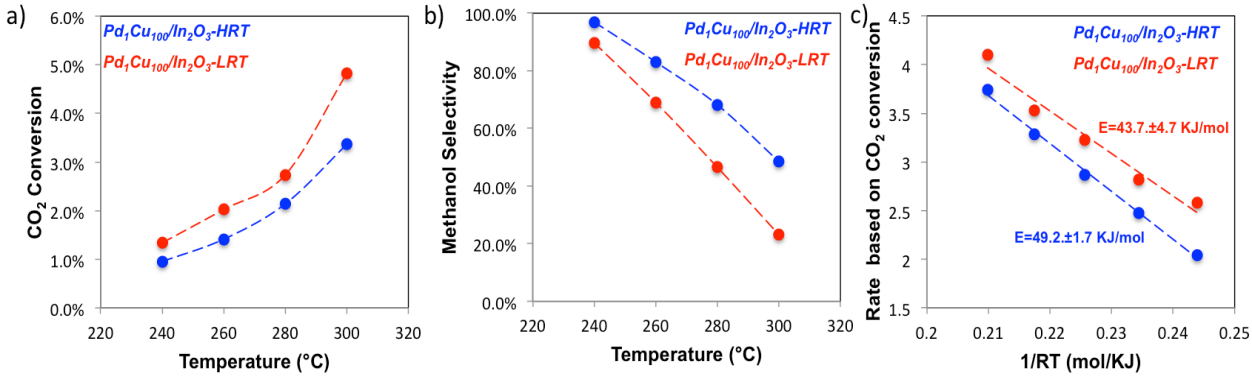

Figure 5.4: Catalytic performance of investigated catalysts for CO_2 hydrogenation to methanol reaction. **(a)** CO_2 conversion over Pd_1Cu_{100}/In_2O_3-HRT and Pd_1Cu_{100}/In_2O_3-LRT catalysts at various reaction temperatures (H_2:CO_2=3:1, 30 bar, GHSV =9000h^{-1}). **(b)** Methanol selectivity for the aforementioned catalysts under similar reaction conditions as (a). **(c)** Arrhenius plot and calculated activation energy for the investigated catalysts.

In the RWGS reaction, both catalysts were tested over a wide range of temperatures (200-500°C). Our data show that the catalysts were inactive for RWGS reaction at 200°C; however, when the temperature is increased to 250°C, only Pd_1Cu_{100}/In_2O_3-LRT was active, as shown in **Figure 5.5**. As the temperature further increases, the CO_2 conversion over Pd_1Cu_{100}/In_2O_3-LRT surpasses Pd_1Cu_{100}/In_2O_3-HRT up until 350°C. The CO_2 conversion over Pd_1Cu_{100}/In_2O_3-LRT reaches ~4.20% at 350°C compared to ~ 3.40% for Pd_1Cu_{100}/In_2O_3-HRT. Increasing the temperature further to 400°C results in a higher CO_2 conversion of ~12% for Pd_1Cu_{100}/In_2O_3-HRT, whereas, only ~10.70% CO_2 conversion was achieved over Pd_1Cu_{100}/In_2O_3-LRT. As the temperature increases further, both catalysts start to show similar activity, reaching CO_2 conversion of ~28.8% and ~28.5% for Pd_1Cu_{100}/In_2O_3-HRT and Pd_1Cu_{100}/In_2O_3-LRT, respectively. The similar reactivities exhibited by the two catalysts at high temperatures could be

attributed to: 1) Pd migration from one host metal to another as indium is reduced with increasing reaction temperatures, and/or 2) changes in the nature of the active site from Pd-alloy to metallic indium (since the majority of the catalyst consists of indium), as both catalysts are reduced *in-situ*, thus, effectively transforming In_2O_3 to In.

The kinetic experiments performed on both catalysts show that the Pd_1Cu_{100}/In_2O_3-LRT has an apparent activation energy of E=63.6±1.2 kJ/mol compared to E=81.6±7.2 kJ/mol for Pd_1Cu_{100}/In_2O_3-HRT (**Figure 5.5e)**. These activation energy differences suggest that different active sites are at play for Pd_1Cu_{100}/In_2O_3-HRT and Pd_1Cu_{100}/In_2O_3-LRT, consistent with the hypothesis that Pd is present in different environments for the two materials.

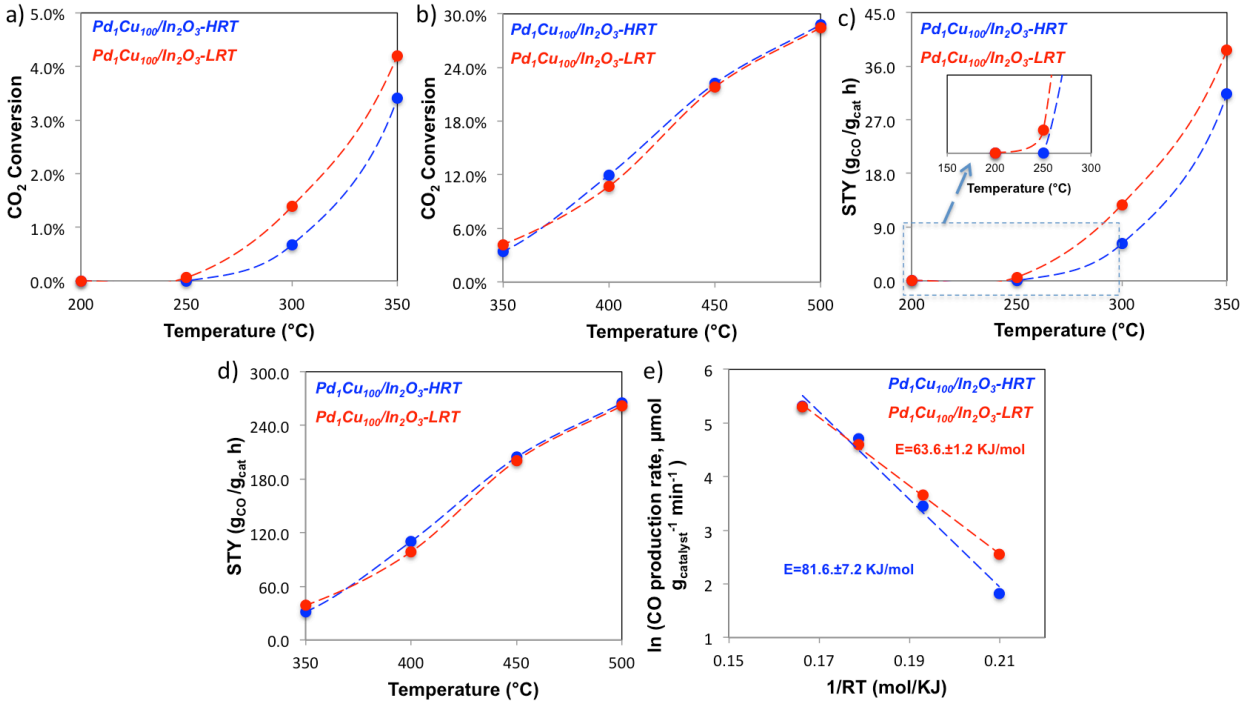

Figure 5.5: Catalytic performance of investigated catalysts for reverse water gas shift reaction. **(a)** CO_2 conversion over Pd_1Cu_{100}/In_2O_3-HRT and Pd_1Cu_{100}/In_2O_3-LRT catalysts at 200-350°C. **(b)** CO_2 conversion of the aforementioned catalyst at 350-500°C (H_2:CO_2=1:1, 1 atm, GHSV =27000h^{-1}). **(c)** CO space time yield (STY) for the aforementioned catalysts under similar reaction conditions as (a). **(d)** CO space time yield (STY) for the aforementioned catalysts under similar reaction conditions as (b). **(e)**

Arrhenius plot and calculated activation energy for the investigated catalysts. Inset in (**c**) shows the enlarged picture of the corresponding rectangle section

5.4 Conclusions

Two different materials were synthesized by controlling the reduction temperature step during the galvanic replacement reaction. The two materials were tested in the CO_2 to methanol and reverse water gas shift reactions and characterized by ICP, XRD, H_2-TRP, and STEM. Based on the characterizations preformed thus far, along with the catalytic activities for both reactions, we speculate that Pd atoms are deposited on different host metals forming different Pd alloys. In order to obtain a conclusive answer, though, two more catalysts were synthesized with a higher Pd loading of 0.5 wt% and sent to our collaborators for STEM imaging and X-ray absorption spectroscopy (XAS) measurements.

CHAPTER 6: Conclusions and Future Work Recommendations

6.1 Summary of thesis conclusion

In this thesis, two different strategies were utilized to overcome the thermodynamic stability of CO_2, in converting it to value-added chemicals: thermodynamic analysis and material science. In chapters 2 and 3, thermodynamic analyses were conducted to optimize reaction conditions for CO_2 conversion to dimethyl ether and acetic acid. In chapters 4 and 5, galvanic replacement, as a synthesis method, was used to synthesize indium-based materials for CO_2 conversion to methanol and CO.

In chapter 2, a general conceptual framework, based on Gibbs free energy minimization, is used where the number of elements is considered rather than species to capture the equilibrium behavior of a mixture containing CO, CO_2, H_2, CH_3OH, DME, and H_2O. The equilibrium analysis was carried out at temperature-pressure combinations of $T\left({}^{o}C\right)\in\left\{100,200,300\right\}$ and $P\left(bar\right)\in\left\{10,40,80\right\}$, and the results were presented in C-H-O space. The maximum DME production of $F_{DME}^{(V)}$ = 0.069 occurred in the vapor phase at $\left(a_H,a_O,T,P\right)$= (0.435, 0.3, 200°C, 40 bar), where 52% of carbon and 94% of hydrogen atoms were consumed for DME production. At this operating condition, no DME separation is required from methanol as it was presented in a negligible amount in the product steam.

In Chapter 3, a similar approach as in chapter 2 was used to identify the optimal reaction condition for maximum production of acetic acid from CO_2. The phase equilibrium analysis was preformed for a mixture containing seven species: CO, CO_2, H_2, CH_3OH, H_2O, CH_3COOH, and $C_3H_6O_2$. The equilibrium analysis was carried out at temperature-pressure combinations of $T\left({}^{o}C\right)\in\left\{100,150,200,250\right\}$and $P\left(bar\right)\in\left\{10,30,50\right\}$. The maximum acetic acid production was

observed in the liquid phase near the edge of the attainable region at $\left(a_H, a_O, T, P\right)$= (0.55, 0.25, 100°C, 50 bar). At the maximum acetic acid production, acetic acid made ~98% of total product and ~99% of carbon is utilized for its production.

In Chapter 4, galvanic replacement was employed, for the first time, to synthesize different supported Pd-In alloy-based catalysts with varied Pd loadings to achieve distinct Pd surface structures: single atoms, small clusters, and extended ensembles. The successful synthesis of these alloys was confirmed via TEM/STEM, ICP, XRD, and XPS, while the specific configurations of the atoms within them were probed via EXAFS and DRIFTS of adsorbed CO. These catalysts exhibited unique catalytic behaviors for CO_2 hydrogenation to methanol where Pd promoted both the reaction rate and methanol selectivity in all cases, though its efficacy was highest when Pd was present in small clusters.

In chapter 5, two different Pd-alloy materials were synthesized via selective deposition of Pd atoms on Cu/In_2O_3, which was achieved by controlling the reduction step in the galvanic replacement synthesis method. These materials showed different reduction behavior and displayed different reactivities in CO_2 hydrogenation to methanol and reverse water gas shift (RWGS) reaction. Practically, Pd_1Cu_{100}/In_2O_3-LRT had a lower light-off temperature compared to Pd_1Cu_{100}/In_2O_3-HRT for RWGS reaction which suggested that Pd atoms are deposited on different host metal, forming different supported Pd alloys.

6.2 Future work recommendations

The findings outlined in this thesis provide different tools for utilizing CO_2 as a raw material for synthesizing value-added chemicals as a way for mitigating CO_2 emissions. Nevertheless, more work ought to be done in order to provide additional insights on how to maximize CO_2 utilization to desired products. Within this context, the following are a few

recommendations for further studies involving thermodynamic analysis and indium-based material.

6.2.1 Thermodynamic: future work recommendations

Since the thermodynamic analysis conducted in this thesis was preformed considering elements rather than species, future research efforts should focus on comparing the experimental data of different feedstock for the feed to the equilibrium calculated data for DME synthesis and acetic acid synthesis. For DME synthesis, it is recommended to expand the thermodynamic analysis to include coke formation as it is one of the possible by-products especially at temperatures higher than 300°C, and to investigate its affect on product distribution [90]. Also, it is of a great interest to investigate the effect of intermediate species condensation on CO_2 conversion and DME selectivity. Similarly, for acetic acid synthesis, thermodynamic analysis could be expanded to include other species such as methane, ethanol, and ethyl acetate and to study their effects on product selectivities, in particular acetic acid selectivity [192,193].

6.2.2 Indium-based Catalysts: future work recommendations

The synthesis technique, galvanic replacement, employed in this thesis for PdIn alloys showed that different Pd cluster sizes had roughly similar selectivities toward methanol. To supplement that experimental study, DFT calculations could be performed to offer further understanding on the reasons behind the similar selectivities for metal in metal, PdIn alloy, catalysts compared to metal on metal, Pd/In_2O_3. Also, further optimization of cluster size (and cluster size uniformity) is desirable for better utilization of the precious metal, palladium. To further improve the catalytic activity of PdIn alloy catalysts, utilizing a more active support such as ZrO_2, is recommended rather than the more inert support, γ-Al_2O_3, that was examined in this thesis.

In addition to the ongoing efforts outlined in Chapter 5, it is recommended that more *in-situ* characterization be performed, in order to further support the hypothesis that was put forward and to investigate the undergoing transformation during reaction. Specifically, it is recommended that the catalysts be characterized by *in-situ* XPS to investigate if there is any shift in the binding energy of Pd, Cu, and In which might indicate Pd alloying with different host metals. Also, *in-situ* STEM is another technique that can be utilized to visualize the undergoing change in Pd deposition site, especially if Pd is indeed migrating from one host metal to another. Similarly, *in-situ* XRD could be utilized with a higher Pd loading catalyst to observe if a new peak develops at high temperatures, which might reveal an alloy formation by Pd migration between two metals.

Appendices

Appendix Chapter 2

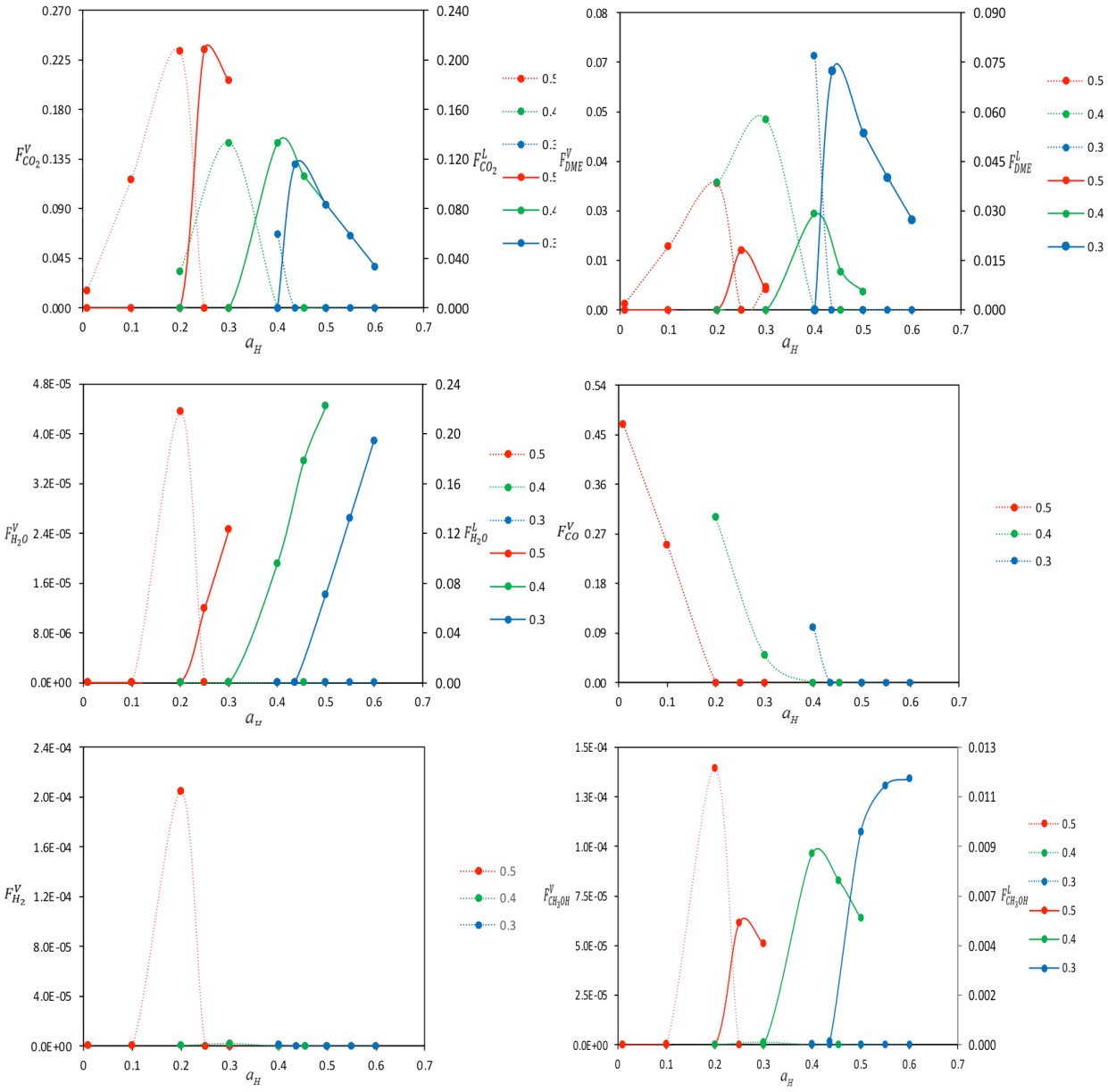

Figure A1: $F_j^{(V)}$(dash, left), $F_j^{(L)}$(solid, right) iso- a_O lines as a_H functions, T=100°C, P=80 bar

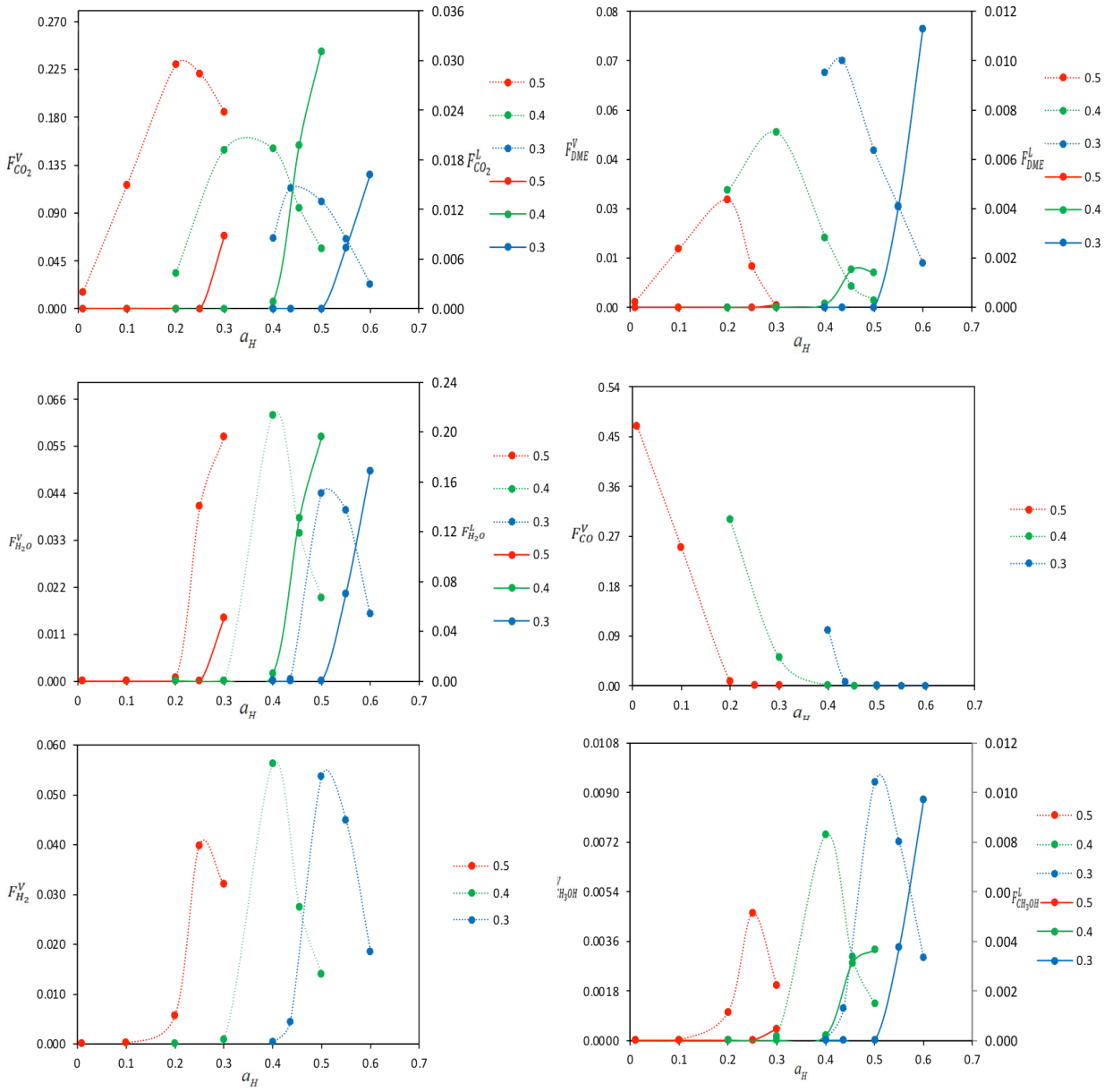

Figure A2: $F_j^{(V)}$(dash, left), $F_j^{(L)}$(solid, right) iso- a_O lines as a_H functions, T=200ºC, P=80 bar

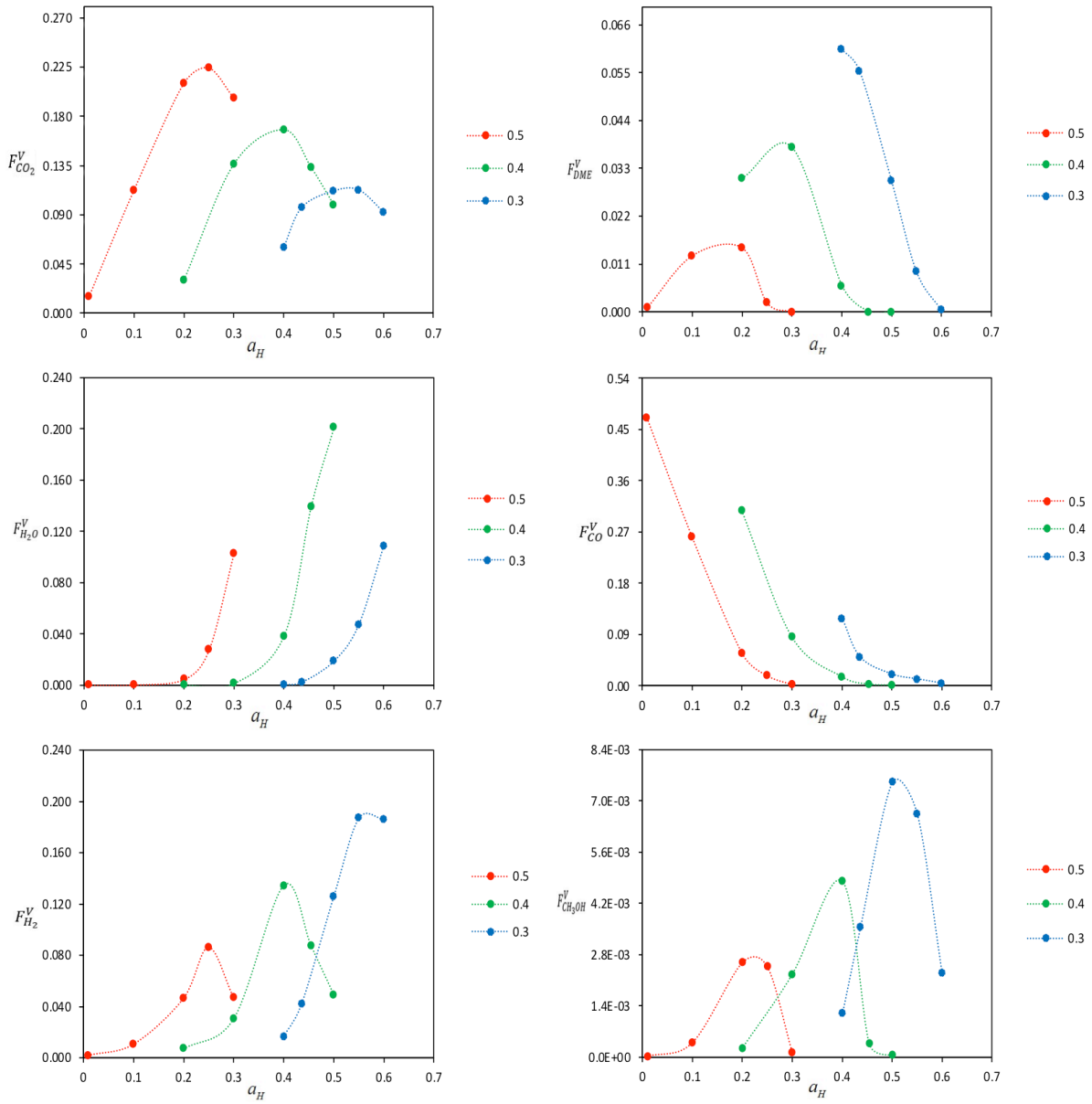

Figure A3: $F_j^{(V)}$(dash, left), $F_j^{(L)}$(solid, right) iso- a_O lines as a_H functions, T=300ºC, P=80 bar

Appendix Chapter 3

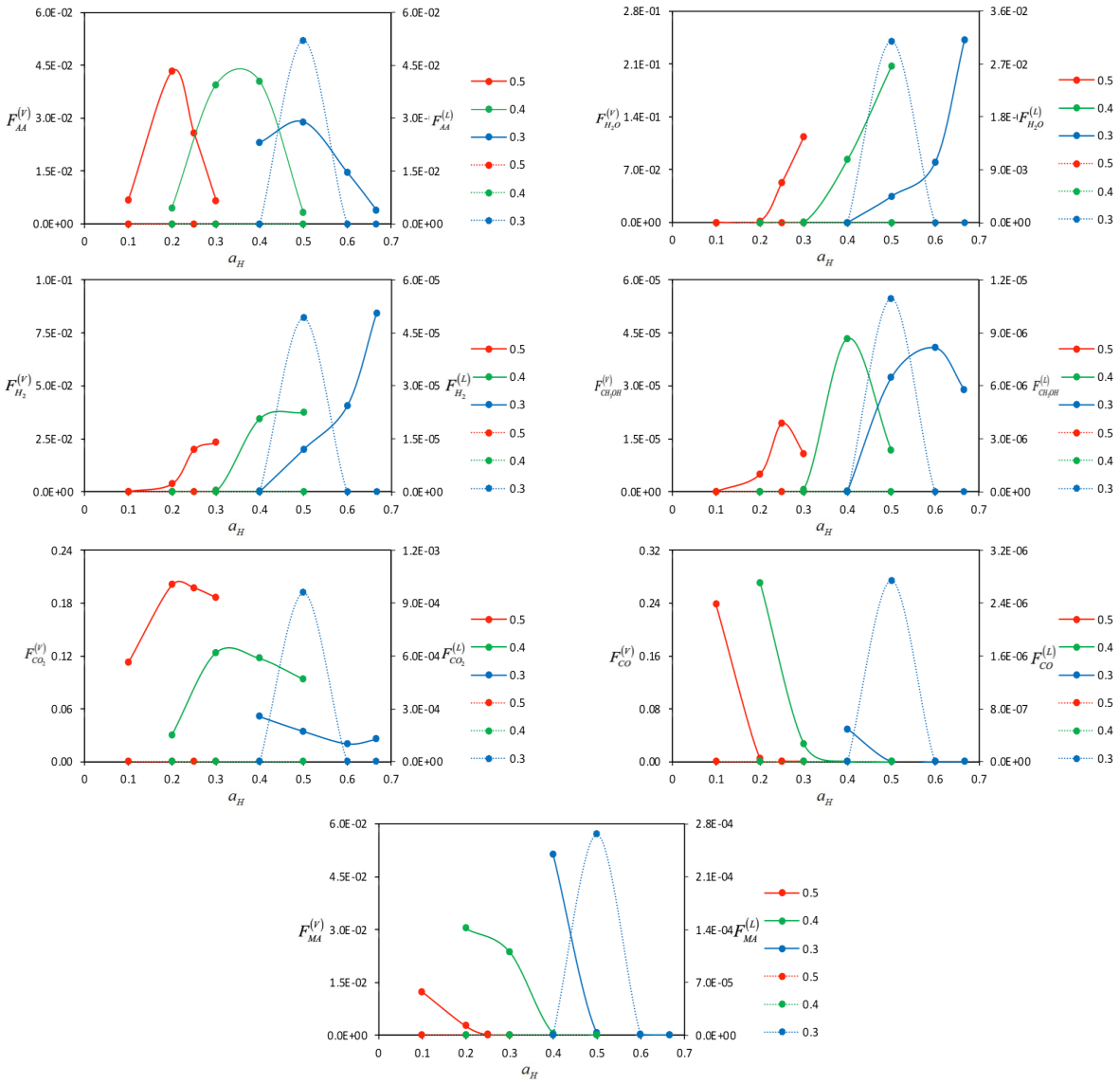

Figure A4: $F_j^{(V)}$(solid, left), $F_j^{(L)}$(dash, right) iso- a_O lines as a_H functions, T=250°C, P=50 bar

Appendix Chapter 4

Table A1: XAS spectra fitting

Catalyst	Treatment	XANES Energy (keV)	Scatter	CN	R, Å	$\Delta\sigma^2$ (x 10^3)	Eo (eV)
Pd Foil	Reference	24.3500	Pd-Pd	12	2.75	0.0	0.0
PdO	Reference	24.3531	Pd-O	4	2.05	0.0	0.0
Pd_1In_5	Fresh	24.3531	Pd-O	4.0	2.05	0.0	-0.3
Pd_1In_5	Used	24.3500	Pd-O	0.5	2.04	1.0	-1.4
			Pd-Pd(In)	5.7	2.77	4.0	-6.0
Pd_1In_{50}	Fresh	24.3531	Pd-O	4.0	2.05	0.0	-0.1
Pd_1In_{50}	Used	24.3506	Pd-O	1.5	2.06	1.0	-2.0
			Pd-Pd(In)	4.6	2.74	4.0	-6.7
Pd_1In_{50}	Reduction at 300°C	24.3495	Pd-Pd(In)	7.4	2.77	4.0	-4.3
Pd_1In_{50}	Rxn at 300°C	24.3502	Pd-O	0.8	2.02	1.0	-1.9
			Pd-Pd(In)	8.1	2.77	4.0	-4.0
Pd_1In_{100}	Fresh	24.3531	Pd-O	3.9	2.05	1.0	-0.4
Pd_1In_{100}	Used	24.3505	Pd-O	1.3	2.05	1.0	-2.1
			Pd-Pd(In)	5.6	2.78	4.0	-4.1

k^2 weighting, $\Delta k = 2.8 – 11.4$ Å^{-1} and $\Delta R = 1.0$-2.0 Å for PdO or $\Delta R = 1.3$-2.9 Å for used and reduced samples. CN is the coordination number. R is interatomic distance. σ^2 is Debye−Waller factor. E_0 is edge-energy shift.

Table A2: Product selectivities over different catalysts at 30 bar, H_2:CO_2=3:1, and GHSV=9000 h^{-1}.

Temperature (°C)	Product	Selectivity (C%)			
		In	**Pd_1In_{100}**	**Pd_1In_{50}**	**Pd_1In_5**
240	methanol	91.5	94.8	97.1	92.8
	carbon monoxide	0.0	0.0	0.0	2.7
	methane	8.5	5.2	1.8	1.1
	dimethyl ether	0.0	0.0	1.1	3.4
260	methanol	62.9	68.2	82.2	80.7
	carbon monoxide	28.7	20.1	10.6	11.8
	methane	7.8	7.7	4.7	2.5
	dimethyl ether	0.6	4.1	2.6	5.0
280	methanol	39.2	47.0	56.9	63.9
	carbon monoxide	51.5	37.5	29.5	23.2
	methane	8.8	11.9	9.9	6.1
	dimethyl ether	0.5	3.6	3.7	6.8
300	methanol	23.8	29.0	32.1	37.0
	carbon monoxide	65.3	53.3	48.6	49.1
	methane	10.5	15.1	16.1	8.7
	dimethyl ether	0.4	2.6	3.2	5.3

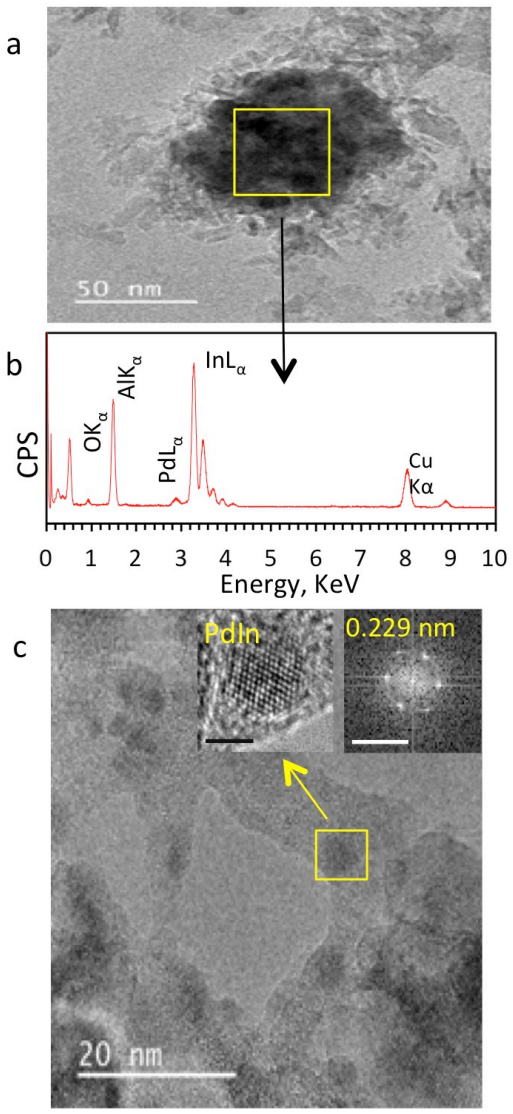

Figure A5: TEM images and EDS for Pd-In alloys. (a) TEM for fresh Pd_1In_5. **(b)** EDS data from selected area in a. **(c)** TEM for fresh Pd_1In_{50} and the insets are representing HRTEM of metal particle and FFT of the metal particle image.

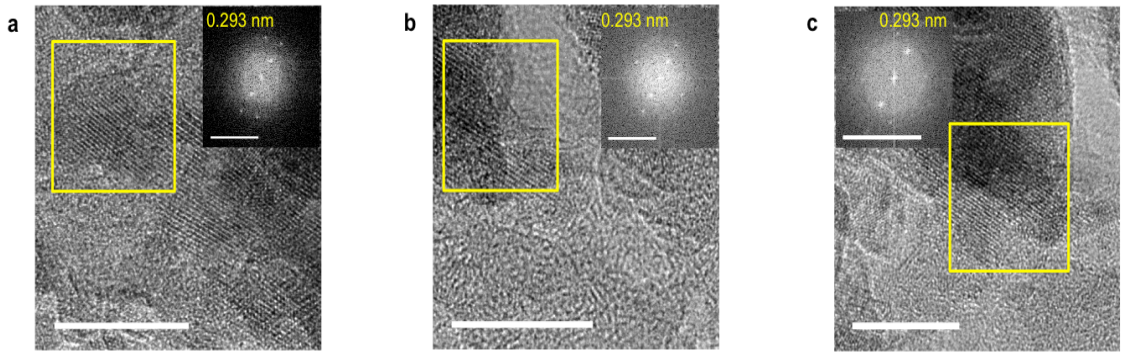

Figure A6: TEM images and their FFT. (a) Fresh Pd_1In_5 **(b)** Fresh Pd_1In_{50} **(c)** Fresh Pd_1In_{100}

The scale bar in all images is 10

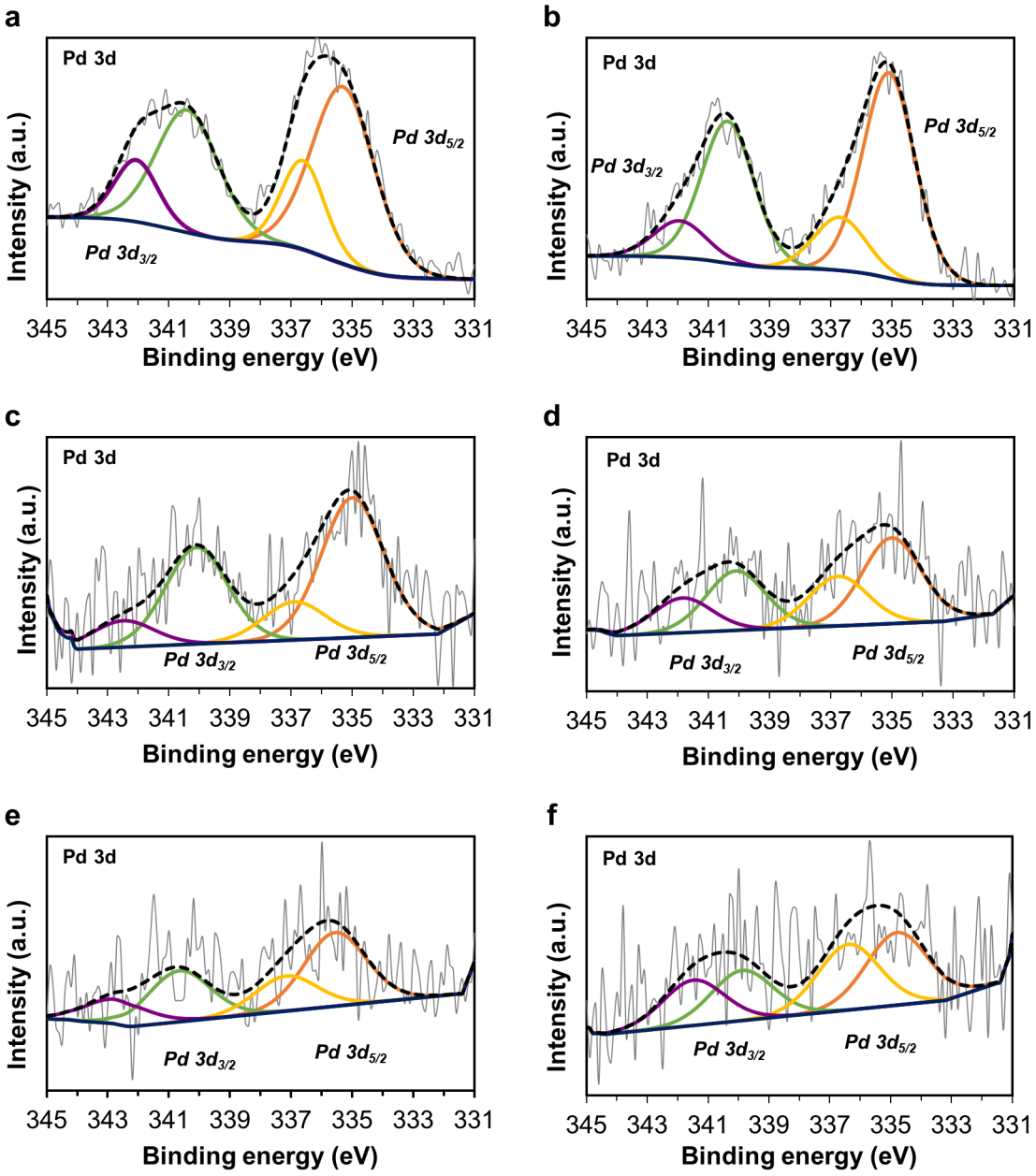

Figure A7: XPS Pd3d core-level spectra of investigated catalysts. **(a)** Fresh reduced Pd_1In_5 catalyst. **(b)** Spent Pd_1In_5 catalyst. **(c)** Fresh reduced Pd_1In_{50} catalyst. **(d)** Spent Pd_1In_{50} catalyst. **(e)** Fresh reduced Pd_1In_{100} catalyst. **(f)** Spent Pd_1In_{100} catalyst. Pd metal fitting peaks are marked with orange and green lines. PdO peak fitting are marked with yellow and purple lines. The sum of these fitted peaks is shown with a dashed black line. The fitted areas are only utilized to evaluate Pd:In ratios, not Pd oxidation state ratios. Quantitative interpretation of the Pd_1In_{100} data is limited by the low signal intensities measured.

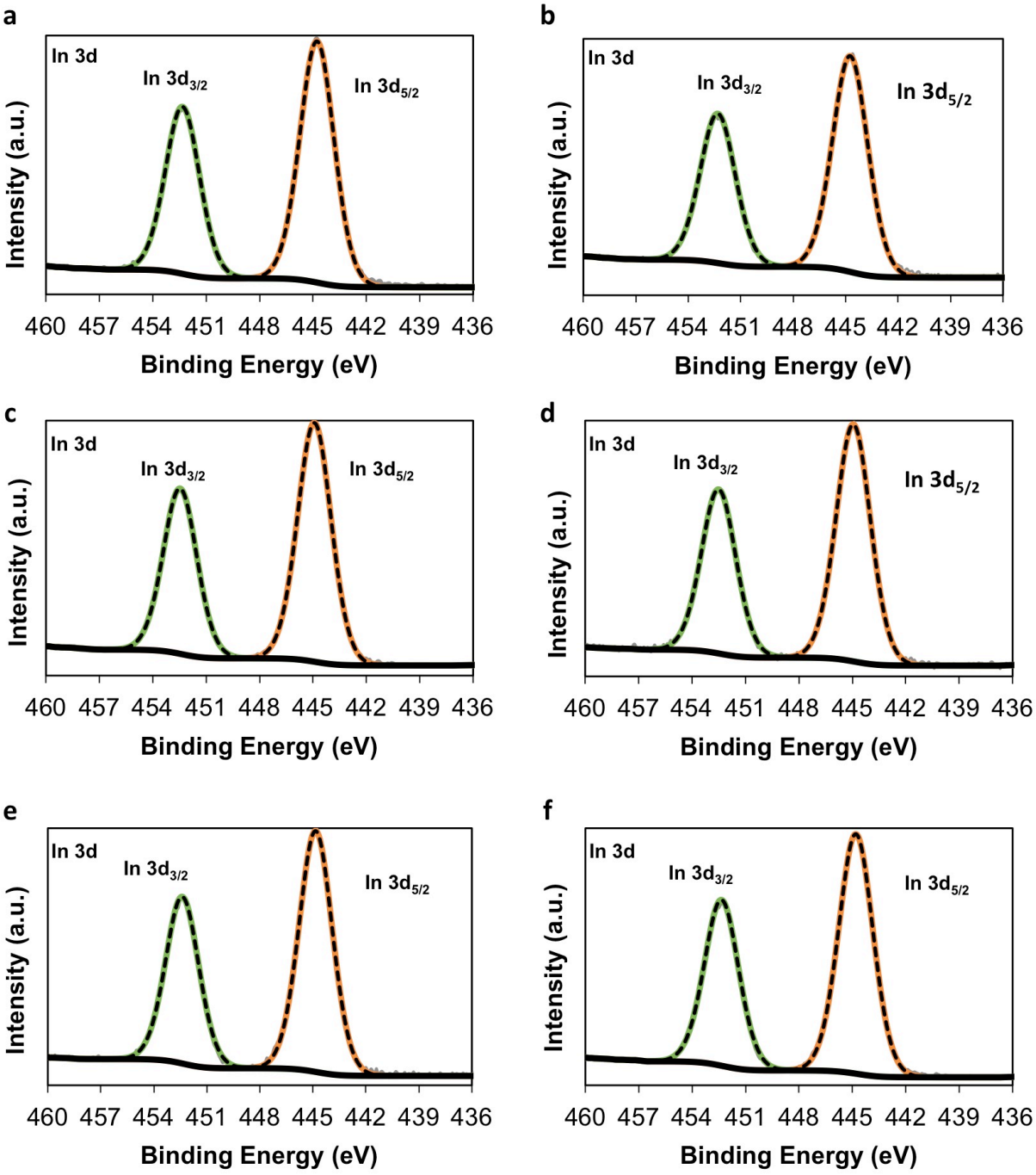

Figure A8: XPS In3d core-level spectra of investigated catalysts. (a) Fresh reduced Pd_1In_5 catalyst. **(b)** Spent Pd_1In_5 catalyst. **(c)** Fresh reduced Pd_1In_{50} catalyst. **(d)** Spent Pd_1In_{50} catalyst. **(e)** Fresh reduced Pd_1In_{100} catalyst. **(f)** Spent Pd_1In_{100} catalyst. The fitted areas are only utilized to evaluate Pd:In ratios, not In oxidation state ratios.

Appendix Chapter 5

Table A3: Product selectivities over Pd_1Cu_{100}/In_2O_3-HRT and Pd_1Cu_{100}/In_2O_3-LRT at 30 bar, H_2:CO_2=3:1, and GHSV=9000 h^{-1}.

Temperature (°C)	Product	Selectivity (C%)	
		Pd_1Cu_{100}/In_2O_3-LRT	**Pd_1Cu_{100}/In_2O_3-HRT**
240	methanol	89.6	96.9
	carbon monoxide	10.2	3.1
	methane	0.2	0
	dimethyl ether	0	0
260	methanol	69	83.1
	carbon monoxide	30.8	16.5
	methane	0.2	0.4
	dimethyl ether	0	0
280	methanol	46.5	68.2
	carbon monoxide	52.7	31
	methane	0.8	0.8
	dimethyl ether	0	0
300	methanol	23.1	48.4
	carbon monoxide	75.5	49.3
	methane	1.4	2.3
	dimethyl ether	0	0

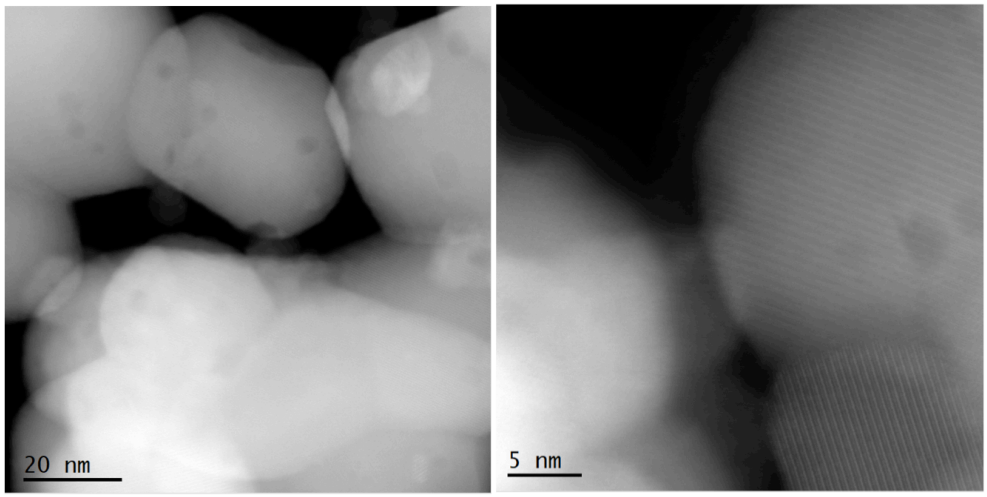

Figure A9: TEM images for Pd_1Cu_{100}/In_2O_3-HRT

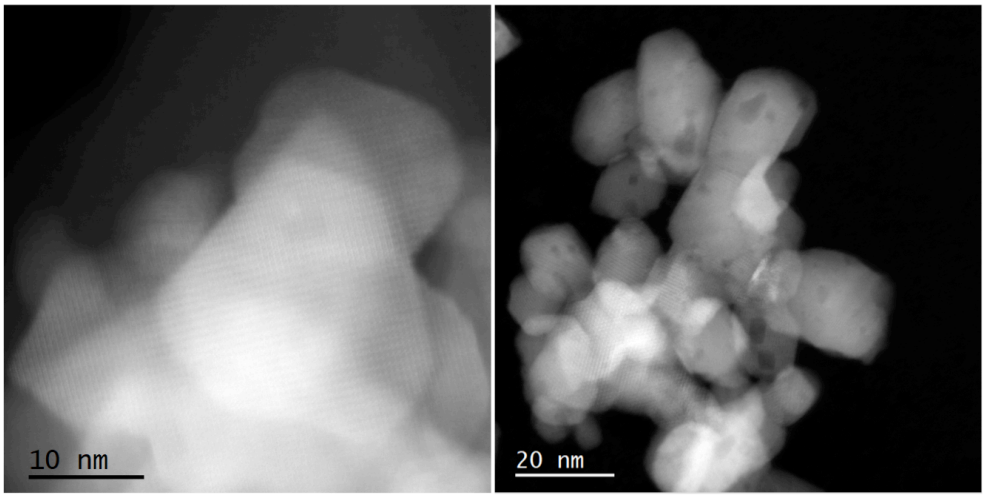

Figure A10: TEM images for Pd_1Cu_{100}/In_2O_3-LRT

Nomenclature

$\bar{a}_{\mathrm{i}}\left[\mathrm{i\,atom\text{-}mol}/s\right]$	*i*th atom-mol flow rate
$\bar{a}_{\mathrm{T}}\left[\mathrm{total\,atom\text{-}mol}/s\right]$	Total atom-mol flow rate
$a_{\mathrm{i}}\left[\mathrm{i\,atom\text{-}mol}/\mathrm{total\,atom\text{-}mol}\right]$	*i*th atom-mol fraction (*i*th atom-mol over total atom-mol present in system)
$a_{\mathrm{C}}\left[\mathrm{C\,atom\text{-}mol}/\mathrm{total\,atom\text{-}mol}\right]$	Carbon atom-mol fraction (carbon atom-mol over total atom-mol present in system)
$a_{\mathrm{H}}\left[\mathrm{H\,atom\text{-}mol}/\mathrm{total\,atom\text{-}mol}\right]$	Hydrogen atom-mol fraction (hydrogen atom-mol over total atom-mol present in system)
$a_{\mathrm{O}}\left[\mathrm{O\,atom\text{-}mol}/\mathrm{total\,atom\text{-}mol}\right]$	Oxygen atom-mol fraction (oxygen atom-mol over total atom-mol present in system)
$\hat{f}_j^{(k)}$ [bar]	Fugacity of species *j* in phase *k*
f_j^o [bar]	Standard fugacity of pure species *j* in its standard state at temperature *T*
$\hat{f}_j^V$ [bar]	Fugacity of species *j* in the vapor phase
$\hat{f}_j^L$ [bar]	Fugacity of species *j* in the liquid phase
$F_j^{(k)}\left[mol\ j/total\ atom-mol\right]$	Moles of species *j* per total atom-mol in phase *k* of the system
$F_j\left[mol\ j/total\ atom-mol\right]$	Moles of species *j* per total atom-mol of the system
$\bar{G}\left(T,P,\left\{n_p^{(k)}\right\}_{(p,k)=(1,1)}^{(NC,NP)}\right)\left[kJ/s\right]$	Total Gibbs free energy of the system
$G_j^o(T)\left[kJ/mol\ j\right]$	Molar Gibbs free energy of pure species *j* in its standard state at temperature *T*
$n_j^{(k)}\left[mol\ j/s\right]$	Molar flow rate of species *j* in phase *k*
P [bar]	Pressure
$P_j^{sat}(T)$ [bar]	Saturated vapor pressure of species *j*
$R\left[kJ/(mol\cdot K)\right]$	Universal Gas Constant
$T\left[K\right]$	Temperature
x_j	Mole fraction of species *j* in the liquid phase
y_j	Mole fraction of species *j* in the vapor phase
Greek letters	
$\mu_j^{(k)}\left[kJ/mol\right]$	Chemical potential of species *j* in phase *k*
$\nu_{i,j}\left[\dfrac{i\,atom-mol}{mol\ j}\right]$	Number of atoms of element *i* in species *j*
$\hat{\phi}_j\left(T,P,\left\{y_j\right\}_{j=1}^{NC}\right)$	Fugacity coefficient of species *j* in the vapor phase

$\gamma_j\left(T,\left\{x_j\right\}_{j=1}^{NC}\right)$	Activity coefficient of species *j* in the liquid phase
$\bar{\pi}\left(T,P,\left\{\bar{a}_i\right\}_{i=1}^{NE}\right)\left[kJ/s\right]$	Total Gibbs free energy optimum value
$\pi\left(T,P,\left\{a_i\right\}_{i=1}^{NE}\right)$	Total Gibbs free energy optimum value per total atom-mol
Ω	Feasible region for all mol per total atom-mol quantities in $\mathbb{R}^{NC}$
Abbreviations	
NC	Number of components
NE	Number of elements
NP	Number of phases

References

1. Adger, W. N., Barnett, J., Brown, K., Marshall, N. & O'Brien, K. Cultural dimensions of climate change impacts and adaptation. *Nat. Clim. Change* **3**, 112–117 (2013).
2. MacDowell, N. *et al.* An overview of CO_2 capture technologies. *Energy Environ. Sci.* **3**, 1645–1669 (2010).
3. Jiang, X., Nie, X., Guo, X., Song, C. & Chen, J. G. Recent Advances in Carbon Dioxide Hydrogenation to Methanol via Heterogeneous Catalysis. *Chem. Rev.* **120**, 7984–8034 (2020).
4. Artz, J. *et al.* Sustainable Conversion of Carbon Dioxide: An Integrated Review of Catalysis and Life Cycle Assessment. *Chem. Rev.* **118**, 434–504 (2018).
5. Metz, B., Davidson, O., Bosch, P., Dave, R. & Meyer, L. *Climate change 2007: mitigation of climate change*. (Cambridge Univ. Press, 2007).
6. Bergero, C., Rich, M. J. & Saikawa, E. All roads lead to Paris: The eight pathways to renewable energy target adoption. *Energy Res. Soc. Sci.* **80**, 102215 (2021).
7. Masson-Delmotte, V., Intergovernmental Panel on Climate Change, WMO, & United Nations Environment Programme. *Climate change and land: an IPCC special report on climate change, desertification, land degradation, sustainable land management, food security, and greenhouse gas fluxes in terrestrial ecosystems : summary for policymakers*. (Intergovernmental Panel on Climate Change, 2019).
8. US Department of Commerce, N. Global Monitoring Laboratory - Carbon Cycle Greenhouse Gases. https://gml.noaa.gov/ccgg/trends/.
9. Rogelj, J. *et al.* Paris Agreement climate proposals need a boost to keep warming well below 2 °C. *Nature* **534**, 631–639 (2016).

10. Piontek, F. M., Herrmann, C. & Saraev, A. Steps from Zero Carbon Supply Chains and Demand of Circular Economy to Circular Business Cases. *Eur. J. Soc. Impact Circ. Econ.* **2**, 1–9 (2021).
11. Cebrucean, D., Cebrucean, V. & Ionel, I. CO_2 Capture and Storage from Fossil Fuel Power Plants. *Energy Procedia* **63**, 18–26 (2014).
12. Quadrelli, E. A., Centi, G., Duplan, J.-L. & Perathoner, S. Carbon Dioxide Recycling: Emerging Large-Scale Technologies with Industrial Potential. *ChemSusChem* **4**, 1194–1215 (2011).
13. Herzog, H. & Golomb, D. Carbon Capture and Storage from Fossil Fuel Use. in *Encyclopedia of Energy* (ed. Cleveland, C. J.) 277–287 (Elsevier, 2004).
14. Zhang, Q. *et al.* Long carbon nanotubes intercrossed Cu/Zn/Al/Zr catalyst for CO/CO_2 hydrogenation to methanol/dimethyl ether. *Catal. Today* **150**, 55–60 (2010).
15. Yan, Y., Zeitler, E. L., Gu, J., Hu, Y. & Bocarsly, A. B. Electrochemistry of Aqueous Pyridinium: Exploration of a Key Aspect of Electrocatalytic Reduction of CO_2 to Methanol. *J. Am. Chem. Soc.* **135**, 14020–14023 (2013).
16. Yang, H. B. *et al.* Atomically dispersed Ni(i) as the active site for electrochemical CO_2 reduction. *Nat. Energy* **3**, 140–147 (2018).
17. V. Kondratenko, E., Mul, G., Baltrusaitis, J., O. Larrazábal, G. & Pérez-Ramírez, J. Status and perspectives of CO_2 conversion into fuels and chemicals by catalytic, photocatalytic and electrocatalytic processes. *Energy Environ. Sci.* **6**, 3112–3135 (2013).
18. Sen, R., Goeppert, A., Kar, S. & Prakash, G. K. S. Hydroxide Based Integrated CO_2 Capture from Air and Conversion to Methanol. *J. Am. Chem. Soc.* **142**, 4544–4549 (2020).

19. Genovese, C., Ampelli, C., Perathoner, S. & Centi, G. Mechanism of C–C bond formation in the electrocatalytic reduction of CO_2 to acetic acid. A challenging reaction to use renewable energy with chemistry. *Green Chem.* **19**, 2406–2415 (2017).
20. Pena Lopez, J. A., Somiari, I. & Manousiouthakis, V. I. Hydrogen/formic acid production from natural gas with zero carbon dioxide emissions. *J. Nat. Gas Sci. Eng.* **49**, 84–93 (2018).
21. Damiani, D., Litynski, J. T., McIlvried, H. G., Vikara, D. M. & Srivastava, R. D. The US department of Energy's R&D program to reduce greenhouse gas emissions through beneficial uses of carbon dioxide. *Greenh. Gases Sci. Technol.* **2**, 9–16 (2012).
22. Ahmad, K. & Upadhyayula, S. Greenhouse gas CO_2 hydrogenation to fuels: A thermodynamic analysis. *Environ. Prog. Sustain. Energy* **38**, 98–111 (2019).
23. Zangeneh, F. T., Taeb, A., Gholivand, K. & Sahebdelfar, S. Thermodynamic Equilibrium Analysis of Propane Dehydrogenation with Carbon Dioxide and Side Reactions. *Chem. Eng. Commun.* **203**, 557–565 (2016).
24. Cui, X. & Kær, S. K. Thermodynamic analysis of steam reforming and oxidative steam reforming of propane and butane for hydrogen production. *Int. J. Hydrog. Energy* **43**, 13009–13021 (2018).
25. Smith, W. R. & Missen, R. W. Strategies for solving the chemical equilibrium problem and an efficient microcomputer-based algorithm. *Can. J. Chem. Eng.* **66**, 591–598 (1988).
26. Gao, J. *et al.* A thermodynamic analysis of methanation reactions of carbon oxides for the production of synthetic natural gas. *RSC Adv.* **2**, 2358–2368 (2012).
27. Jia, C., Gao, J., Dai, Y., Zhang, J. & Yang, Y. The thermodynamics analysis and experimental validation for complicated systems in CO_2 hydrogenation process. *J. Energy Chem.* **25**, 1027–1037 (2016).

28. Chaconas, D., Pichardo, P., Manousiouthakis, I. V. & Manousiouthakis, V. I. Equilibrium analysis of CH_4, CO, CO_2, H_2O, H_2, C mixtures in C–H–O atom space using Gibbs free energy global minimization. *AIChE J.* **67**, e17052 (2021).
29. Piercy, R. & Hampson, N. A. The electrochemistry of indium. *J. Appl. Electrochem.* **5**, 1–15 (1975).
30. Korotcenkov, G., Brinzari, V. & Cho, B. K. In2O3-based multicomponent metal oxide films and their prospects for thermoelectric applications. *Solid State Sci.* **52**, 141–148 (2016).
31. Gopchandran, K. G., Joseph, B., Abraham, J. T., Koshy, P. & Vaidyan, V. K. The preparation of transparent electrically conducting indium oxide films by reactive vacuum evaporation. *Vacuum* **48**, 547–550 (1997).
32. Song, J.-O., Kwak, J. S., Park, Y. & Seong, T.-Y. Improvement of the light output of InGaN-based light-emitting diodes using Cu-doped indium oxide/indium tin oxide p-type electrodes. *Appl. Phys. Lett.* **86**, 213505 (2005).
33. Shigesato, Y., Takaki, S. & Haranoh, T. Electrical and structural properties of low resistivity tin‐doped indium oxide films. *J. Appl. Phys.* **71**, 3356–3364 (1992).
34. Li, C. *et al.* In_2O_3 nanowires as chemical sensors. *Appl. Phys. Lett.* **82**, 1613–1615 (2003).
35. Zhuang, Z., Peng, Q., Liu, J., Wang, X. & Li, Y. Indium Hydroxides, Oxyhydroxides, and Oxides Nanocrystals Series. *Inorg. Chem.* **46**, 5179–5187 (2007).
36. Zhou, B. *et al.* Controlled synthesis of rh-In_2O_3 nanostructures with different morphologies for efficient photocatalytic degradation of oxytetracycline. *Appl. Surf. Sci.* **464**, 115–124 (2019).

37. Babu, S. H., Kaleemulla, S., Rao, N. M. & Krishnamoorthi, C. Indium oxide: A transparent, conducting ferromagnetic semiconductor for spintronic applications. *J. Magn. Magn. Mater.* **416**, 66–74 (2016).

38. Umegaki, T. *et al.* Hydrogen production via steam reforming of ethyl alcohol over nano-structured indium oxide catalysts. *J. Power Sources* **179**, 566–570 (2008).

39. Lorenz, H. *et al.* Novel methanol steam reforming activity and selectivity of pure In_2O_3. *Appl. Catal. Gen.* **347**, 34–42 (2008).

40. Bielz, T., Lorenz, H., Amann, P., Klötzer, B. & Penner, S. Water−Gas Shift and Formaldehyde Reforming Activity Determined by Defect Chemistry of Polycrystalline In_2O_3. *J. Phys. Chem. C* **115**, 6622–6628 (2011).

41. Ye, J., Liu, C. & Ge, Q. DFT Study of CO_2 Adsorption and Hydrogenation on the In_2O_3 Surface. *J. Phys. Chem. C* **116**, 7817–7825 (2012).

42. Ye, J., Liu, C., Mei, D. & Ge, Q. Active Oxygen Vacancy Site for Methanol Synthesis from CO_2 Hydrogenation on In_2O_3(110): A DFT Study. *ACS Catal.* **3**, 1296–1306 (2013).

43. Sun, K. *et al.* Hydrogenation of CO_2 to methanol over In_2O_3 catalyst. *J. CO_2 Util.* **12**, 1–6 (2015).

44. Martin, O., Mart, A. J., Hauert, R., Drouilly, C. & Curulla-Ferr, D. Indium Oxide as a Superior Catalyst for Methanol Synthesis by CO_2 Hydrogenation. *Angew Chem Int Ed* 5 (2016).

45. Gao, P. *et al.* Direct Production of Lower Olefins from CO_2 Conversion via Bifunctional Catalysis. *ACS Catal.* **8**, 571–578 (2018).

46. Gao, P. *et al.* Direct conversion of CO_2 into liquid fuels with high selectivity over a bifunctional catalyst. *Nat. Chem.* **9**, 1019–1024 (2017).

47. Snider, J. L. *et al.* Revealing the Synergy between Oxide and Alloy Phases on the Performance of Bimetallic In–Pd Catalysts for CO $_2$ Hydrogenation to Methanol. *ACS Catal.* **9**, 3399–3412 (2019).

48. Frei, M. S. *et al.* Atomic-scale engineering of indium oxide promotion by palladium for methanol production via CO_2 hydrogenation. *Nat. Commun.* **10**, 3377 (2019).

49. Wang, J., Sun, K., Jia, X. & Liu, C. CO2 hydrogenation to methanol over Rh/In_2O_3 catalyst. *Catal. Today* **365**, 341–347 (2021).

50. Han, Z., Tang, C., Wang, J., Li, L. & Li, C. Atomically dispersed Ptn+ species as highly active sites in Pt/In_2O_3 catalysts for methanol synthesis from CO_2 hydrogenation. *J. Catal.* **394**, 236–244 (2021).

51. Rui, N. *et al.* Hydrogenation of CO_2 to Methanol on a $Au^{\delta+}$ –In_2O_{3-x} Catalyst. *ACS Catal.* **10**, 11307–11317 (2020).

52. Pachauri, R. K. *et al. Climate Change 2014: Synthesis Report. Contribution of Working Groups I, II and III to the Fifth Assessment Report of the Intergovernmental Panel on Climate Change*. *EPIC3Geneva, Switzerland, IPCC, 151 p., pp. 151, ISBN: 978-92-9169-143-2* 151 (IPCC, 2014).

53. Change, I. C. Mitigation of climate change. *Contrib. Work. Group III Fifth Assess. Rep. Intergov. Panel Clim. Change* **1454**, (2014).

54. Centi, G., Alessandra Quadrelli, E. & Perathoner, S. Catalysis for CO_2 conversion: a key technology for rapid introduction of renewable energy in the value chain of chemical industries. *Energy Environ. Sci.* **6**, 1711–1731 (2013).

55. Miguel, C. V., Soria, M. A., Mendes, A. & Madeira, L. M. Direct CO_2 hydrogenation to methane or methanol from post-combustion exhaust streams – A thermodynamic study. *J. Nat. Gas Sci. Eng.* **22**, 1–8 (2015).

56. Garbarino, G. *et al.* A study of Ni/La-Al_2O_3 catalysts: A competitive system for CO_2 methanation. *Appl. Catal. B Environ.* **248**, 286–297 (2019).

57. Zachopoulos, A. & Heracleous, E. Overcoming the equilibrium barriers of CO_2 hydrogenation to methanol via water sorption: A thermodynamic analysis. *J. CO_2 Util.* **21**, 360–367 (2017).

58. Álvarez, A. *et al.* Challenges in the Greener Production of Formates/Formic Acid, Methanol, and DME by Heterogeneously Catalyzed CO_2 Hydrogenation Processes. *Chem. Rev.* **117**, 9804–9838 (2017).

59. Park, S. H. & Lee, C. S. Applicability of dimethyl ether (DME) in a compression ignition engine as an alternative fuel. *Energy Convers. Manag.* **86**, 848–863 (2014).

60. Chen, W.-H., Lin, B.-J., Lee, H.-M. & Huang, M.-H. One-step synthesis of dimethyl ether from the gas mixture containing CO_2 with high space velocity. *Appl. Energy* **98**, 92–101 (2012).

61. Migliori, M., Aloise, A., Catizzone, E. & Giordano, G. Kinetic Analysis of Methanol to Dimethyl Ether Reaction over H-MFI Catalyst. *Ind. Eng. Chem. Res.* **53**, 14885–14891 (2014).

62. Ereña, J. *et al.* Kinetic modelling of dimethyl ether synthesis from (H_2+CO_2) by considering catalyst deactivation. *Chem. Eng. J.* **174**, 660–667 (2011).

63. Azizi, Z., Rezaeimanesh, M., Tohidian, T. & Rahimpour, M. R. Dimethyl ether: A review of technologies and production challenges. *Chem. Eng. Process. Process Intensif.* **82**, 150–172 (2014).

64. Ogawa, T., Inoue, N., Shikada, T. & Ohno, Y. Direct dimethyl ether synthesis. *J. Nat. Gas Chem.* **12**, 219–227 (2003).

65. Sai Prasad, P. S., Bae, J. W., Kang, S.-H., Lee, Y.-J. & Jun, K.-W. Single-step synthesis of DME from syngas on Cu–ZnO–Al_2O_3/zeolite bifunctional catalysts: The superiority of ferrierite over the other zeolites. *Fuel Process. Technol.* **89**, 1281–1286 (2008).

66. Bonura, G. *et al.* Catalytic behaviour of a bifunctional system for the one step synthesis of DME by CO_2 hydrogenation. *Catal. Today* **228**, 51–57 (2014).

67. Bae, J. W., Kang, S.-H., Lee, Y.-J. & Jun, K.-W. Synthesis of DME from syngas on the bifunctional Cu–ZnO–Al_2O_3/Zr-modified ferrierite: Effect of Zr content. *Appl. Catal. B Environ.* **90**, 426–435 (2009).

68. Chen, W.-H., Hsu, C.-L. & Wang, X.-D. Thermodynamic approach and comparison of two-step and single step DME (dimethyl ether) syntheses with carbon dioxide utilization. *Energy* **109**, 326–340 (2016).

69. Shen, W.-J., Jun, K.-W., Choi, H.-S. & Lee, K.-W. Thermodynamic investigation of methanol and dimethyl ether synthesis from CO_2 Hydrogenation. *Korean J. Chem. Eng.* **17**, 210–216 (2000).

70. Stangeland, K., Li, H. & Yu, Z. Thermodynamic Analysis of Chemical and Phase Equilibria in CO_2 Hydrogenation to Methanol, Dimethyl Ether, and Higher Alcohols. *Ind. Eng. Chem. Res.* **57**, 4081–4094 (2018).

71. Gavalas, G. R. *Nonlinear Differential Equations of Chemically Reacting Systems*. (Springer Science & Business Media, 2013).

72. Horn, F. Attainable and non-attainable regions in chemical reaction technique. in *Third European symposium on chemical reaction engineering* 1–10 (Pergamon Press London, 1964).

73. Glasser, D., Crowe, C. & Hildebrandt, D. A geometric approach to steady flow reactors: the attainable region and optimization in concentration space. *Ind. Eng. Chem. Res.* **26**, 1803–1810 (1987).

74. Hildebrandt, D., Glasser, D. & Crowe, C. M. Geometry of the attainable region generated by reaction and mixing: with and without constraints. *Ind. Eng. Chem. Res.* **29**, 49–58 (1990).

75. Nisoli, A., Malone, M. F. & Doherty, M. F. Attainable regions for reaction with separation. *AIChE J.* **43**, 374–387 (1997).

76. Feinberg, M. & Hildebrandt, D. Optimal reactor design from a geometric viewpoint—I. Universal properties of the attainable region. *Chem. Eng. Sci.* **52**, 1637–1665 (1997).

77. Conner, J. A. & Manousiouthakis, V. I. On the attainable region for process networks. *AIChE J.* **60**, 193–212 (2014).

78. Zhou, W. & Manousiouthakis, V. I. Non-ideal reactor network synthesis through IDEAS: Attainable region construction. *Chem. Eng. Sci.* **61**, 6936–6945 (2006).

79. Zhou, W. & Manousiouthakis, V. I. On dimensionality of attainable region construction for isothermal reactor networks. *Comput. Chem. Eng.* **32**, 439–450 (2008).

80. Burri, J. F., Wilson, S. D. & Manousiouthakis, V. I. Infinite DimEnsionAl State-space approach to reactor network synthesis: application to attainable region construction. *Comput. Chem. Eng.* **26**, 849–862 (2002).

81. Manousiouthakis, V. I., Justanieah, A. M. & Taylor, L. A. The Shrink–Wrap algorithm for the construction of the attainable region: an application of the IDEAS framework. *Comput. Chem. Eng.* **28**, 1563–1575 (2004).

82. Paepae, T. & Seodigeng, T. Thermodynamic Attainable Region for Direct Synthesis of Dimethyl Ether from Synthesis Gas. *Int. J. Chem. Mol. Eng.* **10**, 784–790 (2016).

83. *IUPAC Compendium of Chemical Terminology: The Gold Book*. (International Union of Pure and Applied Chemistry, 2006).

84. García-Trenco, A. & Martínez, A. Direct synthesis of DME from syngas on hybrid CuZnAl/ZSM-5 catalysts: New insights into the role of zeolite acidity. *Appl. Catal. Gen.* **411–412**, 170–179 (2012).

85. Michelsen, M. L. The isothermal flash problem. Part II. Phase-split calculation. *Fluid Phase Equilibria* **9**, 21–40 (1982).

86. Michelsen, M. L. The isothermal flash problem. Part I. Stability. *Fluid Phase Equilibria* **9**, 1–19 (1982).

87. Ereña, J., Garoña, R., Arandes, J. M., Aguayo, A. T. & Bilbao, J. Effect of operating conditions on the synthesis of dimethyl ether over a CuO-ZnO-Al_2O_3/NaHZSM-5 bifunctional catalyst. *Catal. Today* **107–108**, 467–473 (2005).

88. Asthana, S., Samanta, C., Voolapalli, R. K. & Saha, B. Direct conversion of syngas to DME: synthesis of new Cu-based hybrid catalysts using Fehling's solution, elimination of the calcination step. *J. Mater. Chem. A* **5**, 2649–2663 (2017).

89. Rodriguez-Vega, P. *et al.* Experimental implementation of a catalytic membrane reactor for the direct synthesis of DME from H_2+CO/CO_2. *Chem. Eng. Sci.* **234**, 116396 (2021).

90. Sierra, I., Ereña, J., Aguayo, A. T., Olazar, M. & Bilbao, J. Deactivation Kinetics for Direct Dimethyl Ether Synthesis on a CuO−ZnO−Al_2O_3/γ-Al_2O_3 Catalyst. *Ind. Eng. Chem. Res.* **49**, 481–489 (2010).

91. Sierra, I. *et al.* Co-feeding water to attenuate deactivation of the catalyst metallic function (CuO–ZnO–Al_2O_3) by coke in the direct synthesis of dimethyl ether. *Appl. Catal. B Environ.* **106**, 167–173 (2011).

92. Pichardo, P. & Manousiouthakis, V. I. Infinite DimEnsionAl State-space as a systematic process intensification tool: Energetic intensification of hydrogen production. *Chem. Eng. Res. Des.* **120**, 372–395 (2017).

93. Bennekom, J. G. van, Winkelman, J. G. M., Venderbosch, R. H., Nieland, S. D. G. B. & Heeres, H. J. Modeling and Experimental Studies on Phase and Chemical Equilibria in High-Pressure Methanol Synthesis. *Ind. Eng. Chem. Res.* **51**, 12233–12243 (2012).

94. Tu, C., Nie, X. & Chen, J. G. Insight into Acetic Acid Synthesis from the Reaction of CH_4 and CO_2. *ACS Catal.* **11**, 3384–3401 (2021).

95. Budiman, A. W. *et al.* Review of Acetic Acid Synthesis from Various Feedstocks Through Different Catalytic Processes. *Catal. Surv. Asia* **20**, 173–193 (2016).

96. Kalck, P., Le Berre, C. & Serp, P. Recent advances in the methanol carbonylation reaction into acetic acid. *Coord. Chem. Rev.* **402**, 213078 (2020).

97. Pacheco, K. A., Bresciani, A. E., Nascimento, C. A. O. & Alves, R. M. B. CO_2-based Acetic Acid Production Assessment. in *Computer Aided Chemical Engineering* vol. 48 1027–1032 (Elsevier, 2020).

98. Somiari, I. & Manousiouthakis, V. Coproduction of acetic acid and hydrogen/power from natural gas with zero carbon dioxide emissions. *AIChE J.* **64**, 860–876 (2018).

99. Sano, K., Uchida, H. & Wakabayashi, S. A new process for acetic acid production by direct oxidation of ethylene. *Catal. Surv. Asia* **3**, 55–60 (1999).

100. Nam, J. S. *et al.* Novel heterogeneous Rh-incorporated graphitic-carbon nitride for liquid-phase carbonylation of methanol to acetic acid. *Catal. Commun.* **99**, 141–145 (2017).

101. Xu, B., Madix, R. J. & Friend, C. M. Activated Metallic Gold as an Agent for Direct Methoxycarbonylation. *J. Am. Chem. Soc.* **133**, 20378–20383 (2011).

102. Shan, J., Li, M., Allard, L. F., Lee, S. & Flytzani-Stephanopoulos, M. Mild oxidation of methane to methanol or acetic acid on supported isolated rhodium catalysts. *Nature* **551**, 605–608 (2017).

103. Xiang, N., Xu, P., Ran, N. & Ye, T. Production of acetic acid from ethanol over CuCr catalysts via dehydrogenation-(aldehyde–water shift) reaction. *RSC Adv.* **7**, 38586–38593 (2017).

104. Onopchenko, A. & Schulz, J. G. D. Oxidation of butane with cobalt salts and oxygen via electron transfer. *J. Org. Chem.* **38**, 909–912 (1973).

105. Yoneda, N., Kusano, S., Yasui, M., Pujado, P. & Wilcher, S. Recent advances in processes and catalysts for the production of acetic acid. *Appl. Catal. Gen.* **221**, 253–265 (2001).

106. Christensen, C. H. *et al.* Formation of Acetic Acid by Aqueous-Phase Oxidation of Ethanol with Air in the Presence of a Heterogeneous Gold Catalyst. *Angew. Chem. Int. Ed.* **45**, 4648–4651 (2006).

107. Tessier, L., Bordes, E. & Gubelmann-Bonneau, M. Active specie on vanadium-containing catalysts for the selective oxidation of ethane to acetic acid. *Catal. Today* **24**, 335–340 (1995).

108. Dimian, A. C. & Kiss, A. A. Novel energy efficient process for acetic acid production by methanol carbonylation. *Chem. Eng. Res. Des.* **159**, 1–12 (2020).

109. Thomas, C. M. & Süss-Fink, G. Ligand effects in the rhodium-catalyzed carbonylation of methanol. *Coord. Chem. Rev.* **243**, 125–142 (2003).

110. Dekleva, T. W. & Forster, D. Mechanistic Aspects of Transition-Metal-Catalyzed Alcohol Carbonylations. in *Advances in Catalysis* (eds. Eley, D. D., Pines, H. & Weisz, P. B.) vol. 34 81–130 (Academic Press, 1986).

111. Sunley, G. J. & Watson, D. J. High productivity methanol carbonylation catalysis using iridium: The Cativa^{TM} process for the manufacture of acetic acid. *Catal. Today* **58**, 293–307 (2000).

112. Jia, C., Gao, J., Dai, Y., Zhang, J. & Yang, Y. The thermodynamics analysis and experimental validation for complicated systems in CO_2 hydrogenation process. *J. Energy Chem.* **25**, 1027–1037 (2016).

113. De, R. *et al.* Electrocatalytic Reduction of CO_2 to Acetic Acid by a Molecular Manganese Corrole Complex. *Angew. Chem.* **132**, 10614–10621 (2020).

114. Shavi, R., Ko, J., Cho, A., Han, J. W. & Seo, J. G. Mechanistic insight into the quantitative synthesis of acetic acid by direct conversion of CH_4 and CO_2: An experimental and theoretical approach. *Appl. Catal. B Environ.* **229**, 237–248 (2018).

115. He, C., Tian, G., Liu, Z. & Feng, S. A Mild Hydrothermal Route to Fix Carbon Dioxide to Simple Carboxylic Acids. *Org. Lett.* **12**, 649–651 (2010).

116. Wilcox, E. M., Roberts, G. W. & Spivey, J. J. Direct catalytic formation of acetic acid from CO_2 and methane. *Catal. Today* **88**, 83–90 (2003).

117. Qian, Q., Zhang, J., Cui, M. & Han, B. Synthesis of acetic acid via methanol hydrocarboxylation with CO_2 and H_2. *Nat. Commun.* **7**, 11481 (2016).

118. Lee, E. J. & Kim, Y. H. Energy saving in acetic acid process using an azeotropic distillation column with a side stripper. *Chem. Eng. Commun.* **205**, 1311–1322 (2018).

119. Servel, C., Roizard, D., Favre, E. & Horbez, D. Improved Energy Efficiency of a Hybrid Pervaporation/Distillation Process for Acetic Acid Production: Identification of Target Membrane Performances by Simulation. *Ind. Eng. Chem. Res.* **53**, 7768–7779 (2014).

120. Feyzi, V. & Beheshti, M. Exergy analysis and optimization of reactive distillation column in acetic acid production process. *Chem. Eng. Process. - Process Intensif.* **120**, 161–172 (2017).

121. Monastersky, R. Global carbon dioxide levels near worrisome milestone. *Nat. News* **497**, 13 (2013).

122. Wang, W., Wang, S., Ma, X. & Gong, J. Recent advances in catalytic hydrogenation of carbon dioxide. *Chem. Soc. Rev.* **40**, 3703 (2011).

123. Waters, T., O'Hair, R. A. J. & Wedd, A. G. Catalytic Gas Phase Oxidation of Methanol to Formaldehyde. *J. Am. Chem. Soc.* **125**, 3384–3396 (2003).

124. Xu, M., Lunsford, J. H., Goodman, D. W. & Bhattacharyya, A. Synthesis of dimethyl ether (DME) from methanol over solid-acid catalysts. *Appl. Catal. Gen.* **149**, 289–301 (1997).

125. Olah, G. A. Beyond Oil and Gas: The Methanol Economy. *Angew. Chem. Int. Ed.* **44**, 2636–2639 (2005).

126. Behrens, M. *et al.* The Active Site of Methanol Synthesis over $Cu/ZnO/Al_2O_3$ Industrial Catalysts. *Science* **336**, 893–897 (2012).

127. Fichtl, M. B. *et al.* Kinetics of deactivation on $Cu/ZnO/Al_2O_3$ methanol synthesis catalysts. *Appl. Catal. Gen.* **502**, 262–270 (2015).

128. Rui, N. *et al.* CO_2 hydrogenation to methanol over Pd/In_2O_3: effects of Pd and oxygen vacancy. *Appl. Catal. B Environ.* **218**, 488–497 (2017).

129. Sun, K. *et al.* A highly active Pt/In_2O_3 catalyst for CO_2 hydrogenation to methanol with enhanced stability. *Green Chem.* **22**, 5059–5066 (2020).

130. Therrien, A. J. *et al.* An atomic-scale view of single-site Pt catalysis for low-temperature CO oxidation. *Nat. Catal.* **1**, 192–198 (2018).

131. Wang, H. *et al.* Surpassing the single-atom catalytic activity limit through paired Pt-O-Pt ensemble built from isolated Pt1 atoms. *Nat. Commun.* **10**, 3808 (2019).

132. Zhang, X. *et al.* Platinum–copper single atom alloy catalysts with high performance towards glycerol hydrogenolysis. *Nat. Commun.* **10**, 5812 (2019).

133. Marcinkowski, M. D. *et al.* Pt/Cu single-atom alloys as coke-resistant catalysts for efficient C–H activation. *Nat. Chem.* **10**, 325–332 (2018).

134. Jeong, H. *et al.* Fully Dispersed Rh Ensemble Catalyst To Enhance Low-Temperature Activity. *J. Am. Chem. Soc.* **140**, 9558–9565 (2018).

135. Lucci, F. R. *et al.* Selective hydrogenation of 1,3-butadiene on platinum–copper alloys at the single-atom limit. *Nat. Commun.* **6**, 8550 (2015).

136. Boucher, M. B. *et al.* Single atom alloy surface analogs in $Pd_{0.18}Cu_{15}$ nanoparticles for selective hydrogenation reactions. *Phys. Chem. Chem. Phys.* **15**, 12187–12196 (2013).

137. Miyazaki, M., Furukawa, S., Takayama, T., Yamazoe, S. & Komatsu, T. Surface Modification of PdZn Nanoparticles via Galvanic Replacement for the Selective Hydrogenation of Terminal Alkynes. *ACS Appl. Nano Mater.* **2**, 3307–3314 (2019).

138. Xia, X., Wang, Y., Ruditskiy, A. & Xia, Y. 25th Anniversary Article: Galvanic Replacement: A Simple and Versatile Route to Hollow Nanostructures with Tunable and Well-Controlled Properties. *Adv. Mater.* **25**, 6313–6333 (2013).

139. Lu, X., Chen, J., Skrabalak, S. E. & Xia, Y. Galvanic replacement reaction: A simple and powerful route to hollow and porous metal nanostructures. *Proc. Inst. Mech. Eng. Part N J. Nanoeng. Nanosyst.* **221**, 1–16 (2007).

140. Men, Y., Kolb, G., Zapf, R., O'Connell, M. & Ziogas, A. Methanol steam reforming over bimetallic Pd–In/Al2O3 catalysts in a microstructured reactor. *Appl. Catal. Gen.* **380**, 15–20 (2010).

141. Cao, Y., Sui, Z., Zhu, Y., Zhou, X. & Chen, D. Selective Hydrogenation of Acetylene over Pd-In/Al_2O_3 Catalyst: Promotional Effect of Indium and Composition-Dependent Performance. *ACS Catal.* **7**, 7835–7846 (2017).

142. Li, C. *et al.* Ni–In Intermetallic Nanocrystals as Efficient Catalysts toward Unsaturated Aldehydes Hydrogenation. *Chem. Mater.* **25**, 3888–3896 (2013).

143. Li, C. *et al.* Nickel-Gallium Intermetallic Nanocrystal Catalysts in the Semihydrogenation of Phenylacetylene. *ChemCatChem* **6**, 824–831 (2014).

144. Feng, Q. *et al.* Isolated Single-Atom Pd Sites in Intermetallic Nanostructures: High Catalytic Selectivity for Semihydrogenation of Alkynes. *J. Am. Chem. Soc.* **139**, 7294–7301 (2017).

145. Fang, Y.-L. *et al.* Structural analysis of palladium-decorated gold nanoparticles as colloidal bimetallic catalysts. *Catal. Today* **160**, 96–102 (2011).

146. Zhao, Z., Miller, J. T., Wu, T., Schweitzer, N. M. & Wong, M. S. EXAFS Characterization of Palladium-on-Gold Catalysts Before and After Glycerol Oxidation. *Top. Catal.* **58**, 302–313 (2015).

147. Miller, J. T. *et al.* The effect of gold particle size on AuAu bond length and reactivity toward oxygen in supported catalysts. *J. Catal.* **240**, 222–234 (2006).

148. Darby, M. T., Sykes, E. C. H., Michaelides, A. & Stamatakis, M. Carbon Monoxide Poisoning Resistance and Structural Stability of Single Atom Alloys. *Top. Catal.* **61**, 428–438 (2018).

149. Abbet, S. *et al.* Identification of Defect Sites on MgO(100) Thin Films by Decoration with Pd Atoms and Studying CO Adsorption Properties. *J. Am. Chem. Soc.* **123**, 6172–6178 (2001).

150. Liu, J. *et al.* Palladium–gold single atom alloy catalysts for liquid phase selective hydrogenation of 1-hexyne. *Catal. Sci. Technol.* **7**, 4276–4284 (2017).

151. Luneau, M. *et al.* Dilute Pd/Au Alloy Nanoparticles Embedded in Colloid-Templated Porous SiO_2 : Stable Au-Based Oxidation Catalysts. *Chem. Mater.* **31**, 5759–5768 (2019).

152. Jeon, J., Kon, K., Toyao, T., Shimizu, K. & Furukawa, S. Design of Pd-based pseudo-binary alloy catalysts for highly active and selective NO reduction. *Chem. Sci.* **10**, 4148–4162 (2019).

153. Wu, Z. *et al.* Pd–In intermetallic alloy nanoparticles: highly selective ethane dehydrogenation catalysts. *Catal. Sci. Technol.* **6**, 6965–6976 (2016).

154. Markov, P. V. *et al.* $PdIn/Al_2O_3$ Intermetallic Catalyst: Structure and Catalytic Characteristics in Selective Hydrogenation of Acetylene. *Kinet. Catal.* **60**, 842–850 (2019).

155. Markov, P. V. *et al.* Intermetallic Pd In /Al_2O_3 catalysts with isolated single-atom Pd sites for one-pot hydrogenation of diphenylacetylene into trans-stilbene. *Mendeleev Commun.* **30**, 468–471 (2020).

156. Ouyang, M. *et al.* Directing reaction pathways via in situ control of active site geometries in PdAu single-atom alloy catalysts. *Nat. Commun.* **12**, 1549 (2021).

157. Zorn, K. *et al.* CO Oxidation on Technological Pd−Al_2O_3 Catalysts: Oxidation State and Activity. *J. Phys. Chem. C* **115**, 1103–1111 (2011).

158. Ye, J., Liu, C., Mei, D. & Ge, Q. Methanol synthesis from CO_2 hydrogenation over a Pd_4/In_2O_3 model catalyst: A combined DFT and kinetic study. *J. Catal.* **317**, 44–53 (2014).

159. Hammer, B. & Norskov, J. K. Why gold is the noblest of all the metals. *Nature* **376**, 238–240 (1995).

160. Lucci, F. R. *et al.* Controlling Hydrogen Activation, Spillover, and Desorption with Pd–Au Single-Atom Alloys. *J. Phys. Chem. Lett.* **7**, 480–485 (2016).

161. Tierney, H. L., Baber, A. E., Kitchin, J. R. & Sykes, E. C. H. Hydrogen Dissociation and Spillover on Individual Isolated Palladium Atoms. *Phys. Rev. Lett.* **103**, 246102 (2009).

162. van der Hoeven, J. E. S. *et al.* Entropic Control of HD Exchange Rates over Dilute Pd-in-Au Alloy Nanoparticle Catalysts. *ACS Catal.* **11**, 6971–6981 (2021).

163. Hartwig, C. *et al.* Isolated Pd atoms in a silver matrix: Spectroscopic and chemical properties. *J. Chem. Phys.* **154**, 184703 (2021).

164. Luo, Y. *et al.* Addressing electronic effects in the semi-hydrogenation of ethyne by InPd2 and intermetallic Ga–Pd compounds. *J. Catal.* **338**, 265–272 (2016).

165. Davis, S. E., Ide, M. S. & Davis, R. J. Selective oxidation of alcohols and aldehydes over supported metal nanoparticles. *Green Chem* **15**, 17–45 (2013).

166. Sreekanth, P. M. & Smirniotis, P. G. Selective Reduction of NO with CO Over Titania Supported Transition Metal Oxide Catalysts. *Catal. Lett.* **122**, 37–42 (2008).

167. Zhang, L., Zhou, M., Wang, A. & Zhang, T. Selective Hydrogenation over Supported Metal Catalysts: From Nanoparticles to Single Atoms. *Chem. Rev.* **120**, 683–733 (2020).

168. An, K. & Somorjai, G. A. Size and Shape Control of Metal Nanoparticles for Reaction Selectivity in Catalysis. *ChemCatChem* **4**, 1512–1524 (2012).

169. Wang, J. X. *et al.* Oxygen Reduction on Well-Defined Core−Shell Nanocatalysts: Particle Size, Facet, and Pt Shell Thickness Effects. *J. Am. Chem. Soc.* **131**, 17298–17302 (2009).

170. Besenbacher, F. *et al.* Design of a Surface Alloy Catalyst for Steam Reforming. *Science* **279**, 1913–1915 (1998).

171. Ferrando, R., Jellinek, J. & Johnston, R. L. Nanoalloys: From Theory to Applications of Alloy Clusters and Nanoparticles. *Chem. Rev.* **108**, 845–910 (2008).

172. Hutchings, G. J. & Kiely, C. J. Strategies for the Synthesis of Supported Gold Palladium Nanoparticles with Controlled Morphology and Composition. *Acc. Chem. Res.* **46**, 1759–1772 (2013).

173. Lee, D. W. *et al.* Tailoring of Pt Island RuO_2/C Catalysts by Galvanic Replacement to Achieve Superior Hydrogen Oxidation Reaction and CO Poisoning Resistance. *ACS Appl. Energy Mater.* **4**, 8098–8107 (2021).

174. Wu, C. *et al.* Nanosized, Hollow, and Mn-Doped CeO_2/SiO_2 Catalysts via Galvanic Replacement: Preparation, Characterization, and Application as Highly Active Catalysts. *ACS Appl. Nano Mater.* **1**, 1438–1443 (2018).

175. Papaderakis, A. *et al.* Hydrogen evolution at Ir-Ni bimetallic deposits prepared by galvanic replacement. *J. Electroanal. Chem.* **808**, 21–27 (2018).

176. Su, Y., Liu, J., Mo, S. & Wang, F. Atomic-Scale Interface Engineering: Boosting Oxygen Electroreduction over Supported Ternary Alloys Fabricated by Carbon-Assisted Galvanic Replacement. *Adv. Mater. Interfaces* **7**, 2001267 (2020).

177. Silva, A. G. M. da, S. Rodrigues, T., J. Haigh, S. & C. Camargo, P. H. Galvanic replacement reaction: recent developments for engineering metal nanostructures towards catalytic applications. *Chem. Commun.* **53**, 7135–7148 (2017).

178. Wang, D.-Y. *et al.* Simple Replacement Reaction for the Preparation of Ternary $Fe_{1-x}PtRu_x$ Nanocrystals with Superior Catalytic Activity in Methanol Oxidation Reaction. *J. Am. Chem. Soc.* **134**, 10011–10020 (2012).

179. Wang, D.-Y. *et al.* Chemical Transformation from FePt to $Fe_{1-x}PtM_x$ (M = Ru, Ni, Sn) Nanocrystals by a Cation Redox Reaction: X-ray Absorption Spectroscopic Studies. *J. Am. Chem. Soc.* **129**, 1538–1540 (2007).

180. Wang, D. *et al.* Spontaneous incorporation of gold in palladium-based ternary nanoparticles makes durable electrocatalysts for oxygen reduction reaction. *Nat. Commun.* **7**, 11941 (2016).

181. Wang, W. *et al.* Reverse water gas shift over In_2O_3–CeO_2 catalysts. *Catal. Today* **259**, 402–408 (2016).

182. Frei, M. S. *et al.* Mechanism and microkinetics of methanol synthesis via CO_2 hydrogenation on indium oxide. *J. Catal.* **361**, 313–321 (2018).

183. Hengne, A. M. *et al.* Ni–Sn-Supported ZrO_2 Catalysts Modified by Indium for Selective CO_2 Hydrogenation to Methanol. *ACS Omega* **3**, 3688–3701 (2018).

184. Frei, M. S. *et al.* Nanostructure of nickel-promoted indium oxide catalysts drives selectivity in CO_2 hydrogenation. *Nat. Commun.* **12**, 1960 (2021).

185. Bavykina, A. *et al.* Turning a Methanation Co Catalyst into an In–Co Methanol Producer. *ACS Catal.* **9**, 6910–6918 (2019).

186. Shan, J. *et al.* PdCu Single Atom Alloys for the Selective Oxidation of Methanol to Methyl Formate at Low Temperatures. *Top. Catal.* **63**, 618–627 (2020).

187. Shi, Z. *et al.* CO_2 hydrogenation to methanol over Cu-In intermetallic catalysts: Effect of reduction temperature. *J. Catal.* **379**, 78–89 (2019).

188. Sitthisa, S. *et al.* Conversion of furfural and 2-methylpentanal on Pd/SiO_2 and $Pd–Cu/SiO_2$ catalysts. *J. Catal.* **280**, 17–27 (2011).

189. Mhadmhan, S., Franco, A., Pineda, A., Reubroycharoen, P. & Luque, R. Continuous Flow Selective Hydrogenation of 5-Hydroxymethylfurfural to 2,5-Dimethylfuran Using Highly Active and Stable Cu–Pd/Reduced Graphene Oxide. *ACS Sustain. Chem. Eng.* **7**, 14210–14216 (2019).

190. Meshesha, B. T. *et al.* PdCu alloy nanoparticles on alumina as selective catalysts for trichloroethylene hydrodechlorination to ethylene. *Appl. Catal. Gen.* **453**, 130–141 (2013).

191. Batista, J., Pintar, A., Mandrino, D., Jenko, M. & Martin, V. XPS and TPR examinations of γ-alumina-supported Pd-Cu catalysts. *Appl. Catal. Gen.* **206**, 113–124 (2001).

192. Cui, M., Qian, Q., Zhang, J., Chen, C. & Han, B. Efficient synthesis of acetic acid via Rh catalyzed methanol hydrocarboxylation with CO_2 and H_2 under milder conditions. *Green Chem.* **19**, 3558–3565 (2017).

193. Alcantara, M. L., Pacheco, K. A., Bresciani, A. E. & Alves, R. M. B. Thermodynamic Analysis of Carbon Dioxide Conversion Reactions. Case Studies: Formic Acid and Acetic Acid Synthesis. *Ind. Eng. Chem. Res.* (2021).